INFORMATION TO USERS

This manuscript has been reproduced from the microfilm master. UMI films the text directly from the original or copy submitted. Thus, some thesis and dissertation copies are in typewriter face, while others may be from any type of computer printer.

The quality of this reproduction is dependent upon the quality of the copy submitted. Broken or indistinct print, colored or poor quality illustrations and photographs, print bleedthrough, substandard margins, and improper alignment can adversely affect reproduction.

In the unlikely event that the author did not send UMI a complete manuscript and there are missing pages, these will be noted. Also, if unauthorized copyright material had to be removed, a note will indicate the deletion.

Oversize materials (e.g., maps, drawings, charts) are reproduced by sectioning the original, beginning at the upper left-hand corner and continuing from left to right in equal sections with small overlaps.

Photographs included in the original manuscript have been reproduced xerographically in this copy. Higher quality 6" x 9" black and white photographic prints are available for any photographs or illustrations appearing in this copy for an additional charge. Contact UMI directly to order.

ProQuest Information and Learning
300 North Zeeb Road, Ann Arbor, MI 48106-1346 USA
800-521-0600

UMI®

AN INTEGRATED GEOLOGICAL MODELING OF THE ARAB-D RESERVOIR, UTHMANIYAH AREA, GHAWAR FIELD

BY

SAMI OSMAN IBRAHIM

A Thesis Presented to the
DEANSHIP OF GRADUATE STUDIES
KING FAHD UNIVERSITY OF PETROLEUM & MINERALS
DHAHRAN, SAUDI ARABIA

In Partial Fulfillment of the
Requirements for the Degree of

MASTER OF SCIENCE
In

GEOLOGY
April 2002

ProQuest Information and Learning Company
300 North Zeeb Road
P.O. Box 1346
Ann Arbor, MI 48106-1346

KING FAHD UNIVERSITY OF PETROLEUM AND MINERALS
DHAHRAN 31261, SAUDI ARABIA

DEANSHIP OF GRADUATE STUDIES

This Thesis, is written by

Sami Osman Ibrahim

Under the direction of his thesis advisor, and approved by his thesis committee, has been presented to and accepted by the Dean of Graduate studies, in partial fulfillment of the requirements for the degree of MASTER OF SCIENCE IN GEOLOGY.

Thesis Committee

Dr. Ali Al-Ghamdi
(Thesis Advisor)

Dr. Mohamed Makkawi
(Thesis Advisor)

Dr. Khattab Al-Hinai
(Member)

Dr. Saleem Ghori
(Member)

Dr. Abullatif Al-Shuhail
(Member)

Dr. Mustafa M. Hariri
Department Chairman

Prof. Osama A. Jannadi
Dean of Graduate Studies

4/8/2002
Date

ACKNOLLEDGEMENT

Acknowledgement is due to King Fahd University of Petroleum and Minerals for support of this research.

I wish to express my appreciation to Professor Ali Al-Ghamdi who served as my thesis advisor. I also wish to thank the other members of my thesis committee Dr. Mohamed Makkawi, Dr. Khattab Al-Hinai, Dr. Saleem Ghori and Dr. Abdullatif Al-Shuhail.

Thanks are also due to Saudi Aramco for providing the basic data used in this research. Special thanks are due to the petroleum geology and geophysics section of the research institute for providing the necessary research facilities. I would like to thank Mr. Saeed Al-Zahrani, Mr. Ahmed Al-Musa, Mr. Mustafa Al-Ali and Mr. Maher Al-Marhoon from Saudi Aramco for their discussion. Sincere thanks are also due to Mr. Reda Meftahi from Paradigm Geophysical for his genuine support and valuable suggestions. A word of thanks is due to Prof. Salah Sultan for his continuous encouragement.

I would also like to express my sincere gratitude to the faculty members of the Department of Earth Sciences for their teaching, support and guidance. I'm deeply indebted to Dr. Mustafa Hariri for his continuous support and able guidance.

Of these, the name of my friend Fadhel Al-Khalifah has to be mentioned for his genuine assistance. Acknowledgements are extended to my Sudanese friends at King Fahd University of Petroleum and Minerals. Special thanks are also due to my friends Mohamed and Abdul-Malik Al-Amin and Osman El-Hussein for their valuable help.

Finally, a word of appreciation is due to my family for their great moral support.

Table of Contents

List of Figures

DISSERTATION ABSTRACT

NAME: Sami Osman Ibrahim

THESIS TITLE: An Integrated Geological Modeling of the Arab-D Reservoir, Uthmaniyah Area, Ghawar Field

MAJOR FIELD: Geology

DATE: April 2002

The Arab-D carbonates represent the most prolific oil-producing interval in the world. Yet the reservoir architecture remains problematic and with the exception of rare horizontal borehole or high-resolution 3-D seismic data, information is largely missing about lateral stratigraphic relationships. Spatial distribution of porosity and permeability and more specifically their extreme values are critical factors in the performance of the reservoir. Therefore, the main objective of this study is to develop a comprehensive 3-D quantitative geologic model of this reservoir.

The study extensively investigated the spatial distribution of lithology, porosity, and permeability of the reservoir in the study area by integrating wireline log data and 3D seismic data. The study provided detailed analyses of the physical interaction among facies distribution, stratigraphy, porosity and resultant permeability. A multidisciplinary approach was adopted by this study through the integration of various techniques. Seismic inversion, Seismic facies modeling, geostatistics and multiattribute transforms and neural network techniques were utilized in order to achieve better accuracy.

Master of Science Degree
King Fahd University of Petroleum and Minerals
Dhahran, Saudi Arabia
April 2002

ملخص الرسالة

الاسم: سامى عثمان ابراهيم
عنوان الرسالة: نمذجة جيولوجية متكامله لمكمن العرب-د البترولي، منطقة العثمانية، حقل الغوار
التخصص: جيولوجيا
تاريخ التخرج: ابريل 2002 م

تمثل رسوبيات العرب-د الجيرية اكبر طبقة منتجة للبترول فى العالم الا ان معرفة بنيتها الداخلية لا تزال امراً قابلاً للجدل وباستثناء بعض معلومات الابار الافقية القليلة والبيانات السيزمية ثلاثية الابعاد عالية الوضوح، تظل المعلومات الوافيه حول العلاقات التطبقية للمكمن و تغيره الجانبى مفقوده. التوزيع الحيزى للمسامية والنفاذية وبخاصة قيمها العاليه تعتبر عوامل حاسمه فى كفاءة اداء المكمن البترولى وانتاجيته. لذا تهدف هذه الدراسة بشكل رئيسى الى بناء نموذج جيولوجى شامل لهذا المكمن.

تتقصى الدراسة بشكل دقيق التوزيع الحيزى للسحنات الصخرية والمسامية والنفاذية للمكمن بمنطقة الدراسة وذلك بدمج البيانات السيزمية ثلاثية الابعاد و معلومات مجسات الابار. كما تقدم الدراسة تحليلاً دقيقاً للتفاعل الفيزيائى البينى لتوزع السحنات الصخرية، الطباقية الصخرية، المسامية والنفاذية الناتجة. تبنت الدراسة النهج متعدد الطرائق بتكامل عدة تقنيات للنمذجة. لقد تم استخدام تقنيات العكس السيزمي، نمذجة السحنات السيزمية، الاحصاء الجيولوجى و تحويل الخواص السيزمية الى معلومات الابار بواسطة شبكات الذكاء الاصطناعى بحثاً عن اقصى دقة ممكنة.

درجة الماجستير فى العلوم
جامعة الملك فهد للبترول والمعادن
الظهران، المملكة العربية السعودية
ابريل 2002 م

CHAPTER ONE

INTRODUCTION

Reservoir studies indicate that the challenge is in maximizing profit by drilling fewer wells. This target could be successfully achieved by effectively characterizing the petrophysical properties in relation to lithological and stratigraphical characteristics of the reservoir. This consequently helps in delineating precisely the reservoir fluid-flow units. The problem of uneven water flooding due to high permeability in some areas in the reservoir is making the issue of high permeability a significant research target. Therefore, special emphasis on petrophysical parameters, namely porosity and permeability, is very useful to display the spatial distribution of such features within the study interval. Further, an appreciation of the facies distribution and facies stratigraphy is fundamental in understanding the variation in reservoir petrophysical properties.

Lithological distribution, permeability and porosity studies were performed using a multidisciplinary approach to integrate geological, seismic and well data for better understanding of the reservoir flow patterns. Density, elevation, and geological nature of the flow systems are significant strategic planning issues for oil recovery in gravity drainage reservoirs.

1.1. LOCATION

The Ghawar structure is a giant north- south trending anticline covering an area of about 2530 sq kilometer located in Eastern Saudi Arabia. The Ghawar represents the most significant oil-producing field in Saudi Arabia and produces about 10% of the world oil. The largest oil accumulations within the field occur in the Arab-D reservoir, which lies at 6500 ft below the sea level and has a gross interval of approximately 300 feet thick.

Ghawar's main producing areas (from north to south) are: Fazran, Ain Dar, Shedgum, Uthmaniyah, Hawiyah, and Haradh. Uthmaniyah area lies almost in the central part of the Ghawar Field. The proposed models will be developed for the Arab-D reservoir in an area located on the southeastern portion of Uthmaniyah area (Figure 1).

1.2. PROBLEM STATEMENT

One of the major problems encountered in this reservoir has been the irregular advance of the water flood front from the injectors toward the producing wells, especially on the shallower-dipping eastern flank (Douglas, 1996). Some of the Ghawar producing Fields, including Uthmaniyah, are characterized by frequencent occurrences of high permeability, which have an enormous impact in terms of well performance, sweep efficiency, and oil recovery.

Spatial distribution of porosity and permeability and more specifically their extreme values are critical factors in the performance of a reservoir. Reservoir simulation and reservoir characterization studies have shown that a critical element in the construction of a reservoir model is capturing of high and low permeability distribution.

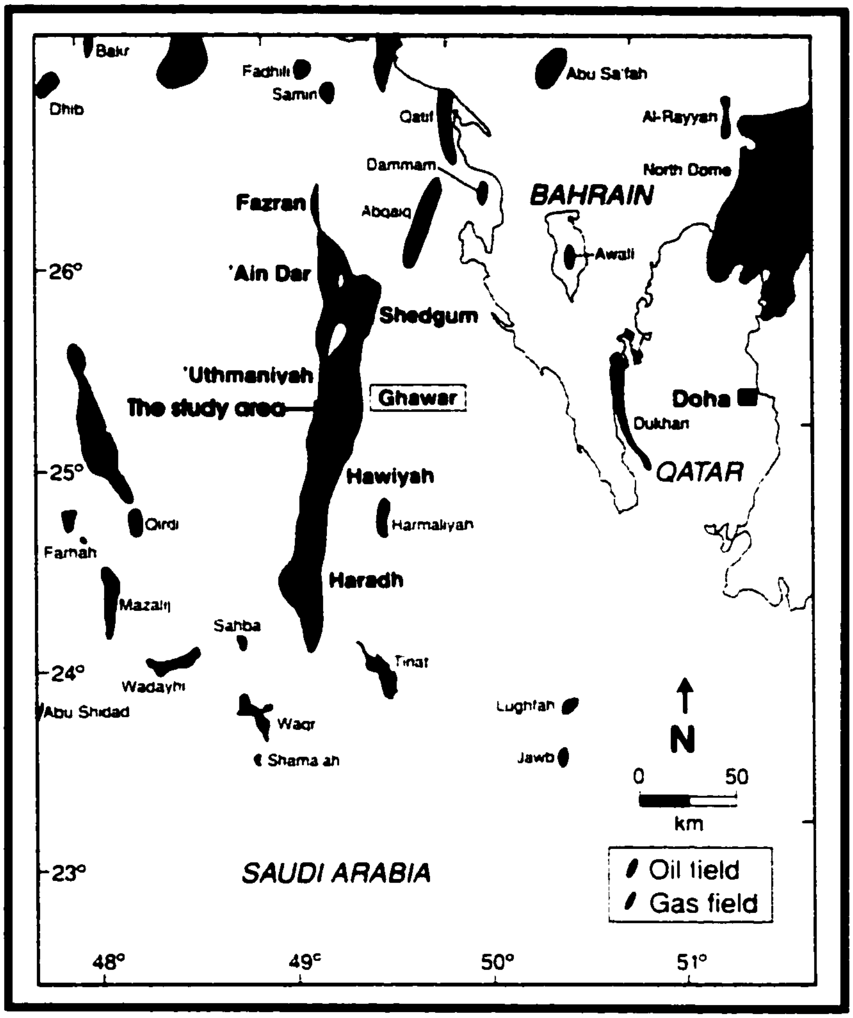

Figure 1: Base map showing the location of the study area (After Cantrell et al.,2001)

High permeability zones are responsible for early breakthrough of injected water resulting in the bypassing of significant volumes of oils, whereas low permeability strata represent flow-barriers and reduce gravity effect. Published permeability rock-fabric data from the Arab-D reservoir show that only a small percentage of reservoir rock is grainstone with more than 14% intergranular porosity and permeability greater than 1 Darcy. If this rock fabric is located in a bed with a few feet cycle, it may be averaged and missed; therefore it is important to describe and measure rock fabrics at a scale at which these extremely high permeable strata can be captured. Only then can these important high permeability rock-fabric flow units be mapped and properly incorporated in subsequent flow simulations.

Integration of stratigraphy, lithologic analyses, and petrophysical analyses into a quantitative 3-D model fills a gap in understanding the spatial distribution of these high permeability zones as well as other flow properties. For realistic interpretation of rock properties, petrophysical analyses must be integrated with stratigraphy and lithology. Distribution patterns of porosity and permeability in different zones of a reservoir change depending on lithology (Sahin and Ghori, 1997). Depositional facies distribution reflects basin paleogeography and the sedimentary processes associated with the geologic setting; these factors in turn, relate to reservoir heterogeneity; and that is why the distribution of depositional facies exerts the primary control on reservoir heterogeneity. Additionally, to fully understand the reservoir characteristics, influence of dolomitization on the development and distribution of porosity and permeability needs to be discussed. Relating dolomitization to petrophysical data is crucial to understanding reservoir quality in carbonate reservoir.

The Arab-D carbonates represent the most prolific oil-producing interval in the world. Yet the reservoir architecture remains problematic and with the exception of rare horizontal borehole or high-resolution 3-D seismic data, information is largely missing about lateral stratigraphic relationships (Meyer et al., 1996). A major concern in petroleum exploration and development is the detailed architecture (internal and external) of reservoirs in a field or basin-wide setting. This concern is due, in part, to the effects of architecture on fluid flow. Although such studies have been conducted, they may either have remained confidential or have partially analyzed separate reservoir parameters.

1.3. OBJECTIVE

1. The main objective of the study is to develop a 3-D quantitative geologic model of the reservoir.
2. The study will extensively investigate the spatial distribution of lithology, porosity, and permeability of the reservoir in the study area by integrating wireline log data, 3-D seismic data and core description.
3. Special attention will be given to the role of dolomitization in the interpretations.
4. The study will provide detailed analyses of the physical interaction among facies distribution, stratigraphy, porosity and resultant permeability.

1.4. LITERATURE REVIEW

Geostatistics provides a toolbox for geologists to analyze data and transfer such analysis and interpretation to the task of reservoir forecasting. The major contribution of geostatistics to reservoir modeling and characterization lies in data integration, providing a formalism to encode vital, possibly nonnumerical information; combine different data accounting for uncertainty; and transfer such uncertainty into the final model (Journel, 1994).

Geostatistical stochastic modeling has been widely used over the last few years to generate more accurate reservoir models that better honor heterogeneity, reservoir architecture, and complex information. Srivastava (1994) stated that even a single outcome from the several stochastic realizations is a better basis for performance prediction than a single outcome from traditional technique that does not honor reservoir heterogeneity. He listed two aspects of a stochastic model of a reservoir: a) the architecture of the flow units, and b) the spatial distribution of rock fluid properties within each flow unit. He pointed out that stochastic model may also be used to integrate seismic data with petrophysical data or to ensure that the model follows some basic geologic principles in terms of where certain facies can and can not appear; and thus it honors complex information. He also added that the reservoir architecture is commonly the first priority in a stochastic reservoir model and is usually described in terms of the different facies.

Weber (1986) found out that boundaries of permeable bodies within a reservoir usually coincide with changes in reservoir facies (i.e. with boundaries of genetic units). Within certain types of genetic units, characteristic patterns of porosity and permeability zonation is often found. Hearn et. al. (1986) confirmed these findings by recognizing that the distribution of flow units is related to the facies distribution. The results of many recent studies indicate that there is a close relationship between facies and reservoir quality.

Lamy et al. (1998) published a comprehensive study on seismic inversion for reservoir modeling. They used the technique to invert seismic traces within the model into acoustic impedances, which finally transformed into reservoir parameters such as porosity, through a statistical petrophysical relationship. Wang (1998) reported that the acoustic impedance decreases linearly with porosity, and should be used to estimate petrophysical properties from seismic data. Bashore et al. (1994) suggested that the incorporation of secondary data set such as seismic inversions can provide information on small-scale variations in interwell heterogeneity, which may have a profound effect on fluid flow estimates and estimate uncertainty.

Douglas (1996) constructed a Geostatistical model for the Arab-D reservoir in North 'Ain Dar Field. He improved the previous deterministic models covering the area. He suggested that the reservoir zonation provided by the sequence stratigraphic model is significant from a reservoir flow sense. His simulation model was successful in capturing the irregular patterns of water movement from the flank injectors toward the crest of the structure. Porosity and permeability models were constrained by the distribution of the reservoir rock types that are distinct from each other in terms of population of these properties. Data extremes for porosity and permeability were successfully captured in the model. He mentioned that his model should be applicable to other portions of the Ghawar reservoir. Cantrell and Hagerty (1999) found out that even microporosity in the reservoir has a noticeable affect on the fluid flow properties and ultimate recovery of hydrocarbons. Saner and Sahin (1999) grouped the carbonate rock types in the Arab-D reservoir into three lithofacies: granular, muddy-granular, and muddy. They recognized that porosity and permeability distribution patterns of the Arab-D zones are controlled by both type and the arrangement of different lithofacies. They integrated stratigraphic and petrographic analyses with basic core measurements based on core plugs from a well drilled in the Uthmaniyah Field.

A recent systematic petrographic analysis of the Arab-D in the Hawyiah area conducted by Meyer et. al. (2000) showed that high permeability intervals are attributed to the presence of oolitic, skeletal pelletoidal, foraminiferal, cladocoropsis lithofacies and even ordinary rock fabrics. Such intervals sandwiched between low-permeability strata characterize the sequential stratification of the stratiform of high permeability flow units in the reservoir. Post-depositional dolomitization from carbonate diagenesis distributed sporadically throughout the reservoir. Linear NE-oriented pattern of these dolomite occurrences suggest that some structural elements is responsible from controlling their orientation. It's interpreted that these linear patterns to have formed in response to a series of fracturing and faulting events that allowed dolomitizing fluids to invade the reservoir from below, and preferentially dolomitized there. These areas of high dolomite are important because they tend to be the areas where overall high flow occurs and where high permeabilities predominate (Cantrell, et. al., 2001).

1.5. GEOLOGIC SETTING

Geologically, the Arabian Peninsula can be divided into three distinctive tectonosedimentary provinces (Figure 2) as follows (Powers, et al., 1966):

1) The mobile belt: is located to the north and east of the Arabian Shelf. It's mainly composed of the Zagros Mountains and Oman Mountains, which represent small links in the much grater Alpine-Himalayan Orogenic System. It also comprises narrow foreland basins, which contain the major oil fields of parts of Oman and of southwestern Iran.

2) The Arabian Shelf: is located north, east, and northeast of the shield. It's composed of sedimentary rocks deposited during the Cambrian to Holocene period, in epicontinental transgressions that took place along the lower part of the Arabian Shield. These transgressions caused the shield to be gradually covered by a thick, nearly horizontal to gently dipping sequence of strata. These strata were subjected to slight deformation that produced an easterly to northeasterly dipping sedimentary succession with relatively undisturbed beds, which represent the geologic Arabian shelf. The sediments are of both shallow marine and continental origin. The Arabian Shield can be divided into three major distinctive geologic units: the interior homocline, the interior platform, and several intrashelf basins. Most of the known reservoirs of eastern Arabia were found in the rocks of the Arabian Shelf.

3) The Arabian Shield: The shield rocks occupy about one-third of the surface area of the Arabian Peninsula. On the west they form most of Najd and all of Al Hijaz and Asir; on the southwest they support the highlands of Yemen, and along the southern coast they occur in sporadic outcrops. The western Arabian Shield of Saudi Arabia is an extensive area of Precambrian rocks, mainly igneous and metamorphic, and largely overlain by younger volcanics in the west. Included within the basement complex are great belts of sedimentary rocks, now contorted, intruded and metamorphosed. Presumably, through the Precambrian time, the shield was subjected to several times to downwarping, sedimentation, orogeny, injection by plutonic rocks, and leveling before becoming immobile. During the Tertiary Period, substantial faulting and other disturbances occurred along the margin of the Red Sea depression.

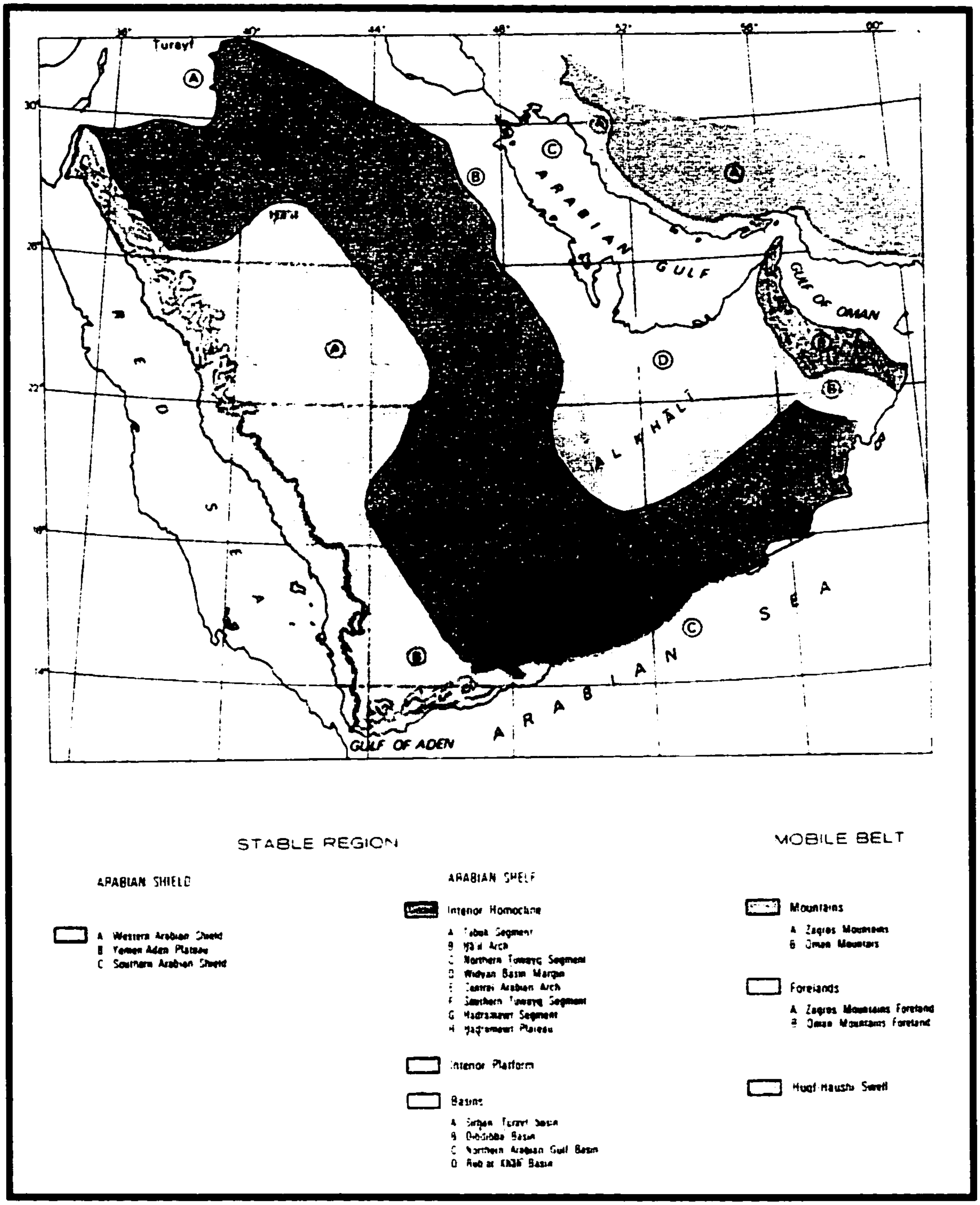

Figure 2: Tectono-sedimentary units of the Arabian peninsula (After Schlumberger, 1975)

1.5.1. JURASSIC SUCCESSION

Saudi Arabia has 26% of the world's total proved oil reserve. Approximately two-thirds of the Saudi proved oil reserve occurs in the Middle-Late Jurassic carbonate reservoirs. The Arab Formation consists of four members, commencing at the base with the Arab-D member, and followed by the Arab-C, Arab-B, and Arab-A members. Each member consists of a couplet (i.e. the Arab-D carbonate and the Arab-D anhydrite), which represents a cyclic transition upwards from shallow marine carbonates to marginal marine evaporites. The Arab Formation is overlain by the regional cap rocks, the Hith Anhydrite, which represents the uppermost formation in the Jurassic succession. The Hith Formation averages 500 ft in thickness and forms an extensive seal that has prevented further upward movement of oil (Huges, 1996). Beneath the Arab Formation, a descending sequence of Upper and Middle Jurassic limestone rock-units occurs, namely the Jubailah, Hanifa, Tuwaiq Mountain, and Dhruma Formations, followed downward by the shales and limestones of the Lower Jurassic Marrat Formation and sandstones with shales of the Lowermost Jurassic upper Minjur member.

The Jurassic succession is generally composed of marine carbonate and evaporite rocks. The Jurassic section has good exposures in central Saudi Arabia, except for the Arab Formation. The extensive dissolution of the anhydrite beds and the subsequent collapse of the overlaying carbonates in this formation have prevented working out a precise lithologic sequence. As a result, subsurface units at Dammam well number 7 in Eastern Province have been taken as the type and reference section (Powers, et al., 1966).

The thickness of the Jurassic succession reaches about 1200m at the outcrop section in central Saudi Arabia, and increases laterally eastward up to 3000m in eastern oil fields.

1.5.2. GEOLOGY OF UTHMANIYAH AREA

Ghawar structure is an elongate, asymmetric NNE-SSW striking, north plunging, complex anticline, which started forming in the Jurassic period and kept active during the Cretaceous and Tertiary periods. The anticline consists of a simple fold in the south and two crestal closures in the center, and splits into two in the north.

The Uthmaniyah area, which is located in the central portion of the Ghawar structure, is reflected at the surface by a dissected plateau of a resistant limestone layer. The plateau surface extends largely over the western flank of the Ghawar structure. The Uthmaniyah Field shows a low anticline having about 450 feet of relief along the eastern edge and a very low swell of less than 50 feet of relief along the western edge. Oil was first found in Uthmaniyah in 1951 in the main producing interval, the Arab-D member and the uppermost Jubailah Formation.

1.5.3. RESERVOIR GEOLOGY

The Arab-D reservoir includes the upper part of the carbonate mudstones of the Jubailah Formation and the overlying carbonates of the entire Arab-D of the Arab Formation (Powers, et al., 1966). The boundary between these two Formations is conformable and represents a transition from mudstones to clean packstones (Figure 3). The Arab-D reservoir is thick and massive carbonate sequences of Upper Jurassic age, comprising various carbonate rock types of an approximately 300 ft thickness. These rocks form overall a cleaning-up and shallowing-up succession. The reservoir exhibits an overall downward decrease in porosity and increase in dolomite content. Grainstones dominate the upper interval, whereas wackestones and fine-crystalline dolomitic rocks dominate the lower portion. It generally exhibits a complex lithology and a large variety of heterogeneities, which remarkably challenge reservoir evaluation and field development. High permeability occurrences are abundant throughout the reservoir, and have enormous impact in terms of well performance, sweep efficiency, and oil recovery.

The reservoir displays good porosity and permeability with local high permeability areas characterizing the upper portion of the reservoir (Saner and Sahin, 1999). Interparticle porosity, in grainstones and dolomitic grainstones, predominates in the reservoir. However, other porosity types such as the intercrysalline porosity in dolomitized rocks are locally important (Douglas, 1996). Detailed studies show that average permeabilities are about 100 md. High permeability is observed in stromatoporoid, cladocoropsis, and grain-dominated carbonate facies. Cladocoropsis appeared to be especially important for super-k flow in the Uthmaniyah area.

A comprehensive stratigraphic study on the Late Jurassic depositional sequences in the Arabian Gulf, conducted by Al-Sharhan and Whittle (1995) showed that the Arab-D reservoir is characterized by mudstones and wakestones in the basal part of the section that grade upward into bioclastic dolomitic packstone/grainstone, which show the highest porosity in the study area. Huges (1996) concluded that these carbonates are composed of a series of high frequency palaeobathymetric changes, which superimposed upon an extensive carbonate-platform. Gradual shallowing of the platform resulted possibly from a reduction in subsidence rate, a fall in the sea level, rise in carbonate productivity rate or a

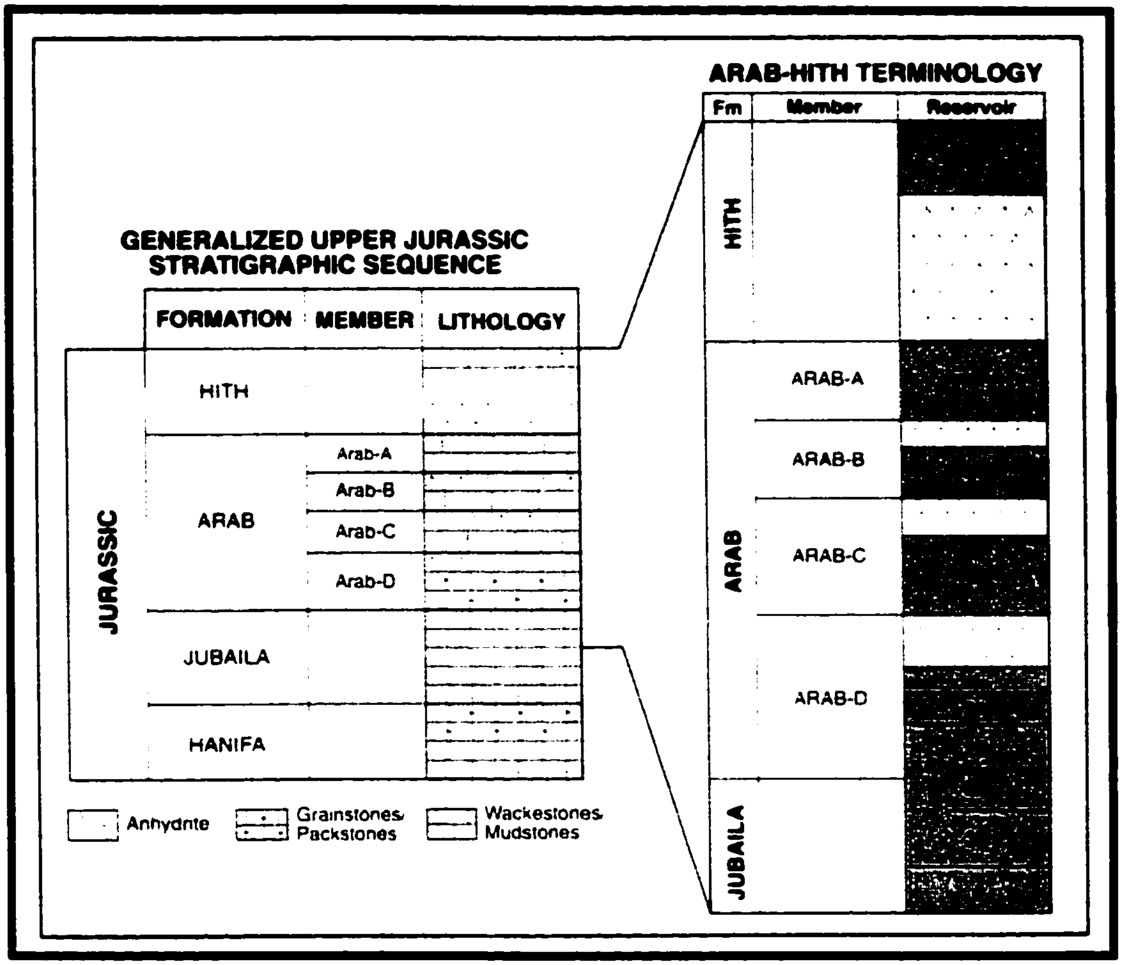

Figure 3: Geology and Stratigraphy of the Arab-D reservoir (After Cantrell et al.,2001)

combination of these. The latest episode of very shallow marine carbonate sedimentation terminated with the deposition of the Arab-D evaporites. Initially, the Arab-D reservoir in Ghawar was divided into zone 1, 2, 3, and 4. These zones were further subdivided to form zones 1, 2A, 2B, 3A, 3B and 4 (Daetwyler, 1987).

1.6. FACILITIES

Petrosystems' Unix window based Stratimagic package (version 1.8.0 – 2001) and NexModel software were used for seismic facies and petrophysical analyses. The seismic inversion model was constructed using the Hampson-Russell Unix window based STRATA software (Version 4.0-2000). The unix window based Emerge software of Hampson-Ruessell (Version 4.0) was used to genrate petrophysical models using multiattribute regression supported by Neural Network technology. Geostatistical analyses were performed utlizing Geostat software (Version 4.0) of Hampson-Russell. These packages were accessed through a Sun workstation at the Petroleum Geology and Geophysics Laboratory of the Research Institute, King Fahd University of Petroleum and Minerals.

CHAPTER TWO

PROCEDURE AND DATA HANDLING

2.1. INTRODUCTION

Reservoir simulations, used to predict the production behavior of hydrocarbon reservoirs, have three ingredients: fluid flow equations, fluid properties, and rock properties. Fluid flow equations are universal, fluid properties may show limited variation with depth as a function of pressure; laterally these properties show limited variation. However, rock properties can vary abruptly in space and can therefore often be the main cause of uncertainty in reservoir simulation studies. Therefore, great care should be devoted to description of rock properties.

To describe the reservoir architecture and properties, seismic data, wire line log data and core data are commonly used. Seismic data gives 3-D information on the interwell area. However, this technique seldom yields information detailed enough to be used in a reliable description for the reservoir architecture and properties. Well logs and core give detailed information on the rock properties, but this data is only valid in the near surroundings of the well and can't usually be easily interpolated into the interwell area. Hence, reservoir-modeling techniques, that incorporate different types of reservoir data with geological knowledge, have to be used. In general terms, three groups of modeling techniques can be differentiated: geological modeling, deterministic interpolation and geostatistical techniques. All these types have been utilized in this study and supplemented by the new Neural Network technique to optimize precision and to achieve a meaningful interpretation.

2.2. PROCEDURE

The study involved geological and petrophysical evaluation based on data obtained from well log motifs for eleven wells in the study area, and a 3-D seismic survey covering the reservoir being proposed for this study. The study has utilized and integrated the following methods (Figure 4):

1. A stratigraphic framework was developed for the model area by using information obtained from well log correlation and 3-D seismic data. Stratal surfaces that define the reservoir intervals were picked and used as a basis for the subsequent lithological and petrophysical modeling of the reservoir intervals.
2. Seismic data together with well log data were analyzed to determine spatial distribution of lithofacies and their physical interaction with porosity and permeability distributions and other petrophysical properties. Facies maps were generated directly from seismic data using the Neural Network technique for the computation of each trace assigned in the correlation procedure.
3. Stratal surfaces, required in most of the subsequent analyses, were mapped. This substantially contributed to the prediction of the distribution and continuity of flow intervals. Facies and layering data could largely support the petrophysical analyses.

4. Three-dimensional impedance model for the entire reservoir interval was constructed by a constrained model-based inversion technique. The technique allows for the production of an inverted 3-D seismic section, which displays velocity or impedance versus depth or time from input consisting of stacked seismic data constrained by well logs.
5. Petrophysical modeling using the geostatistical kriging and stochastic methods for porosity and permeability were carried out by integrating porosity logs and seismic data. Porosity models were constrained by the lithological or impedance models generated in the previous step.
6. To achieve the previous step, various geostatistical techniques were used for more reliable reservoir models with some emphasis on stochastic modeling to better display the variability of these properties.
7. Geostatistical porosity models were calibrated with porosity models generated by the new method of the multi-attribute transforms using Neural Network technology to reach higher confidence.

Extensive and detailed interpretation of the produced models is an essential goal.

2.3. DATA HANDLING

2.3.1. WELL INFORMATION

Different types of logs, markers and some check-shot surveys for eleven wells, with an average spacing of 1.5 km, were originally prepared as soft data. The well data set contains sonic, density, core effective porosity and core absolute permeability logs, for each well, measured at a constant depth interval of 0.5 ft.

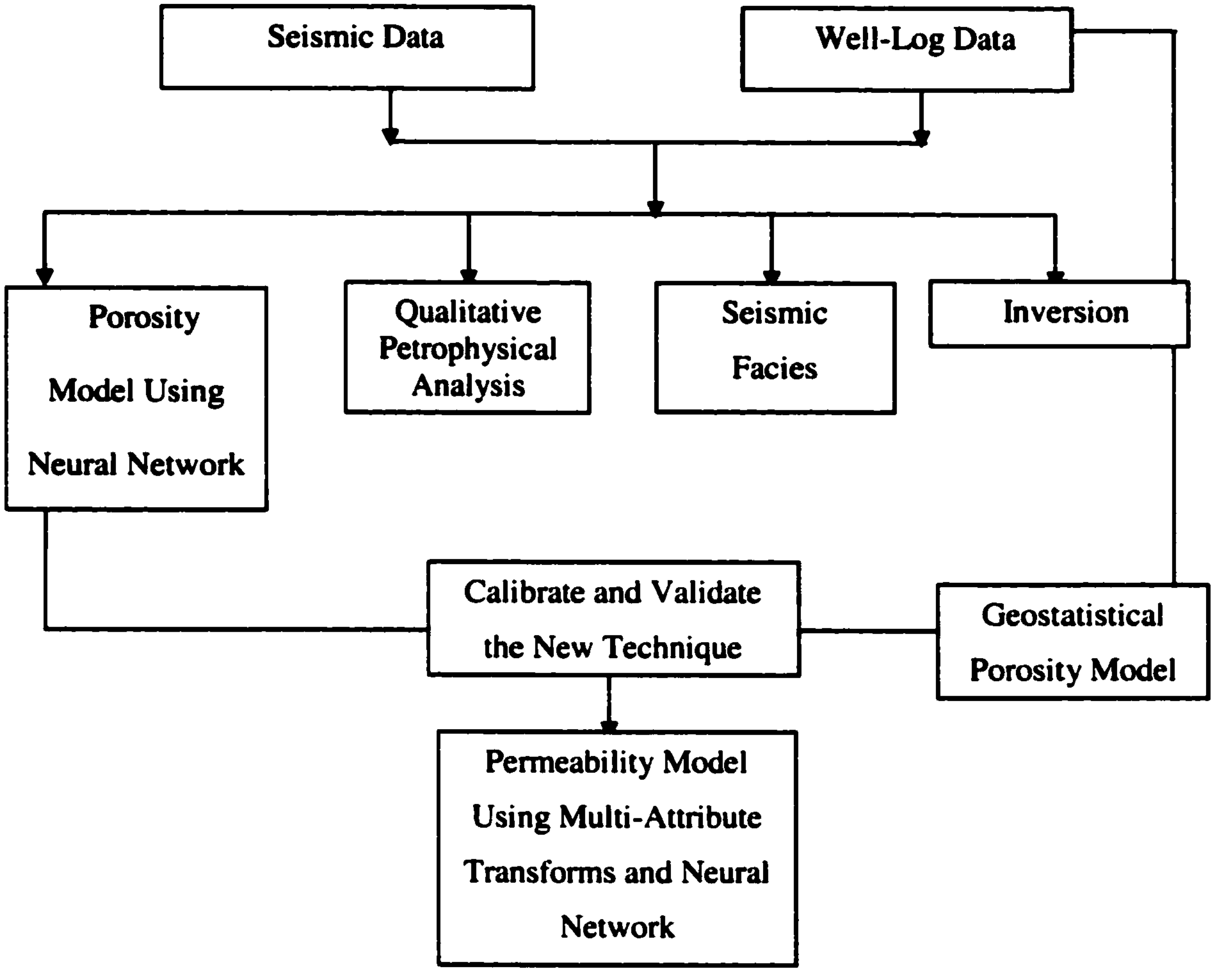

Figure 4: Flow chart showing the procedure

The four log types for eleven wells were imported into lithofacies modeling software. Every log in these wells has a large depth coverage extending from few hundreds feet below the surface all the way downward to the bottom of the Arab-D reservoir. Markers for every well, defining tops of main lithological units were imported to guide picking major horizons and correlating events to be studied throughout the analysis. Check-shot data for four wells were also loaded and formed the basis for the generation of synthetic traces needed to test quality of trace shape classification, which represents the intimate element to the lithological modeling.

All available types of logs and markers for eleven wells were imported and saved as a database for the subsequent geostatistical and neural network applications. The depth coverage in four wells is only limited to the Arab-D zone, where it extends from near surface downward to the bottom of the Arab-D reservoir. No check-shot data were needed since check-shot corrections were interactively preformed through inversion process.

2.3.2. SEISMIC DATA

3-D good quality stacked and migrated seismic reflection data, for the study area, were imported. The given seismic data for the study area cover an area of 651.37 square kilometer. The seismic coverage comprises 1005 E-W trending inlines and 1037 N-S trending crosslines with inline spacing and CDP spacing of 25 meters. The number of live traces loaded is 1041148 with time sampling interval of 4 milliseconds and 650 samples per each trace. Time domain of the seismic section starts from -100 milliseconds and ends with 2000 milliseconds.

Seismic data were then subjected to a careful refining in order to reach a higher level of accuracy and hence optimizing reliability of the final model. As a result, the size of the seismic block was objectively reduced and data at the edges were excluded to avoid noisy data inherited from acquisition and processing. A new block comprising the central part of the survey was created (Figure 5). The final block comprises a mesh of a thousand lines, covering an area of 149.375 square kilometer with 600 inlines and 400 crosslines. The data were eventually resampled and confined to a targeted time window of 500 milliseconds between 900 and 1400 milliseconds where the time interval of interest resides.

At least, one horizon is needed to subsequently guide interpolation during execution of inversion and lithological models. Both given and interpolated check-shot data and markers were initially utilized in performing the seismic-well tie and picking the top of the Arab-D reservoir at well locations. These picks were later used as seed points and a complete picking was precisely carried out on line-by-line basis. More accurate interpolation and editing were achieved after completion of inversion. The horizon was finally exported to other computer applications where it represents a major prerequisite to modeling processes.

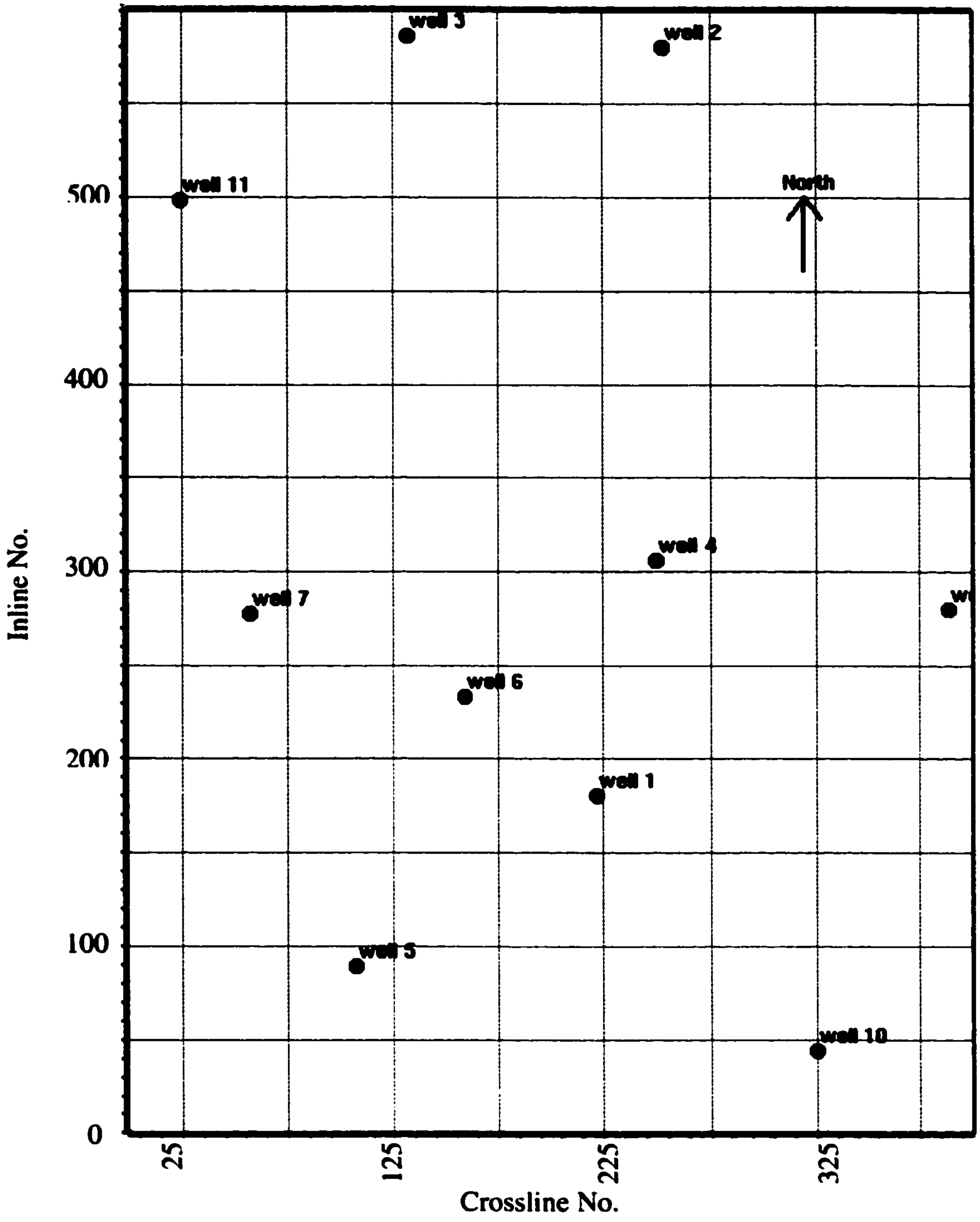

Figure 5: Base map of the area showing well distribution and seismic coverage

CHAPTER THREE

SIESMIC INVERSION AND LITHOFACIES ANALYSIS

3.1. SEISMIC INVERSION

To optimize the understanding of reservoir, it is necessary to combine geophysical, geological and petrophysical measurement and knowledge. However, the integration of information from different disciplines is in practice not easy to achieve. Inversion of seismic data to acoustic impedance has proven to be an excellent tool for integrated studies. The ultimate aim of the inversion process is to reconstruct the acoustic impedance profile of the subsurface. This can not be achieved to perfection since these profiles contain detail, which is far beyond the seismic resolution. To obtain the best result, all available data (i.e., seismic and well data) and prior information (e.g., of the wavelet and stratigraphy) have to be used.

3.1.1. HISTORICAL BACKGROUND

From geophysical prospective, reservoir characterization has traditionally used seismic amplitude data. This dates back to when seismic amplitudes were used for bright spot detection. Shortly afterward, the first attempts were made to invert amplitude data to directly recover rock property parameters, primarily acoustic impedance. Seismic amplitudes and amplitude attributes characterize the reflection properties of an interface and only indirectly the surrounding rocks. In contrast, rock property parameters derived from seismic directly characterize the rocks, meaning they can be directly and quantitatively related to other key reservoir parameters. A second advantage is that rock property data derived from seismic is equally valid over the whole section, not just focused on areas with high amplitudes. Third, it enables reservoir geologists and engineers to not only think in terms of reflectors but in terms of layers and layer properties. Therefore, seismic inversion has increasingly become more important tool in oil exploration.

The first generation of inversion methods met with mixed success, mainly due the problems with data quality and lack of phase control. However, improved data quality and the availability of computation power in the late 1990s brought about a second generation of much more powerful and robust impedance inversion algorithms. The basis for successful modern inversion algorithms is their ability to integrate additional information into the process. The low-frequency component can be recovered by using choice of geologic modeling methods, preferably based on interpretation of the stratigraphic framework. Robust wavelet estimation algorithms became available, and the wavelet could be fully incorporated into the inversion algorithm to back out seismic phase and spectral coloring.

3.1.2. PRACTICAL ADVANTAGES OF SEISMIC INVERSION

Because of quality and productivity benefits, impedance is replacing seismic reflection amplitude data as the primary basis for reservoir interpretation and characterization. Impedance-based seismic reservoir characterization is now standard procedure in most large oil companies and many independents for high–cost projects (Riel, 2000). The ability of modern inversion approaches to integrate large amounts of different data is what improves accuracy, reliability, and resolution of reservoir models relative to models based on the interpretation of seismic and the use of seismic amplitudes and amplitude attributes. It is expected that the next few years will bring practical inversion algorithms that use more and more information to dramatically enhance reservoir characterization resolution, accuracy and reliability (Riel, 2000). Because impedance is a rock property it can be directly linked to other reservoir properties available at well control points such as porosity, fluid content and permeability. Furthermore, being a layer property, impedance is an ideal basis for the application of modern volume interpretation methods. Also because it is a layer property, geophysicists, geologists and petroleum engineers understand impedance. As such, it is proving an ideal common currency for communication by asset teams.

In addition, employing impedance results in increased resolution through the increased bandwidth and reduced tuning through the removal of the wavelet and the integration of low frequency model. A major contribution to the success of impedance model is the presence of information down to zero Hz. This requires information from beyond the seismic bandwidth and therefore necessitates the integration of seismic data with data containing low frequency information, which is often generated from well log data (Marzuki et. al., 2001). Field experience shows that the detailed models resulting from this approach have resulted in the identification of new hydrocarbon pools in and close to existing fields, improved reserve calculations and improved well planning for secondary recovery. Some of the cost benefits experienced by oil companies adopting this new approach have been improved water flood design, identification of attic and downdip hydrocarbon pools, improved hydrocarbon in place and recoverable reserve calculations with associated uncertainty and risk analysis (Atkins et. al., 2001).

3.1.3. THEORETICAL BACKGROUND

Simply, inversion or inverse modeling can be defined as the calculation of an impedance function, which could have generated a given seismic trace. This indicates the non-unique nature of the solution generated by most inversion techniques. Most inversion techniques assume that the seismic trace is the convolution of a wavelet (of given bandwidth and phase) with the reflectivity series underlying the ground location of the seismic trace. Thus, the seismic trace is assumed to be free-noise, multiple free, and zero offset. The amplitudes of the seismic trace are taken as proportional to the reflection coefficients of the subsurface neglecting the effect of improper scaling of the data, amplitude changes due to tuning, and residual phase either left in the data after processing or introduced by processing.

The well logs in the area provide the critical calibration of impedance to lithology since there is no worldwide relationship linking the two. This calibration is achieved by properly establishing well-seismic tie after performing an accurate correlation process. Many inversion approaches use the sonic log in a well on or near the line to start or guide the inversion. The reflectivity function from the sonic log can be used to determine the effective wavelet present in the seismic field data. This wavelet can then be used as to estimate the reflectivity function of each trace, and from the later the values of the acoustic impedance function are estimated. Neither velocity nor acoustic impedance uniquely correlates with a given lithology, unless local geologic input and well data constrain the relationships. In the presence of noise, some inversion techniques are unstable and all are inaccurate. The amount of user intervention required depends upon the algorithm and the approach used (Dobrin and Savit, 1988).

Mathematically, post-stack seismic inversion is the process, which analyzes stacked seismic traces and attempts to reconstruct the velocity or impedance structure of the earth. The fundamental model on which inversion is based is the 1-D convolutional model:

$$T(i) = \sum_j r(j) W(i - j + 1) + n(i) \tag{3-1}$$

Where: $T(i)$ = the seismic trace

r (j) = the zero-offset reflectivity of the earth expressed as a time series

W (i) = the seismic wavelet, assumed to be constant

n (i) = additive random noise

Multiples in this model are assumed to be negligible.

Inversion can be thought of as the process of determining the reflectivity, r(j), given a seismic trace, T(i). Since the reflectivity is related to the impedance of a series of layers in the earth by:

$$r(j) = \frac{I(j) - I(j-1)}{I(j) + I(j-1)} \tag{3-2}$$

Where I(j) = impedance = ρ(j) v(j) = density $_{(j)}$ × velocity $_{(j)}$

Inversion can be thought of equally as determining the underlying impedance. Many approaches are commonly used to inversion. They differ primarily in their treatment of the seismic wavelet, and their handling of the non-uniqueness problem associated with inversion.

3.1.4. MODEL BASED INVERSION

Model-based inversion is a generalized linear inversion algorithm. It is assumed that the wavelet in the seismic data is known and, in fact, is the wavelet extracted or the current wavelet. For each trace a synthetic seismogram is calculated using the initial guess impedance from well logs and the known wavelet. That impedance is then modified gradually, until the resulting synthetic trace matches the real seismic trace within some tolerance level. How far the algorithm may move from the initial guess can be manually controlled in order to match the real data.

The general workflow of the methodology can be briefly summarized as follows:

1) Build an initial stratigraphic model comprising a few readily identifiable and correlatable stratal surfaces using the seismic data and best quality log data.
2) Synthesize sonic and density logs required for placing the well data in the time domain using multi-well multi-level approach where levels are defined by the stratigraphic framework.
3) Interpolate and extrapolate the good quality log data along the stratigraphic layers to form a low frequency model.
4) Extract a wavelet from the seismic data using the good quality log data.
5) Invert the seismic data to produce an initial impedance model.
6) Update the model iteratively by refining and adding more detail to the stratigraphic model, adjusting low frequency model accordingly, improving the wavelet and re-running the inversion

Mathematically, model-based inversion follows from the convolutional model:

seismic = (wavelet * reflectivity) + noise

where * indicates the convolution process

Assuming that the seismic trace is known, the wavelet is known, and the noise is uncorrelated and random, the reflectivity is that sequence, which fits the data best. That is, if one can find a reflectivity, which convolves with the wavelet to give a good approximation to the seismic trace, this reflectivity should be assumed as the right answer.

This algorithm was chosen to perform inversion in this study due to its numerous advantageous characteristics. Firstly, it attempts to achieve resolution beyond the seismic band by a stronger use of the a priori impedance logs and since high-resolution logs are input, high resolution in the inversion is possible. Secondly, simplicity is implemented by limiting the solution space to that spanned by well logs. Thirdly, it therefore produces the closest model to the initial or the geological model, which is also consistent with the seismic data. However, it has a potential problem, which is the sensitive dependence on the wavelet. Therefore, careful and proper extraction of the dominant seismic wavelet should be achieved.

The 3-D seismic block for the area was used as input data. Density and sonic logs and lithologic markers for eleven wells were used to generate the initial impedance model and to guide picking of horizons, log correlation, and interpolation. Log correlation used is a process of applying a manual correction to the depth-time curve to optimize the correlation between initial model and the seismic data. It changes the depth-time curve in exactly the same way as a check-shot correction. It consists of selecting events on the synthetic trace and the corresponding events on the real trace, and applying stretching and squeezing. Since the synthetic is used, the choice of wavelet may be more crucial.

Resulting correction was applied only to the time-depth curve and hence it did not change the velocities in the sonic log. This method has the effect of maintaining the original reflection coefficients for synthetic calculations. All wells gave correlation coefficients higher than 0.75. Wavelets dominant in seismic data in the vicinity of wells were extracted after correlation was established. Some of these wavelets were then averaged, compared to a statistically derived seismic wavelet for validation, and set as the current wavelet to be used in inversion. Wavelet extracted is a ricker zero-phase wavelet with phase rotation of 180° (Figure 6).

The initial guess model, which consists of an impedance log, was derived by multiplying real sonic logs by real density logs (Figure 7). The impedance log model must be measured in two-way travel time whereas original logs are measured in depth. Therefore, depth-time correction is deemed critical to the initial guess model. For integration to take place a velocity model needs to be defined that relates the time and depth domain. This velocity model needs to be accurate enough to place each layer in the well log alongside the equivalent event in the seismic data. A first pass low frequency model is usually generated from the interpolation and extrapolation of impedance logs from wells along the layers defined. The first impedance values at trace locations in this model are used for inversion. The wavelet extracted from wells and the low frequency model is used as the basis for a constrained model based inversion to give the initial impedance model. The impedance model and the stratigraphic model are modified and refined in an iterative way searching for the best tie between events picked on well logs and events interpreted on the impedance model, which is critical to placing the well data accurately in time and avoiding miss-correlation (Figure 8). The wavelet is updated as

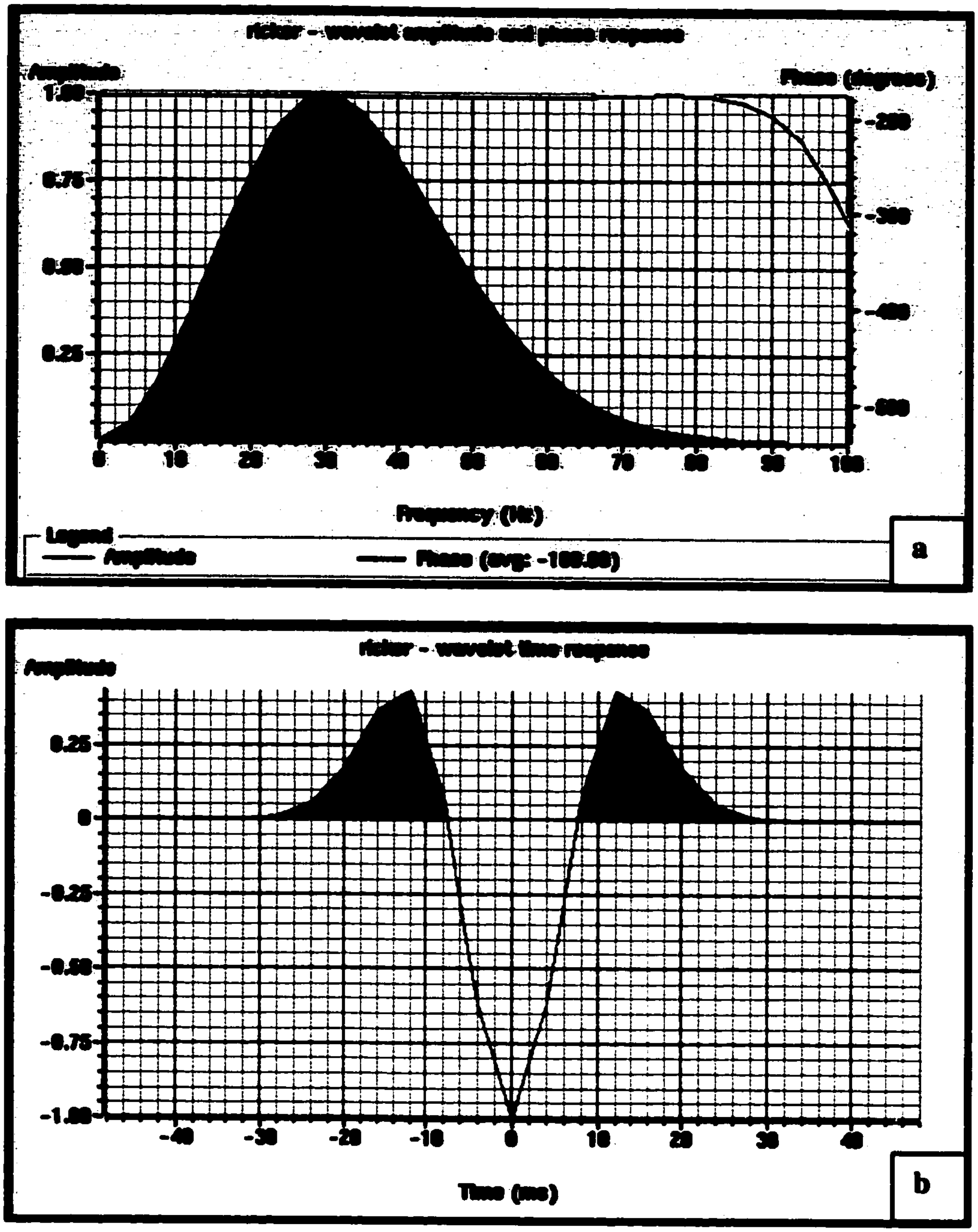

Figure 6: Wavelets dominant in seismic data in the vicinity of wells were extracted after correlation was established. The best wavelets were then averaged to produce the estimated wavelet to be used in inversion: a) In frequency domain b) In time domain

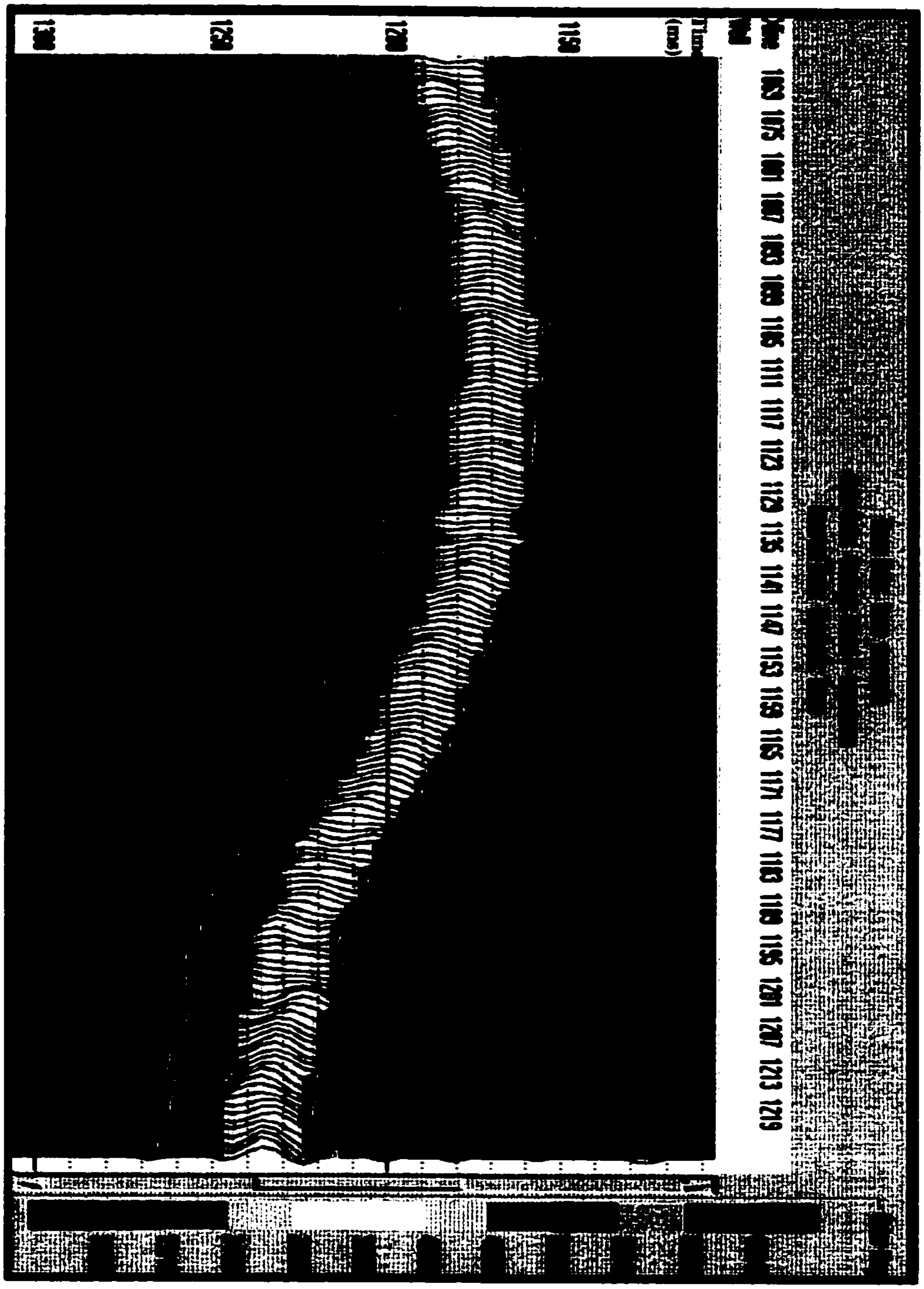

Figure 7: The initial guess model, which consists of an impedance log, was derived by multiplying real sonic logs by real density logs. The interpolation and extrapolation were carried out along the defined stratigraphic boundaries of the Arab-D reservoir (blue lines)

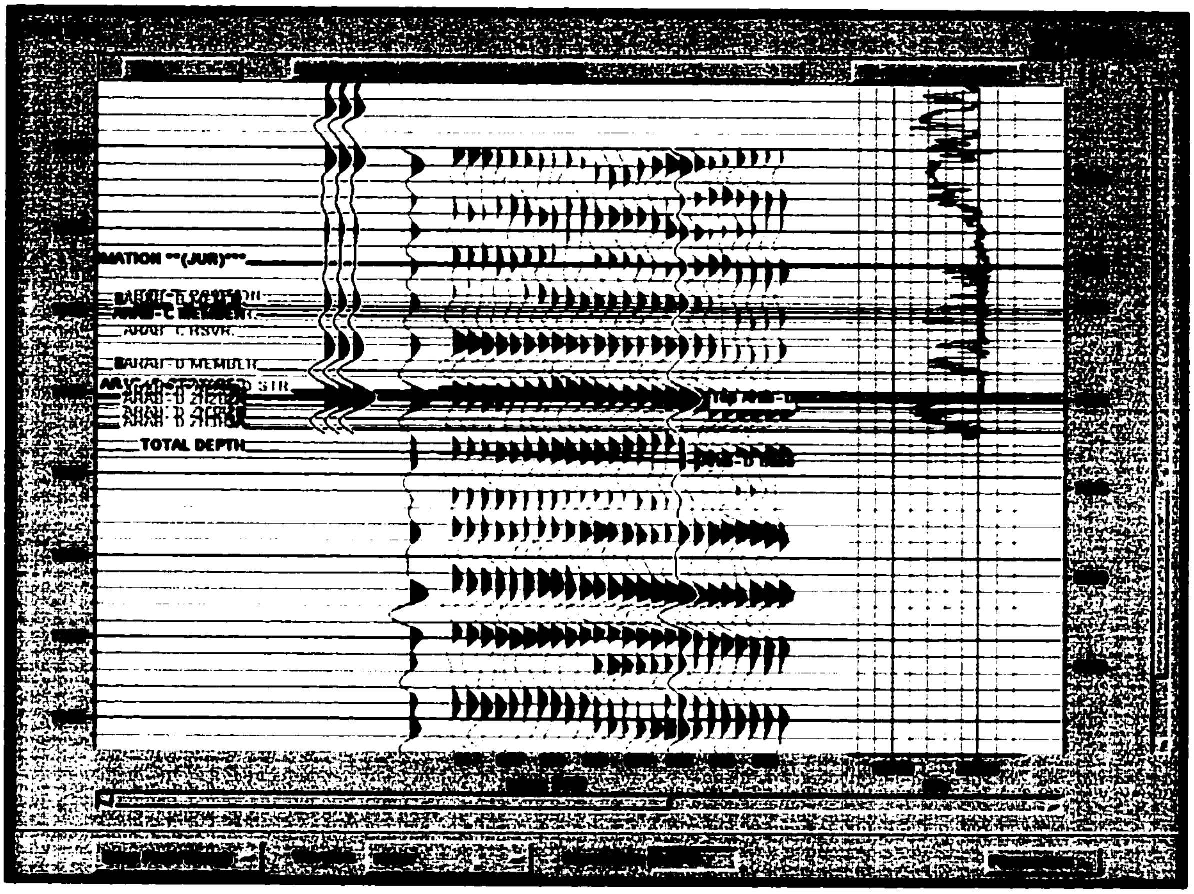

Figure 8: Seismic-well tie was performed searching for the best tie between events picked on well logs and events interpreted on the impedance model: Logs shown in red color, synthetic trace in blue color and seismic in grey

wells are more tied to the seismic data. Stratal surface interpretation is refined as the integration process leads to a clearer understanding of the geological character of the field. Before inverting the seismic data, inversion analysis was performed to test validity of the model-based inversion. The algorithm proven quality performance and gave an absolute error of 0.036 (Figure 9).

Inversion was finally applied for the whole section. The initial guess is a series of equal travel-time layers and as the inversion proceeds, the actual thickness of these layers needs to be modified to optimize the match to the seismic data. Hence, an average block size equal to the seismic sampling interval was assigned to reach this goal. A constraint was used to impose fixed boundaries on the calculated impedance. At each step, the impedance parameters can move freely as long as they don't cross the fixed boundaries. The reason why this process needs to be constrained is to prevent small amount of noise in the data, or modeling errors, from driving the algorithm in the wrong direction. The constraint is set to maximum impedance change of 25%, which is the maximum allowable deviation in impedance as a percentage of the average impedance of the constraint log. Then the final impedance at sample I, I(i), must satisfy:

$$I(i) = I_o(i) \pm 0.25 I_{AV} \tag{3-3}$$

Where: $I_o(i)$ = the initial guess impedance at sample i

I_{AV} = the average impedance of the input constraint, I_o

A conjugate-gradient algorithm was used to change the initial guess model into the final velocity structure. Fifty iterations were calculated in this process for more accuracy.

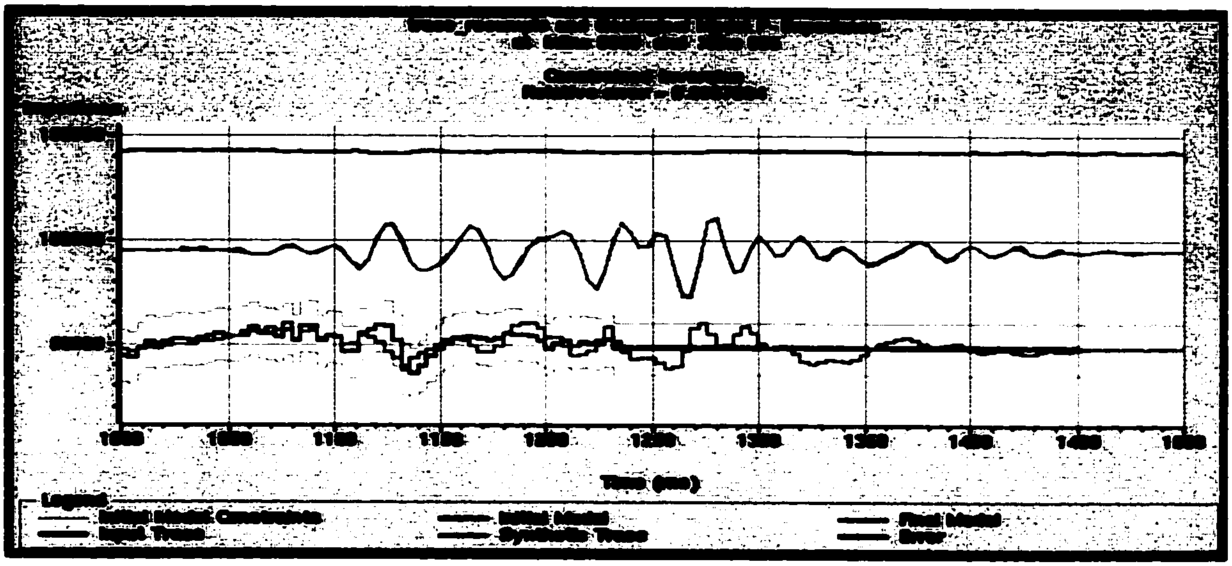

Figure 9: Diagram showing the accuracy obtained using the generated inversion model. The model-based inversion algorithm proven quality performance and gave an absolute error of 0.036

As a result, an accurate high-resolution impedance model was gained providing the basis for easy lithological interpretation and further petrophysical modeling.

3.2. LITHOFACIES MODELING

Seismic interpretation begins with the identification and mapping of significant reflectors (horizons), and the construction of a structural framework where appropriate. However, the finality of this exercise is to predict not only trap closure, but also lithology. Well information and/or model based on sedimentology must be applied to the seismic data, and the necessary relationships must be validated.

Seismic modeling used to stick to only two methods of applying seismic attributes for reservoir characterization. The first method is the computation of a plethora of interval and surface seismic attributes, and subsequent fitting of well information or depositional models to the resulting maps. Typically, a large number of attribute maps are culled down to few relevant maps. The final fitting is always based on empirical relationships. The second method is the classification of seismic data or seismic inversion using available well information. The fundamental flaw that might result from this is the assumption that the well data are representative of the diversity of geological information, that is, no other significant geological facies exit. Once seismic attributes are calibrated to well information, the final data integration and model building process might include the use of geostatistical technology. The flaw in the previously described process is the absence of two vital pieces of information: the overall seismic signal variability and the areal distribution of variability. Interval attributes are only a numerical value calculated from the seismic signal (amplitude, phase, frequency, etc.), and none of them individually characterize the signal heterogeneity. Without knowledge of the overall signal variability, reliable assessment at well locations is difficult. For instance, extrapolation of this information away from well is unreliable, especially if one doesn't know how the well log information relates to the total seismic signal variability.

3.2.1. SEISMIC FACIES CLASSIFICATION

A new classification method was introduced to overcome the flaw associated with seismic attribute classification and seismic inversion. The new Seismic facies classification is a robust technique, which effectively reveals the interrelationship between petrophysical properties and lithofacies distribution and provides an additional tool to verify the inversion model. This function helped assess the seismic signal variability within the interval of interest. The signal was analyzed using Neural Network Technology (NNT) and categorized signal shapes into discrete seismic facies. Besides, attribute maps and other analytical processes are applied to the data such as azimuth and dip maps. These were compared to and incorporated in the seismic facies maps in a methodological manner to validate and optimize accuracy of lithological modeling. Dip/azimuth maps have been applied by Shell to improve reservoir mapping. In particular minor fault- and fracture-identification and mapping can benefit from these attributes (Sonneland et. al., 1990). Dip and azimuth maps are commonly used to detect major and minor (faults for example). The values of the dip map are in degrees from a horizontal reference. Azimuth is measured with respect to inline direction initially and the true dip is then calculated taking the inline orientation with respect to true north. In addition, seismic variability observed at wells could be related to the seismic facies, making calibration of the two data types more realistic because the total range in signal variability was captured in the seismic facies map.

3.2.2. CLASSIFYING TRACE SHAPE

Changes in any of the physical parameters of the seismic signal are always reflected in a change in the shape of the seismic trace. These changes are due to lateral and vertical changes in the reservoir properties. The classification process is based on variations in the shape of the seismic trace (Addy, 2001). Shape is quantified as the rate of change (slope) of sample from one sample point to another along the trace, i.e. is the change strongly negative, positive, or almost nil. Note that the actual amplitude values are not very significant as opposed to overall shape of the seismic trace. The approach follows two steps: first, identifying typical trace shapes, then each trace will be assigned to one of the typical shapes based on similarity.

Neural networks, utilized in this approach, can be briefly defined as a branch of artificial intelligence computing that addresses mainly shape recognition. The algorithms mimic human mind's process of identifying the discriminant characteristics of objects, and making it possible to make associations with other objects of a similar nature. The NNT operates iteratively in two phases: the training session and the classification. In the training session, the program learns or educates itself through a number of iterations, to identify discrete seismic trace shapes from a predefined data training set and constructs a set of model traces. By a self-orienting trial and error process, the synthetic traces are changed at each iteration in search of a better correlation to the actual data. In the classification phase, the model classes are compared to the actual seismic data on a trace-by-trace basis. Each actual trace is then assigned to a discrete seismic facies class based on "goodness of fit" criteria. The final result is a panel of model traces that collectively represent the diversity of signal shape over the entire area covered by seismic interval.

3.2.3. SEISMIC FACIES MAP: CREATING AND PROCESSING THE MAP

Interval on which processing will be performed was selected, with time thickness of 40 milliseconds, which is confined to the Arab-D reservoir. Neural network was trained on the whole 3-D seismic survey of the study area and all traces within the coverage were used for fifty iterations to achieve the best training. Generally, neural network process quickly reaches an 80% solution, only after ten iterations. Different numbers of classes were assigned according to the desired number of facies to model. Three numbers of classes were chosen to give a fair spread and to help search the best resolution. They were also chosen objectively to reflect realistically the geology of the area based on the available geological information. Thus, seven classes were firstly used to map reservoir lithology based on the number of facies available according to Dunham classification. Another trial was done with 21 classes based on Exxon classification of 1987 on the Arab-D reservoir in Uthmaniyah field. A last trial was made with a number of fifteen classes to try in between. Model traces were created and the cumulative difference from one model trace to the other was reviewed using a cumulative difference curve, which displays relative variation. This curve was found to be almost straight in the final trial, representing the maximum differences between traces and indicating that the number of iterations and the number of models were sufficient and there were no intermediate shapes encountered in the data (Figure 10).

After creating and quality controlling the model traces and processing the initial facies map, seismic data were classified (Figure 11). Eventually, three lithofacies maps

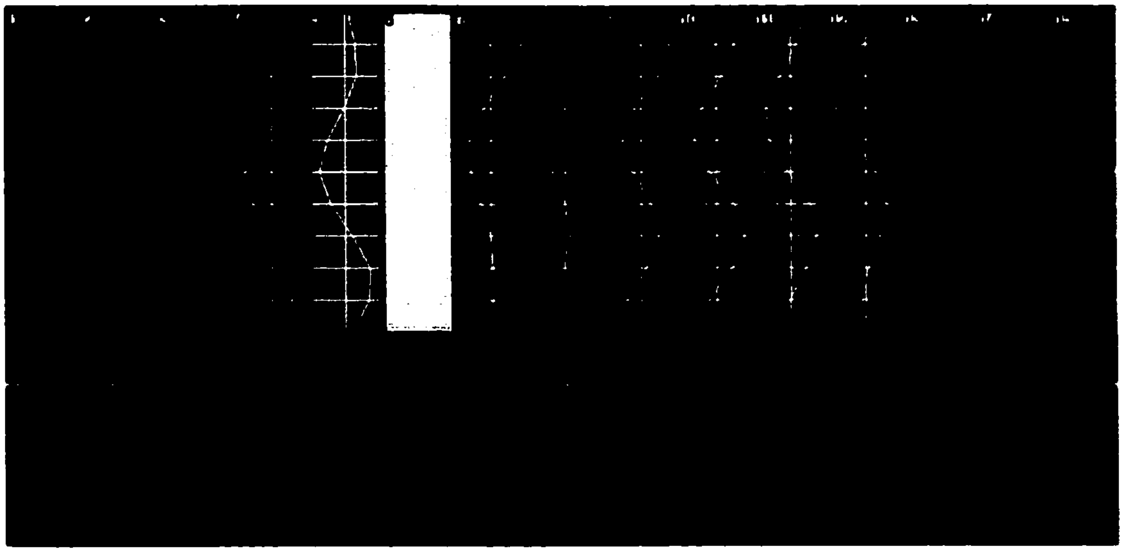

Figure 10: Seismic trace models: the number of models were considered sufficient and there were no intermediate shapes encountered in the data since the cumulative difference curve was found to be almost straight

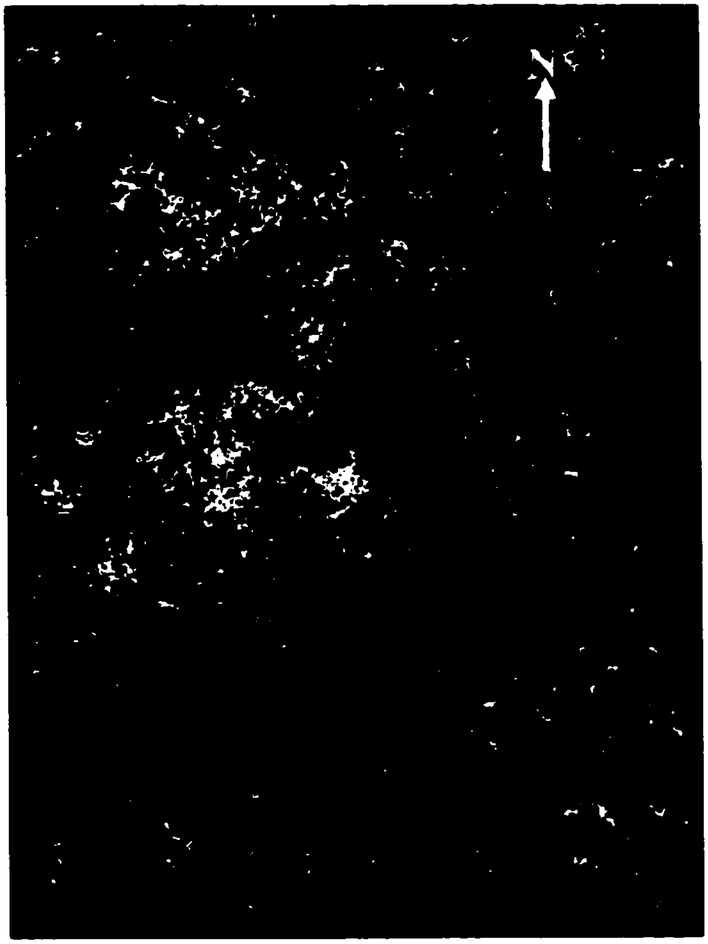

Figure 11: Seismic classification map showing the lateral distribution of the seismic facies

with different classes were generated. Each map was associated with a correlation map, containing the correlation values for each trace relative to the model to which it was assigned. The maps were also assessed by projecting facies information on seismic sections to visually check how lithofacies distribution and signal variability are coinciding.

The last step in the classification was the processing of multiattribute seismic facies maps, which greatly enhance visualization of facies distribution. The purpose of this step is to use another methodology to investigate seismic variation within an interval using various attribute maps such as horizons attribute maps (e.g. average amplitude and dip and azimuth maps), interval attribute maps (e.g. isochron and amplitude maps), and seismic facies. Mainly, amplitude, strongest events, statistical peak and trough and azimuth/dip maps of the horizons, amplitude and isopach maps of the interval, and the three seismic facies maps were incorporated into the new maps. Just as in the shape classification seismic facies, multiattribute seismic facies analysis uses the NNT. However, in multiattribute analysis, clusters of values are classified instead of trace shape. Dip-azimuth maps (Figure 12), which reveal the structure of the interval, have greatly improved the seismic facies maps. This is attributed to the tremendous effect of structural relief on carbonate deposition.

Well information was fitted to the seismic data by projecting a synthetic trace from the well on the seismic section and comparing it with the seismic trace passing through that well. To correct for difference in time when comparing the two traces, the synthetic trace was shifted in time. Synthetic traces could then be correlated with model traces and even substitute a model trace that showed the best match. This also provides another tool

Figure 12: Dip-azimuth map of the bottom of Arab-D reservoir could reveal the structure of the interval and have greatly improved the seismic facies maps. This is attributed to the tremendous effect of structural relief on carbonate deposition

for quality control when checking the model trace of the facies map in the area of the well being projected on the facies map.

3.2.4. QUALITATIVE PETROPHYSICAL ANALYSIS

Seismic signal variations identified on the seismic facies maps are finally related to changes in reservoir characteristics using well information. Thus, seismic facies maps could be calibrated to petrophysical properties such as porosity, density, permeability and acoustic impedance (Poupon et. al., 1999). The process entirely depends on perturbing geological and geophysical parameters by editing physical properties such as thickness, bulk density and bulk velocity and their effect on signal variability can be detected. Thus, a good idea about properties control on signal variability will be obtained. Porosity, density, permeability are also edited to calculate the optimal values for these properties that give the best match between synthetic and real seismic in any specific defined layer or interval.

CHAPTER FOUR

GEOSTATISTICAL AND PETROPHYSICAL MODELING

4.1. GEOSTATISTICAL MODELING

4.1.1. UNIVARIATE STATISTICS

At most basic level, all data are simply numerical values pertaining to some physical parameter. Obviously, these values are a function of some other parameters such as time or distance. Although this is crucial to the final analysis of the data, initially only the values themselves were analyzed. For example, let A represent a collection of N amplitude values. This would be written as:

$A = (a_1, a_2, \ldots\ldots\ldots, aN)$

Although looking at numbers is useful, it has been found that displaying data in graphical forms is the best way to initially visualize its trend. The simplest way to plot A is to assume that the data have been sampled uniformly in either time, depth, or distance. A better way to graph the data would be to reorder the values from smallest to largest in order to estimate the central value or the median.

To quantify this analysis, the statistics of the dataset were determined. The first statistic that was considered is the arithmetic mean, which is simply the sum of the amplitudes divided by the total number of amplitudes. Mathematically it can be written as:

$$m = \frac{1}{N}\sum_{i=1}^{N} a_i = arithmetic\ mean \qquad (4\text{-}1)$$

Next, the variance and the standard deviation values for the data sets were calculated. The variance is the sum of the squared values minus the mean:

$$\sigma^2 = \frac{1}{N}\sum_{i=1}^{N}(a_i - m)^2 = \text{var}iance \qquad (4\text{-}2)$$

From the variance, standard deviation was simply calculated by taking the square root.

4.1.2. RANDOM VARIABLES AND PROBABILITY DISTRIBUTIONS

The concept of the random variable is deemed as one of the most fundamental concepts in statistical theory since it plays an important role in the subsequent advanced geostatistical analyses. A random variable is a variable whose values are randomly generated according to some probabilistic mechanism. Thus, a random variable can take on a series of N outcomes, each with a given probability of occurring. In symbols:

Z = a discrete random variable,

z_i, i = 1, ….., N = occurrences of Z

p_i, I = 1, …..,N = probability of each z_i.

That is, for the ith measurement of Z, called z_i, its probability of occurrence is p_i. Also, the probability of values sum to 1 and must be greater than, or equal to, 0. In symbols:

$$\sum_{i=1}^{N} p_i = 1 \tag{4-3}$$

$p_i \geq = 0$, for all i = 1,........, N.

Probability can be thought of as following some type of distribution functions. There are two types of distribution functions, the probability distribution function, or pdf:

$$f(Z_i) = p_i \tag{4-4}$$

and the cumulative distribution function, or cdf:

$$F(Z_i) = \sum_{j=1}^{i} p_j \tag{4-5}$$

For very large numbers of measurements, what is termed the Gaussian distribution is often approached, with a continuous pdf defined as:

$$g(x) = \frac{1}{\sigma}\sqrt{2\pi}\exp\left[-\frac{1}{2}\left(x - {}^{m}\!/_{\sigma}\right)\right] \tag{4-6}$$

The cdf of a Gaussian function does not have an analytical form, but can be computed by integrating or summing the pdf.

Using the concept of the random variables, the mean and variance can be defined in a slightly different way. The mean of a random variable is referred to as the expected value and is different in that it is weighted by the probability. In symbols:

$$E\{Z\} = m = \sum_{j=1}^{N} p_i z_i = Expected\ value \tag{4-7}$$

The variance of a random variable is the expected squared deviation of Z and its mean:

$$Var\{Z\} = \sigma^2 = E\{(Z - m)^2\} \tag{4-8}$$

$$= \sum_{i=1}^{N} p_i (z_i - m) \tag{4-9}$$

Geological complexity implies that knowledge of a certain reservoir parameter at a drilled location does not allow us to predict with full confidence the value of that parameter at undrilled location. Therefore, geostatistics recognizes this uncertainty by treating the value at each location as a random variable given that some assumptions about the statistical characteristics of the phenomena under study have been made (Hampson-Russel, 2000).

4.1.3. BIVARIATE STATISTICS

If a function of two variables is considered, the problem becomes more difficult. There are many cases in geology where two types of measurements are made to reveal a certain property. Obviously, the first thing that would be thought of with these two sets of measurements is cross plotting them on an x-y graph. This is called cross plot or scattergram, which has been utilized here to plot petrophysical properties against the dense seismic data, searching for a meaningful relationship that would contribute a lot to further modeling.

The first thing done with the cross plot is trying to fit some type of curve to it. The simplest type of curve is a straight line and performing this type of fit is called a linear regression analysis. In this case, the formula can be written as:

$$y = a + bx \tag{4-10}$$

where: a = intercept

b = slope

In all analyses carried out through this study, the slope is found to be negative, which is as would be expected. That's as porosity and permeability increase, acoustic impedance is expected to decrease. It's also obvious that the observed fit is not good because the points obviously do not fall on the regression line. It may be instructive to look at how this regression line was derived. In this case the least-squares methods was used, which tries to minimize the sum of the squared error between the points and their vertical distance to the regression line. The problem with simply looking to the regression lines is that there will be no idea of the magnitude of this error. This will lead to a discussion of the statistics between two variables, or how similar are the two data sets?

There are two ways to look for the degree of similarity of the two variables. Either to take the sum of their differences (or difference squared) or the sum of their products. The sum of their difference is the easiest visualize and here will be considered first. If a set of numbers is graphed against itself, the result will be a straight line at 45°. If the numbers are from two different datasets, they will deviate a way from this straight line and the amount of deviation will determine how well the numbers fit each other. An obvious measure of the deviation is the sum of the squared normal distances a way from the 45° line. This can be expressed as:

$$\gamma = \frac{1}{N}\sum_{i=1}^{N} d_i^2 = \frac{1}{2N}\sum_{i=1}^{N}(X_i - Y_i)^2 \tag{4-11}$$

Where d_i = normal distances of points from the 45 degree line

N = numbers of points

$i = 1,2,3,\ldots\ldots, N$

X,Y =the coordinates of the point

The previous equation is defined as the semi-variogram and measures the scatter between x and y values in a quantitative way. The second measure of similarity between the two data sets is found by taking the sum of the products, or:

$$\text{Product Sum} = \frac{1}{N}\sum_{i=1}^{N} X_i Y_i \tag{4-12}$$

Actually, this calculation will be biased by the mean values of the two datasets. By defining the mean values of x and y as:

$$m_x = \frac{1}{N}\sum_{i=1}^{N} x_i \tag{4-13}$$

$$m_y = \frac{1}{N}\sum_{i=1}^{N} y_i \tag{4-14}$$

The covariance (C) can then be defined by removing the product of the means as shown:

$$C = \frac{1}{2}\sum_{i=1}^{N}(x_i - m_x)(y_i - m_x) = \frac{1}{2}\sum_{i=1}^{N} x_i y_i - m_x m_y \tag{4-15}$$

Thus when x = y, C = σ. That is, the variance of x equals the autocovariance of x. An alternative would therefore be:

σ_x^2 = variance of x

σ_y^2 = variance of y

σ_{xy} = covariance of x and y

Another measure of correlation that is often used is the correlation coefficient, ρ, which can be written:

$$\rho = {}^{\sigma_{xy}}\!/_{\sigma_x \sigma_y} \tag{4-16}$$

The correlation coefficient is one of the most widely used measures of "goodness of fit". Obviously the best correlation coefficient is:

$$\rho = {}^{\sigma_{xy}}\!/_{\sigma_x \sigma_y} = 1.00 \tag{4-17}$$

Finally, it can be shown that the variogram and the covariance can be related as follows:

$$2\gamma_{xy} = \sigma_x^2 + \sigma_y^2 + (m_x - m_y)^2 - 2\sigma_{xy} \tag{4-18}$$

4.1.4. SPATIAL CONTINUITY

In spatial analysis, the variogram and the covariance functions are considered as functions of offset. The offset actually refers to the offset from one sample location to another (Olea, 1994). The variogram and the covariance as a function of offset can be computed by binning the data into a number of separate offset bins and then computing the variogram value in each bin using the formula:

$$\gamma(h) = \frac{1}{2} N \sum_{hij=h} (\phi_i - \phi_j)^2 \qquad (4\text{-}19)$$

where: h = offset.

That is, all the pairs of points (locations) are separated by approximately h and the average of the sum of their differences squared is found. In the case of binned data, h defines the offset to the center of the bin and all offsets between h – (Δh/2) and h + (Δh/2) are included, where:

$$\Delta h = \frac{\max \mathit{offset} - \min \mathit{offset}}{\mathit{number\ of\ offset} - 1} \qquad (4\text{-}20)$$

The following figure shows a theoretical variogram with the nugget, range and sill annotated and the smooth curve showing modeled variogram.

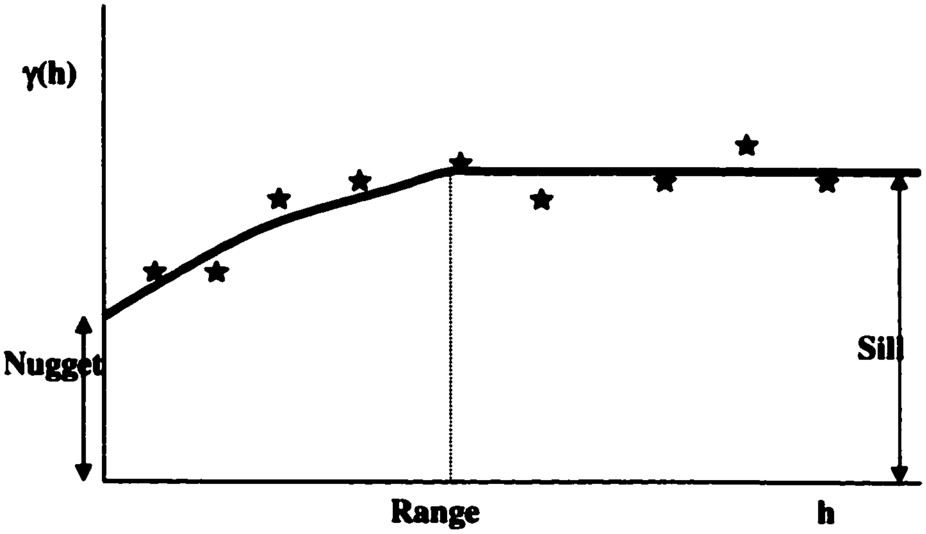

The range is the offset distance at which the curve flattens off to a plateau. This value is of crucial importance and defines the distance at which the differences between points (wells) become random. Another way of looking at the range is that it represents the maximum offset of the smooth structures present in the data. The value of the plateau is called the sill. The value at zero-offset is called the nugget and it affects maps created using the variogram such as kriged maps. Key points about the variogram are:

1) The variogram is a measure of spatial continuity and contains all the information necessary for geostatistical estimation.

2) The variogram is analogous to the autocorrelation function in time series analysis.

3) The variogram may be anisotropic, i.e., it may change with different directions.

Besides, the covariance can be calculated as a function of offset using the formula:

$$C(h) = \frac{1}{2} \sum_{hij=h} \phi_i \phi_j - m_{-y} m_{+y} \tag{4-21}$$

where: m_{-h} = mean of pairs of points in the –h direction.

m_{+h} = mean of pairs in the +h direction.

A second way of driving the covariance function is to use the variogram itself. As explained earlier, the covariance is related to the variogram in the following way:

$$C(h) = \gamma(\infty) - \gamma(h) = C(0) - \gamma(h) \tag{4-22}$$

where: $\gamma(\infty)$ = sill

C(0) = zero offset covariance

It's noticed that only smooth functions of offset, h was assumed but no details of variogram modeling were discussed. Basically, there are four main functions that are used to model variograms:

1) Spherical: $\gamma(h) = C * \left[1.5 * \left(\frac{h}{a}\right) - 0.5 * \left(\frac{h}{a}\right)^3\right], \quad h \le a$

$= C, \quad h \succ a$

2) Exponential: $\gamma(h) = C * \left[1 - \exp\left(\frac{h}{a}\right)\right]$

3) Gaussian: $\gamma(h) = C * \left[1 - \exp\left(\frac{h^2}{a^2}\right)\right]$

4) Power: $\gamma(h) = C * h^n$

If n = 1, that is called a linear model.

In the above models: h = offset

a = range

c = sill (except for the power model, which has no sill)

n = exponent

In addition, each model can have an effect added to its basic shape:

$\gamma(h) = \gamma 0 + \gamma(h),$

where: γ0 = nugget

4.1.5. ORDINARY KRIGING

Kriging is a technique for creating a gridded map of sparse data using what is termed BLUE, or Best Linear Unbiased Estimation, which means:

Best: This is obviously a value judgment, but the method is considered best because it minimizes the variance errors.

Linear: The result is a weighted linear combination of the input.

Unbiased: The mean residual error is set to zero.

Estimation: The final answer is an estimate, not the ground truth.

Obviously, the above goals are very ambitious since neither the mean nor the variance of the full data set is known and therefore cannot be in theory guaranteed that the mean will be zero, or the variance minimized. This is where the theory of random variables comes in. The mean and variance of the data itself may not be known, but a probability model, in which the mean and the variance are assumed to be known, can be built (Hampson-Russel, 2000).

From point (2) it can be noticed that kriging is nothing more than a procedure by which an unknown value on a map is estimated by a linearly weighted sum of the existing values. Written as an equation for N values:

$$Z_0 = w_1 Z_1 + w_2 Z_2 + \dots\dots\dots + w_N Z_N \qquad (4\text{-}23)$$

From point (3), the unbiased assumption, the residual error can be set to zero:

$$E\{Z_0 - Z_0^{'}\} = E\{Z_0\} - E\{Z_0^{'}\} = 0 \qquad (4\text{-}24)$$

Where: Z_0 = the true value and

$Z_0^{'}$ = the estimated value.

From point (1), the variance of the error needs to be minimized:

$$\partial Var\{Z_0 - Z_0^{'}\} / \partial w_i = 0 \qquad (4\text{-}25)$$

Since the error variance can be expressed as a covariance function, the solution turns out to involve only the covariance. Thus the final solution can be written:

$$\sum_{j=1}^{n} w_j C_{ij} = C_{i0} \qquad (4\text{-}26)$$

A striking advantage of kriging not available in traditional estimation methods is that the kriging algorithm honors the data at sample locations. Also the ability of kriging to model anisotropy is another advantage over the traditional methods including the inverse distance squared methods (Wolf et. al., 1994). Another advantage of kriging over these methods is its declustering ability. Because in inverse distance methods the weights given to sampled data are solely dependent on the distance to the estimated point. This results in weighting the sampled points, which are closer to the estimated point more heavily. Whereas, in kriging, weights are not only determined by the distance between the data and the estimated point, but also on the data configuration or the distances between the sampled data points themselves. Therefore, weights are adjusted for any clustering of the data.

In simple kriging, the mean of the data to be calculated is assumed to be known. Since all the data points have not been sampled, the mean cannot be known. In ordinary kriging, to get around this problem, it is often assumed that the weights are unbiased, or sum to one. In equation form:

$$\sum_{i=1}^{n} w_i = 1 \tag{4-27}$$

If this constraint is added to the derivation of the kriging equations, the result is added as an extra row and column to the kriging equations. That is, the n x n simple kriging equations become the (n+1) x (n+1) ordinary kriging equations shown here:

$$\begin{bmatrix} C_{11} & . & . & C_{1n} & 1 \\ . & . & . & . & . \\ . & . & . & . & . \\ C_{n1} & . & . & C_{nn} & 1 \\ 1 & . & . & 1 & 0 \end{bmatrix} \begin{bmatrix} w_1 \\ . \\ . \\ w_n \\ \mu \end{bmatrix} = \begin{bmatrix} C_{10} \\ . \\ . \\ C_{n0} \\ 1 \end{bmatrix} \tag{4-28}$$

or: $C'W = D'$

with solution: $W = (C')^{-1} D'$ (4-29)

where: C' = matrix containing covariance values between two points (constrained)

W = kriging weights as a vector and

D' = vector containing covariance values between the unknown and the known points (constrained).

4.1.6. CROSS VALIDATION

Cross-validation is a very useful procedure to check for systematic errors in the dataset. Very simply, cross-validation can be thought of as running the kriging process on the whole dataset except for one value and then comparing the predicted value at this location to the known value. If this is done for the each value in the dataset, a plot of the miss-fit error can be made at each value (Wolf et. al., 1994).

4.1.7. THE MARKOV-BAYES (LINEAR) ASSUMPTION

Often, a linear relationship between sparse (well) data and dense (seismic) data is set up. This is referred to as the Markov-Bayes Assumption. The purpose of setting up this relationship is to aid in the modeling of variograms and to handle the trend in the dense data (Hampson-Russel, 2000).

Geostatistical calculations, such as cokriging and cosimulation, which use the secondary dense variable to estimate the primary variable, assume that there is some linear relationship between them. In the conventional application of cokriging, three variograms must be modeled:

1) The well-to well variogram

2) The well-to-seismic variogram

3) The seismic-to-seismic variogram

The resulting variogram models contain implicit information about the linear relationship between the variables, and how well correlated they are. In other words, when these variograms are modeled, a cross-plot between the variables at their common points can be effectively formed, and the slope and the scatter points about the line can be derived. A major problem with variogram modeling is that two of the three variograms depends on a very small sample of data (the wells) and these models may be unreliable.

One solution to this problem is to use an assumed linear relationship to help in modeling the variograms. If it is assumed that, the seismic data is related to the well data as follows:

$$S(x,y) = A * W(x,y) + B + noise \qquad (4\text{-}30)$$

where A and B are constants to be determined and the noise is zero-mean and uncorrelated with the other variables. Then, under these conditions, it can be showed that the required covariances are related by:

$$Cov_{ss}^{(h)} = \left(1/N\right) * \sum s(x+h) * s(x) - \left(1/N^2\right) * \sum s(x+h) * s(x) \qquad (4\text{-}31)$$

$$= A^2 * Cov_{ww}^{(h)} + Cov_{nn}^{(h)} \qquad (4\text{-}32)$$

$$Cov_{ws}^{(h)} = A * Cov_{ww}^{(h)} \qquad (4\text{-}33)$$

In other words, if the slope, A and the noise covariance, $Cov_{nn}^{(h)}$, are known, all three covariances can be calculated from knowledge of any one of them.

Both the slope and the noise covariance can be estimated from a cross-plot of the dense data versus the sparse data at those points where they both exist. Instead, of using the noise covariance directly, the normalized correlation between the two variables must be used:

$$\rho = Cov_{ws} / [Cov_{ww} * Cov_{ss}]^{1/2} \tag{4-34}$$

This is a number which varies between −1 and +1 such that:

−1 = perfectly correlated with negative slope

0 = no correlation whatsoever

+1 = perfectly correlated with positive slope

The practical effect of the normalized correlation measure is that if the correlation is large, then in cokriging, the secondary (seismic) data will have a larger impact on the result. Conversely, if the correlation is small, then in cokriging, the secondary (seismic) data will have a small impact on the result.

4.1.8. COKRIGING

Often, two sets of variables are available, one sparse but exact such as well data, the other dense but not exact such as seismic data, giving us information about the physical parameter. The extension of kriging to operation that allows exploitation of information in both datasets is called cokriging.

Intuitively, if two sets of data u and v are available, it would seem that the extension of kriging to cokriging would involve a double set of weights (Xu et. al., 1992):

$$u = \sum_{i=1}^{n} a_i u_i + \sum_{j=1}^{m} b_j v_j \tag{4-35}$$

where: a_i, i=1, n represent the weights on one input dataset,

b_j, j=1, m represent the weights on the second input dataset.

By recalling that in kriging, simply the well-to-well covariance function is required. In cokriging, two other variograms are required: the seismic-to-seismic variogram and the well-to-seismic variogram. These can be written in symbols:

Cov{uu} = well-to-well covariance

Cov{vv} = sesmic-to-seismic covariance

Cov{uv} = well to seismic covariance.

Then, cokriging system of equations can be written as an n + m + 2 set of equations:

$$\sum_{i=1}^{n} a_i Cov\{u_i v_j\} + \sum_{i=1}^{m} b_j Cov\{v_i v_j\} + \mu_1 = Cov\{u_0 v_i\} \tag{4-36}$$

$$\sum_{i=1}^{n} a_i Cov\{u_i v_j\} + \sum_{i=1}^{m} b_j Cov\{v_i v_j\} + \mu_2 = Cov\{u_0 v_j\} \tag{4-37}$$

$$\sum_{i=1}^{n} a_i = 1$$

$$\sum_{i=1}^{n} b_j = 0$$

4.1.9. STOCHASTIC SIMULATION

Stochastic simulation involves creating a series of equally probable realizations, or models, of a random variable. Each model, or stochastic image, depends on the assumptions that have gone into the simulation procedure. The most popular type of simulation is called conditional simulation, which honors the hard data values at measured locations (Srivastava, 1994). Since it has had conditions placed on it. Although there are several algorithms used to perform stochastic simulation, the most common is called Sequential Gaussian Simulation (SGS) and this is the procedure, which was used in this study to model porosity of the Arab-D reservoir.

The main steps in performing SGS can be described as follows:

1) Setting of all grid cells and insertion of the known sparse data points at their correct locations.
2) Selection of a point randomly using a random number generator. Estimation of the value at that point using Ordinary Kriging (wells alone) or collocated cokriging (wells plus seismic).
3) The estimate at that point consists of a value plus a variance (standard deviation). By assuming a Gaussian distribution with these parameters, the value assigned to this point can be determined by a random number generator. Because of the Gaussian distribution, grid points far from wells will have larger variances and thus a higher probability of getting a value significantly different from the kriging estimate.

4) Insertion of the estimated value at the grid location. Selection of a new point grid location using a random number generator and repeating steps one to three. The previously derived point is now treated as if was a hard data point.

5) When all grid points have been filled, one map is complete. Creation of another map, which will be different because the grid cells will be visited in a different order.

When performing SGS, the first choice is whether the conditioning data will be the sparse data alone (well data) or will be both the sparse and the dense data (well plus seismic). The choice here determines whether the estimation algorithm will be kriging or collocated cokriging. The rules for these two algorithms apply in the simulation case as well. In particular, kriging requires one variogram model, while cokriging requires three (Hampson-Russell, 2000).

Once a series of maps is created using SGS, they need to be analyzed in some way. The basic assumption in simulation analysis is that each point of the grid contains a probability distribution. The peak in that distribution is the most likely value, given the hard data and the variogram model. The most likely value is also what one would get using conventional kriging or cokriging. The width of the distribution describes the uncertainty associated with the distribution at that point. By creating a large number of simulation maps, it is hoped to reduce the probability distribution at each point of the grid. From these probability distributions, probabilities associated with ranges of the measured parameter are derived.

There are three basic ways of analyzing the result. First is to average all the derived maps. In principle, for a very large number of maps, this should be very similar to ordinary kriging or cokriging. Second is to ask for probability is that the value is somewhere in the range from a low value to a high value. The resulting map shows probability values from zero to one.

Finally, those locations, where the value in the range from low value to high value, can be asked for with a particular confidence level. The confidence level is expressed as a percentage from 0 to 100%. For simplicity, this analytical option has been chosen to determine uncertainty values though this work.

4.2. PETROPHYSICAL MODELING USING MULTI-ATTRIBUTE TRANSFORMS AND NEURAL NETWORK

4.2.1. INTRODUCTION

The integration of the seismic data and the log data has become increasingly important and successful in recent years due to shift from exploration to development of existing fields. One known type of integration is the inverse modeling of synthetic seismic data from logs. A second type of integration is the inverse modeling of the logs from the seismic data, which has also been utilized in this study. The new technique of the neural network transforms goes beyond the limits of conventional inversion technique in several ways. First, it directly predicts rock properties other than acoustic impedance, such as porosity, permeability and water saturation (Zhang et. al., 2001). This differs from modeling porosity achieved in this work using acoustic impedance derived from inversion as a secondary data. A second difference is that it uses attributes derived from seismic data rather than the conventional post-stack data itself. Thirdly, instead of assuming a particular model relating the logs and the seismic, a statistical linear (multivariate regression) or non-linear (neural network) relationship will be derived by analyzing a set of training data at well location.

An empirical relationship between log data and seismic attributes or any other external attributes is determined first, and then information from seismic attributes or external attributes are transformed from the seismic attribute domain to the petrophysical domain. The algorithms use the convolutional model, which uses several seismic samples for the computation of each log value. The neural network applications then take these extra samples and assign weights to them in order to derive a non-linear, weighted combination of multiple attributes that best predict the target rock property. In practice, these algorithms could rigorously enhance seismic resolution and improve reservoir modeling and production. Neural network algorithms have proven to be very useful for reservoir mapping (Gosse et. al., 2000).

This technique was proposed in this study to address the problem associated with permeability modeling using conventional geostatistics. Geostatistical permeability models generated through this study showed serious inadequacy with an average absolute error greater than 13% (187 md). Permeability is an important parameter in a heterogeneous carbonate reservoir characterization since it controls the strategies involving well completion and stimulation and reservoir management. Therefore, permeability is a key parameter that governs in great extension reservoir handling and development (Soto et. al., 2001). Yet, modeling permeability represents the most problematic piece of work in reservoir prediction and characterization since the models explaining permeability are not always bivariate (Log (k) vs. Φ) as all conventional models assume. This necessitated the involvement of a more robust technique that can tackle this problem with higher success. The proposed method has greatly improved the analysis giving better prediction with an absolute average error of about 2% (33md). Porosity models based on this technique proved to be as accurate as geostatistical models and they even showed some advantages over them in that they better agreed with geologic and seismic trends. Accordingly, they were deemed reliable and consequently incorporated in permeability modeling as one of the major attributes to be used in prediction.

4.2.2. MULTI-ATTRIBUTE LINEAR REGRESSION

4.2.2.1. SEISMIC ATTRIBUTES

In this methodology, the aim is to find an operator, possibly non-linear, which can predict well logs from neighboring seismic data. In fact, not the seismic data itself is chosen to be analyzed, but attributes of the seismic data. One of the reasons why this is expected to be more beneficial than the raw seismic data is that many of these attributes will be non-linear, thus increasing the predictive power. Seismic attributes can be defined as any mathematical transforms of the seismic data, such as trace envelope, instantaneous phase, instantaneous frequency, etc. Seismic attributes may be divided into two categories, horizon-based attributes such as dip and azimuth and sample-based attributes such as envelope and dominant frequency. Only sample-based attributes are considered in this methodology.

4.2.2.2. CONVENTIONAL CROSS PLOTTING

Given a particular attribute of the seismic data, the simplest procedure for deriving the desired relationship between the target data and seismic attribute is to cross plot the two. The assumption is that the target log has been integrated to travel-time at the same sample rate as seismic attribute. Each point in the cross plot consists of a pair of numbers corresponding to a particular time sample. Assuming linear relationship between the target log and the attribute, a straight line may be fit by regression:

$$y = a + bx \tag{4-38}$$

The coefficients a and b in the equation may be derived by minimizing the mean squared prediction error:

$$E^2 = \frac{1}{N}\sum_{i=1}^{N} \left(y_i - a - bx_i\right)^2 \tag{4-39}$$

Where the sum is overall points in the cross plot.

The calculated prediction error, E, is a measure of the goodness-of-fit for the regression line defined by equation (4-39). An equivalent measure is the normalized correlation defined by:

$$r = \frac{S_{xy}}{S_x S_y} \tag{4-40}$$

where:

$$S_{xy} = \frac{1}{N}\sum_{i=1}^{N}\left(x_i - m_x\right)\left(y_i - m_y\right) \tag{7-41}$$

$$S_x = \frac{1}{N}\sum_{i=1}^{N}\left(x_i - m_x\right)^2 \tag{4-42}$$

$$S_y = \frac{1}{N}\sum_{i=1}^{N}(y_i - m_y)^2 \tag{4-43}$$

$$m_x = \frac{1}{N}\sum_{i=1}^{N}x_i \tag{4-44}$$

$$m_y = \frac{1}{N}\sum_{i=1}^{N}y_i \tag{4-45}$$

4.2.2.3. EXTENSION OF CROSS PLOTTING TO MULTI-ATTRIBUTE

Statistical regression has been proposed as more versatile solution to the problem of permeability estimation. Conventional statistical regression has generally been done parametrically using multiple linear models (Lee et al, 1999). The extension of the conventional linear analysis to multiple attributes (multivariate linear regression) is straightforward. If there are (n) attributes, the target log at each time sample is modeled by the linear equation:

$$L(t) = w_0 + w_1A_1(t) + w_2A_2(t) + ... + w_nA_n(t) \tag{4-46}$$

The weights in this equation may be derived by minimizing the mean squared prediction error, as extended from equation (4-39):

$$E^2 = \frac{1}{N}\sum_{i=1}^{N}(L_i - w_0 - w_1A_1 - w_2A_2 - .... - w_nA_n)^2 \tag{4-47}$$

The solution for the four weights produces the standard normal equations:

$$\begin{bmatrix} w_0 \\ w_1 \\ w_2 \\ w_3 \end{bmatrix} \begin{bmatrix} N & \sum A_{1i} & \sum A_{2i} & \sum A_{3i} \\ \sum A_{1i} & \sum A_{1i}^2 & \sum A_{1i}A_{2i} & \sum A_{1i}A_{3i} \\ \sum A_{2i} & \sum A_{1i}A_{2i} & \sum A_{2i}^2 & \sum A_{2i}A_{3i} \\ \sum A_{3i} & \sum A_{1i}A_{3i} & \sum A_{2i}A_{3i} & \sum A_{3i}^2 \end{bmatrix}^2 \begin{bmatrix} \sum L_i \\ \sum A_{1i}L_i \\ \sum A_{2i}L \\ \sum A_{3i}L_i \end{bmatrix} \qquad (4\text{-}48)$$

Just as in the single attribute case, the mean-squared error (equation 4-47) calculated using the derived weights constitutes a goodness-of-fit measure for the transform, as does the normalized correlation, defined in equation (4-40), where the x-coordinate is now the predicted log value and the y-coordinate is the real log value (Hampson et. al., 1999). In most advanced non-parametric algorithms, multivariate statistical analysis is commonly used to ensure quality control, preprocess data, reduce the number of independent variables or determine the dominant variables (Soto et. al., 2000).

4.2.2.4. USE OF CONVOLUTIONAL OPERATOR

The derivation of the multi-attribute regression assumes a single weight for each attribute. The problem associated with this is that the frequency content of the target log is typically much higher than that of the seismic attribute. Consequently, correlating them sample-by-sample basis may not be optimal. The alternative is to assume that each sample of the target log is related to a group of neighboring samples on the seismic attribute as shown in the following figure:

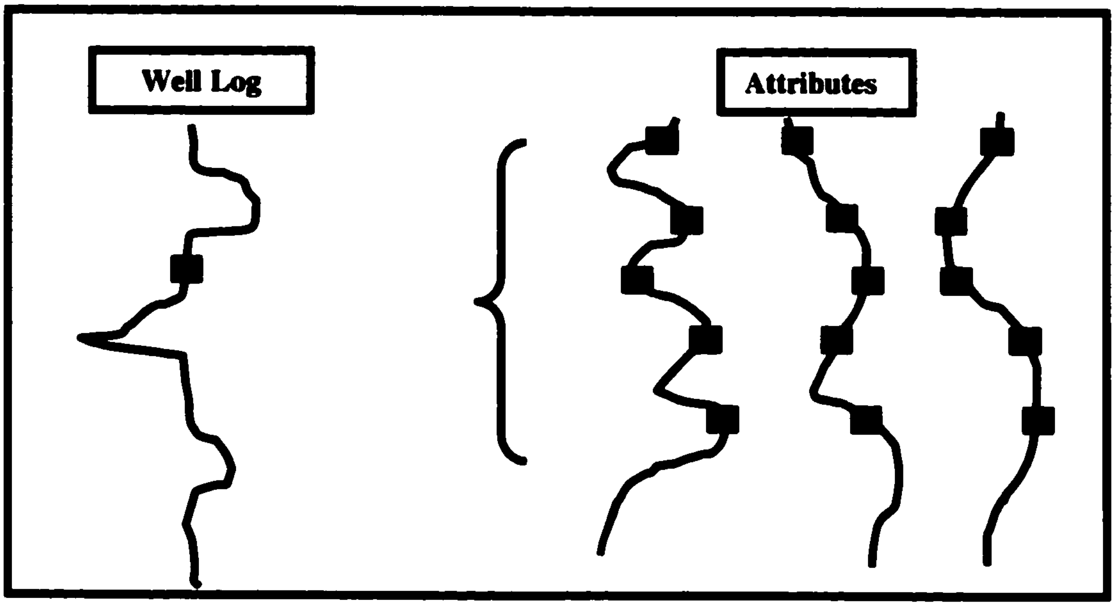

The use of convolutional operator is also suggested by the classic convolutional model in geophysics. If the well log for example, happens to be acoustic impedance, then the previous five-point operator is closely related to the seismic wavelet. In general, for any other log property, the wavelet can be expected to smear the effects of each log sample over a range of contiguous seismic samples. The extension of equation (4-46) to include the convolutional operator is:

$$L = w_0 + w_1 * A_1 + w_2 * A_2 + \dots\dots\dots + w_n * A_n \qquad (4\text{-}49)$$

where * represents convolution, and the w_i are operators of specified length. Once again, the operator coefficients may be derived by minimizing the mean-squared prediction error:

$$E^2 = \frac{1}{N}\sum_{i=1}^{N}\left(L_i - w_0 - w_1 * A_1 - w_2 * A_2 - \dots\dots\dots - w_n * A_n\right)^2 \qquad (4\text{-}50)$$

This is equivalent to introducing a series of new attributes, which are time-shifted versions of the original attributes (Gosse et. al., 2000).

4.2.2.5. DETERMINING ATTRIBUTES BY STEP-WISE REGRESSION

So far, equations, which allow us to determine optimal operators for any given set of attributes, have been derived. These operators are optimal in the sense that the mean-squared prediction error between the actual target logs and the predicted target logs is minimized. The next issue to be addressed is how to select the attributes.

The assumption in the step-wise regression is that if the best combination of M attributes is already known, then the best combination of M+1 attributes includes the previous M attributes as members. Of course, the previously calculated coefficients must be re-derived. The process is illustrated in the series of steps:

Step 1: Find the single best attribute by exhaustive search. For each attribute in the list, such as amplitude weighted phase, average frequency, etc., solve for optimal coefficients and calculate the prediction error. The best attribute is the one with the lowest prediction error. Call this attribute$_1$.

Step 2: Find the best pair of attributes, assuming that the first member is attribute$_1$. For each other attribute in the list, from all pairs. For example, attribute$_1$and amplitude weighted phase, attribute$_1$ and average frequency, etc. For each pair, solve for the optimal coefficients and calculate the prediction error. The best pair is the one with the lowest prediction error. Call this second attribute from the best pair attribute$_2$.

Step 3: Find the best triplet of attributes, assuming that the first two members are attribue$_1$, and attribute$_2$. For each other attribute in the list, form all triplets. For example, (attribute$_1$, attribute$_2$, amplitude weighted phase), (attribute$_1$, attribute$_2$, average frequency), etc. For each triplet, solve for the optimal coefficients and calculate the prediction error. The best triplet is the one with the lowest prediction error. Call this third attribute from the best triplet attribute$_3$. Finally, this process can be carried on as long as desired.

The problem with step-wise regression is that no one can be sure of deriving the optimal solution. However, it can be shown that each additional attribute found has a prediction error less than or equal to the previous smaller combination. This can be proven by contradiction: if the new prediction error is greater, then simply set all the weights to zero for this new attribute, and the prediction error will be equal to the previous set.

The most important advantage of step-wise regression is that it relief us from the need to worry about whether the attributes in the total list are linearly independent. This is because the step-wise regression automatically chooses the next attribute whose contribution in a direction orthogonal to the previous attributes is greatest. Assume, for example, that two of the attribute, say A_i and A_j are scaled versions of each other: $A_j = a + b^* A_i$. This would represent the extreme case of linear dependence. As the step-wise regression proceeds, one or the other of them will be chosen first, say A_i. From then on, the other attribute, A_j, will never be chosen. This is because once A_i is included; the improvement by adding the other attribute, A_j is precisely zero.

At this point the general term multi-attribute transform can be defined. The multi-attribute transform is a set of attribute types along with rules for transforming the attribute into the desired output log (Hampson et. al., 1999). In the analysis so far the transformation are linear weights applied to either the attributes themselves or to non-linear transforms of the attributes. The next section extends this analysis to include neural networks, which can establish non-linear relationships between the target log and the attributes.

4.2.3. PROBABALISTIC NEURAL NETWORK (PNN)

The probabilistic neural network (PNN) is actually a mathematical interpolation scheme, which happens to use a neural network architecture for its implementation. This is a potential advantage, since by studying the mathematical formulation; its behavior can often be understood much better than other neural networks algorithms. The data used by the PNN consists of a series of training examples, one for each seismic sample in the analysis windows from all the wells:

$$\begin{gathered}\{A_{11}, A_{21}, A_{31}, L_1\} \\ \{A_{12}, A_{22}, \mathrm{A}_{32}, L_2\} \\ \cdot \\ \cdot \\ \cdot \\ \{A_{13}, A_{23.}, A_{33}, L_3\}\end{gathered}$$

where there are n training samples and three attributes. The values L_i are the measured target log values for each of the examples.

Given the training data, the PNN assumes that each new output log value can be written as a linear combination of the log values in the training data. For a new data sample with attribute values:

$$x = \{A_{1j}, A_{2j}, A_{3j}\} \tag{4-51}$$

the new log value is estimated as:

$$\hat{L}(x) = \frac{\sum_{i=1}^{n} L_i \exp(-D(x, x_i))}{\sum_{i=1}^{n} \exp(-D(x, x_i))} \tag{4-52}$$

where

$$D(x, x_i) = \sum_{j=1}^{3} \left(\frac{x_j - x_{ij}}{S_j} \right)^2 \tag{4-53}$$

The quantity D(x, x_j) is the distance between the input point and each of the training points x_i. This distance is measured in the multidimensional space spanned by the attributes, and is scaled by the quantity S_j, which may be different for each of the attributes. Equations 7-15 and 7-16 describe the application of the PNN network. The training of the network consists of determining the optimal set of smoothing parameters, S_j. The criterion for determining these parameters is that the resulting network should have the lowest validation error.

Define the validation result for the mth target sample as:

$$\hat{L}_m(x_m) = \frac{\sum_{i \neq m}^{n} L_i \exp(-D(x_m, x_i))}{\sum_{i \neq m}^{n} \exp(-D(x_m, x_i))} \tag{4-54}$$

This is the predicted value of the mth target sample when that sample is left out of the training data. Since the value of this sample is known, the prediction for that sample can be calculated. Repeating this process for each of the training samples, the total prediction error for the data can be defined.

$$E_v = (S_1, S_2, S_3) = \sum_{i=1}^{n} \left(L_i - \hat{L}_i\right)^2 \tag{4-55}$$

Note that the prediction error depends on the choice of the parameters, S_j. This quantity is minimized using non-linear conjugate gradient algorithms. The resulting network also has the property that the validation error is minimized.

4.2.4. VALIDATION

The transforms derived by the neural network technique are applied to the entire seismic volume. Prediction error and uncertainty estimations are performed through a process called cross validation that determines the optimal number of attributes that when combined have the highest predictability. Theoretically, the more attributes used, the lower the prediction error. However, there is a limit to the resolution obtainable depending on the quality of the data and on the physical properties of the reservoirs. Using too many attributes may result in over-training.

Cross-validation allows the transform to be evaluated for its predictive power. It removes a known value from the training set and tries to predict it based on surrounding values. Therefore, in the process of cross-validation, the analysis is repeated, as many times as there are wells, each time leaving out a different well. The total validation error is the root mean square average of the individual errors:

$$E_v^2 = \frac{1}{N}\sum_{i=1}^{N} e_{vi}^2 \tag{4-56}$$

where: E_v is the total validation error

e_{vi} is the validation error for well i, and

N is the number of wells in the analysis

CHAPTER FIVE

RESULTS AND DISCUSSION

5.1. SEISMIC INVERSION ANALYSIS

Inversion of the seismic data into impedance in this work was obviously successful in providing a very effective mean to characterize reservoir in three dimensions. Impedance is often related to critical reservoir properties such as lithology and porosity, which have shown inverse relationship with acoustic impedance (Appendix A). Therefore, impedance models have been known and utilized as major lithological indicators, allowing better delineation and description of complex facies variation.

In the principles of the seismic modeling, if the lithology is assumed to be known, acoustic impedance values can be assigned to each facies (Johnsen et. al., 1996). The most commonly used carbonate reservoir rock classification of Saudi Aramco is entirely based on both original textural variations (amount of mud matrix, particle size) and subsequent diagenetic modification, providing a function to rock density and porosity, which can be directly related to subsequent interpretation of acoustic impedance. Thus, available literature about lithological variation within this reservoir (Daetwyler, 1987) and (Cantrell, 2001) was very useful to interpret the inversion model in terms of rock types. This knowledge rigorously guided the explanation and justification of many enigmatic features present in the impedance model. Hence, a meaningful description of reservoir layering and lithology was quite possible. This led to easier verification of previous studies and opened the door for detailed lithological characterization of this geologically complicated area (Valle et. al., 1997).

Due to the unavailability of a 3-D visualization tool, 2-D slices and cross-sections dissecting the 3-D impedance model of the 40 ms reservoir interval were prepared instead. Eleven depth slices were made at a constant interval of 4 ms to precisely investigate lateral variability through significant zones of the reservoir. The first slice passes through the top of the reservoir and the last slice coinciding with the bottom of the Arab-D reservoir. They were numbered sequentially from top to bottom. Data was carefully explored line by line to study detailed spatial variability and to trace lateral continuity of lithological bodies in the depth dimension.

The first slice (Figure 13), passing exactly at the top of zone 1 of the Arab-D reservoir, showed abnormally high impedance values compared to other zones, reflecting the known lithological nature of this zone, which composed mainly of fully dolomitized limestones intercalated with anhydrites and characterized by very low porosity values. It represents a transition from Sabkha deposition to marine shallow marine (grainstone) deposition. Dolomite typically has a higher grain density and acoustic velocity than limestones (Cantrell et al., 2001). High impedance fully dolomitized limestones and anhydrites are not predominant over the whole zone. Less dolomitized carbonate rocks are also locally present and mainly located in the southeastern area of the survey on the eastern flank of the Uthmaniyah anticline. Other occurrences of these rocks are also seen in northwestern area on the structural highs of the anticline. The high-impedance rocks show a distinctive northeastern trend. Obvious heterogeneity encountered within this zone displays its transitional depositional environment.

Zone 2A, displayed in slice 2 (Figure 14) at 4ms below the top of the interval, shows relatively very low impedance values indicating a good quality porous interval. This zone is known as high-energy subtidal stable grain-flat deposits. It mainly consists of grainstones and calcarenitic limestones (packstones and wakestones) with traces of dolomites (Powers, 1966). Low-impedance rocks are concentrated on the southeastern area of the survey and they also present at the north and the northwestern parts. Whereas, high-impedance rocks are located in the central area showing the same northeastern trend noticed in zone1, which is probably related to fracturing. Most of the major fractures in the study area have a northeastern trend (KFUPM, 2000). However, another northern trend could be recognized. Distinctive rounded high-impedance area is locally seen within the low-impedance region on the flank in the most southeastern area. This feature is most probably caused by local slight dolomitization.

Slice 3 (Figure 15a) cutting through upper zone 2B, shows an increase of the content of high-impedance rocks. This is consistent with the available knowledge about this zone, since it is known that the upper third interval of this zone is extensively dolomitized. Zone 2B consists of a wide variety of lithofacies, all of which are predominantly grain-supported. The micritic lithofacies and mud content increase downward and the effect of dolomitization becomes minimal (Daetwyler, 1987). This gradual change is displayed by the following two slices (slice 4 and slice 5) (Figure 15 b/c), which also show the same trends of high-impedance rocks as the previous slices. Low-impedance rocks are located in the northwestern area at the structural highs as well as in flank area.

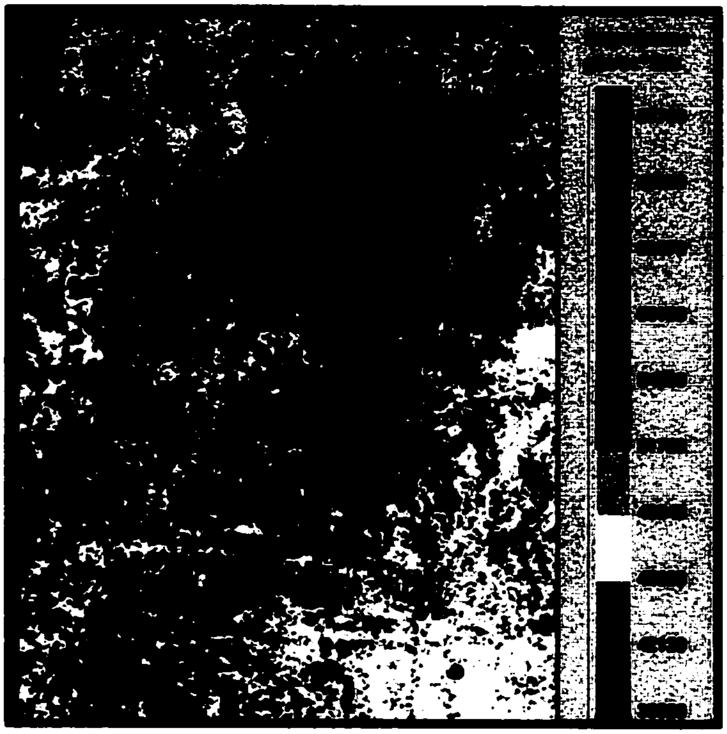

Figure 13: Impedance slice 1, passing through zone1, shows abnormally high impedance values compared to other zones, reflecting the known lithological nature of this zone

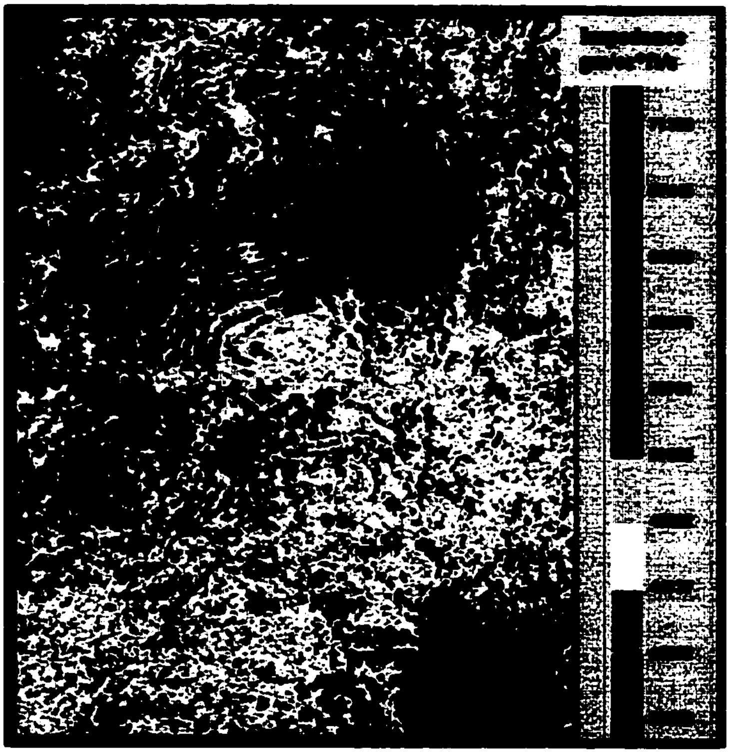

Figure 14: Impedance slice 2, passing through zone 2A, shows relatively very low impedance values indicating a good quality porous interval

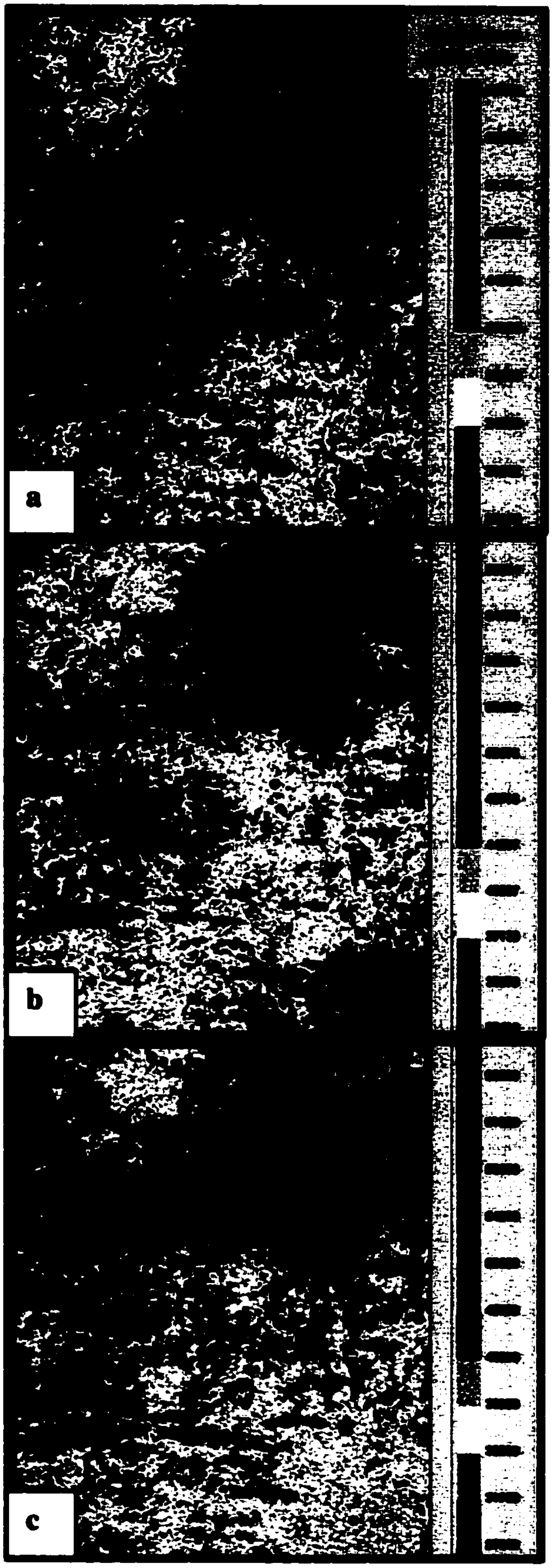

Figure 15: Slices passing through zone 2B:
a) Slice 3 at the upper part of the zone shows an increase of the content of high-impedance rocks due to dolomitization.
b) Slice 4 at the middle part of the zone.
c) Slice 5 at the lower part of the zone. Slices 4 and 5 also displays high impedance values since the mud content increases toward the lower parts. However, low values at present at the structural highs

In zone 3A, it is well known that various grain-supported lithofacies are interbedded with relatively non-porous, micritic lithofacies, whereas dolomite is common to abundant. This explains the relative high-impedance values dominant in this zone as seen in slice 6 and 7 (Figure 16 a/b). Slice 7 dissecting the lower part of the zone, displays higher impedance values than the upper part of the zone due to the increase in mud content and dolomitization. Trends of dolomitization (high-impedance) are still consistent with those of the upper zones.

Many previous studies stated that dolomite is extremely rare in zone 3B (Cantrell et. al., 2001). However, it largely consists of the low porosity, mud-supported micritic lithofacies. The zone was interpreted to have been deposited from intertidal to low supratidal environments. Therefore, high impedance values as anticipated are still prevalent over slice 8 and 9, which are cutting this zone. Lower values are encountered on the flank and the structural highs to the west (Figure 17 a/b). As in zone 3B, dolomite is extremely rare in zone 4 (Cantrell et. al., 2001). Nevertheless, high-impedance rocks are expected to be common since the zone is dominated by dense, low porosity, mud-supported micritic lithofacies. That what the last two slices (slice 10 and slice 11) (Figure 18 a/b) clearly show with slight decrease in impedance values in the upper part, which can be related to the largely developed porous grain-supported lithofacies interbedded with micritic lithofacies in this zone

As shown in the isochron map (Figure 19), a structural-low area in the middle of the southern most area shows somewhat high values in some impedance slices compared to the surrounding areas. This is only recorded in the relatively high-impedance zones. Therefore, this phenomenon is interpreted to be depositionally controlled, as carbonate rocks are very sensitive to even minor bathymetric changes caused by structurally related

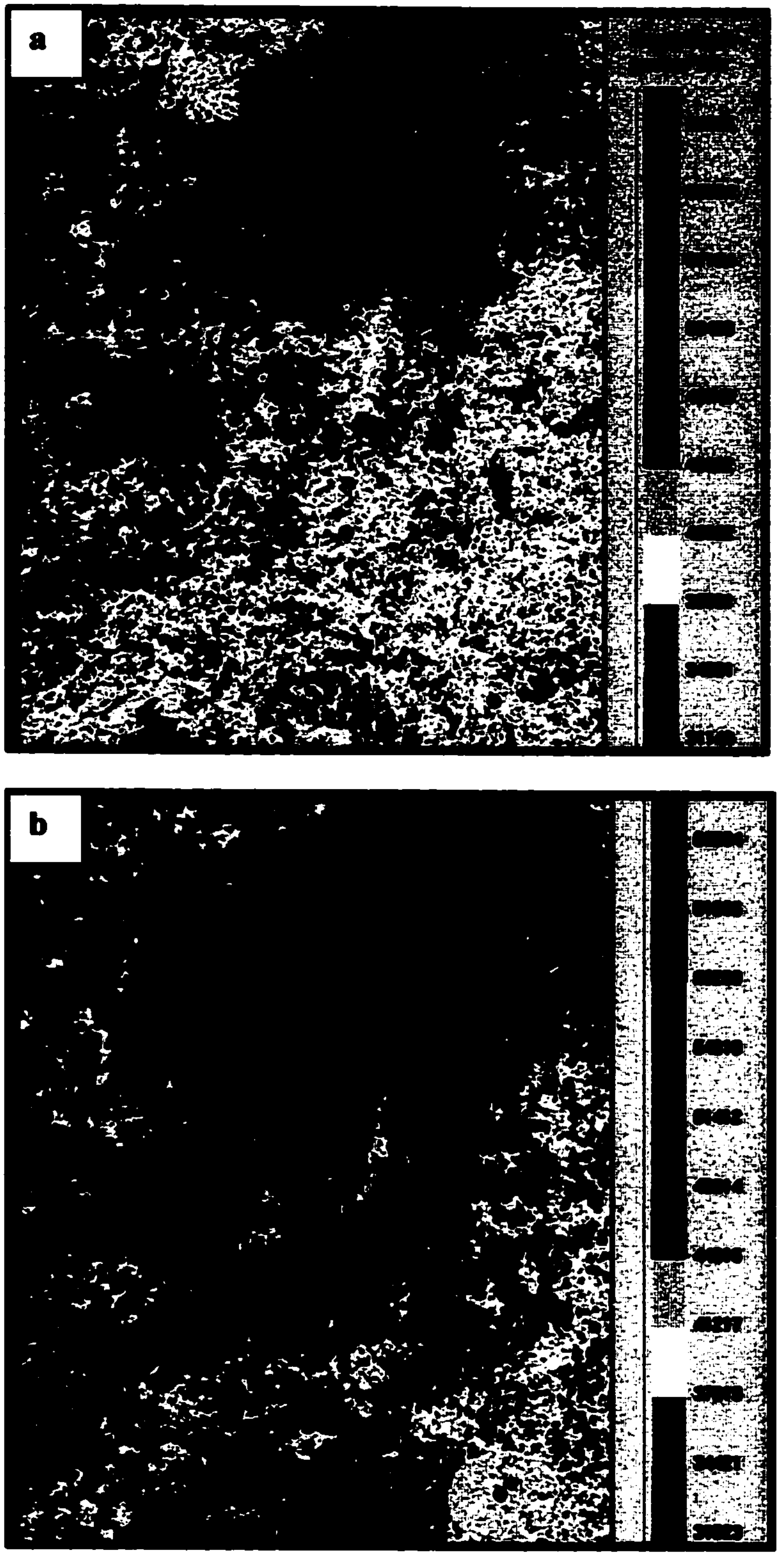

Figure 16: Slices passing through zone 3A: a) slice 6 at the middle part of the zone, b) slice 7 at the lower part of the zone 3A displays higher impedance values than the upper part of the zone due to the increase in mud content and dolomitization

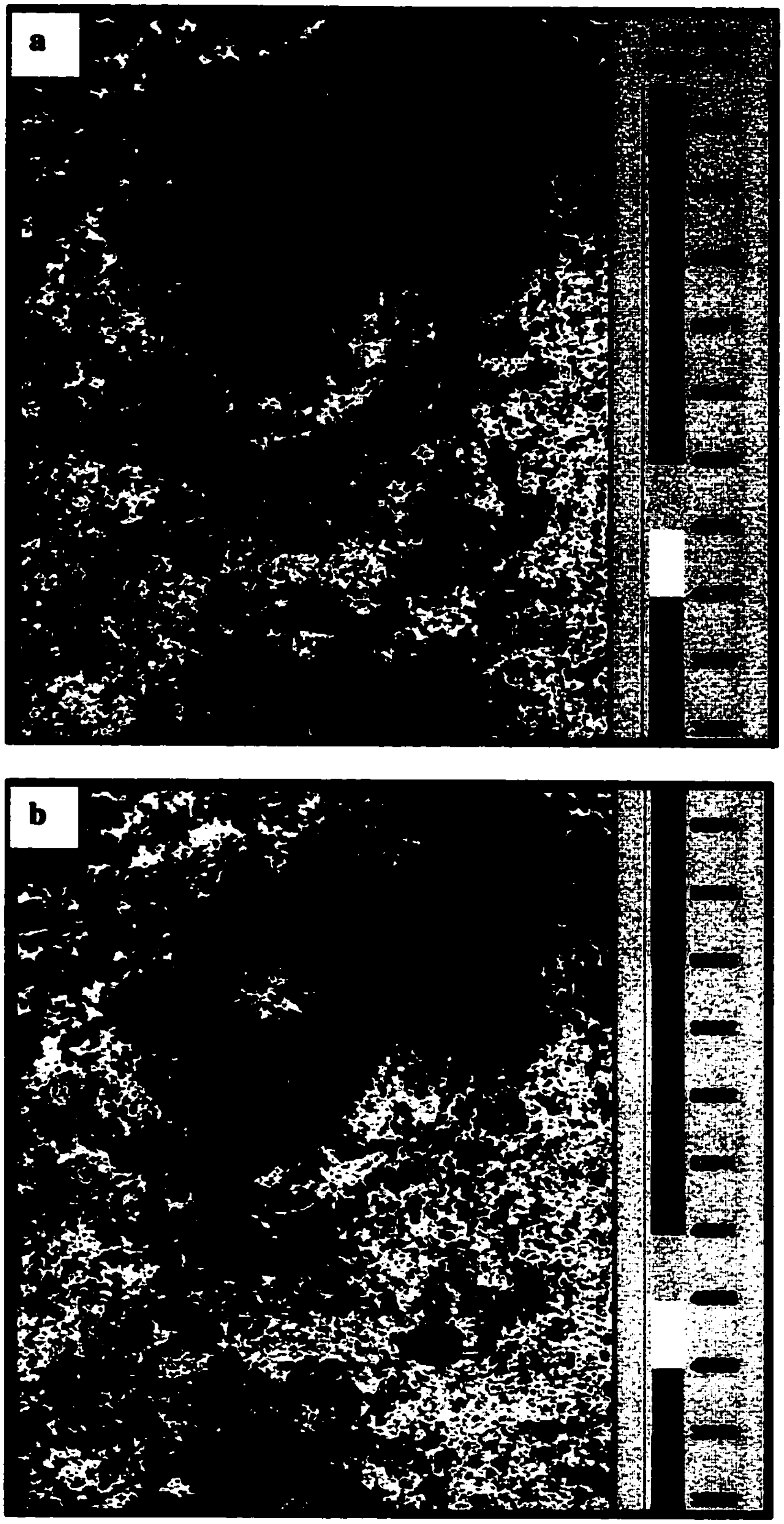

Figure 17: Slices passing through zone 3B: a) slice 8 at the upper part of the zone b) slice 9 at the lower part of the zone. High impedance values are prevalent in this zone since it largely consists of mud-supported micritic lithofacies

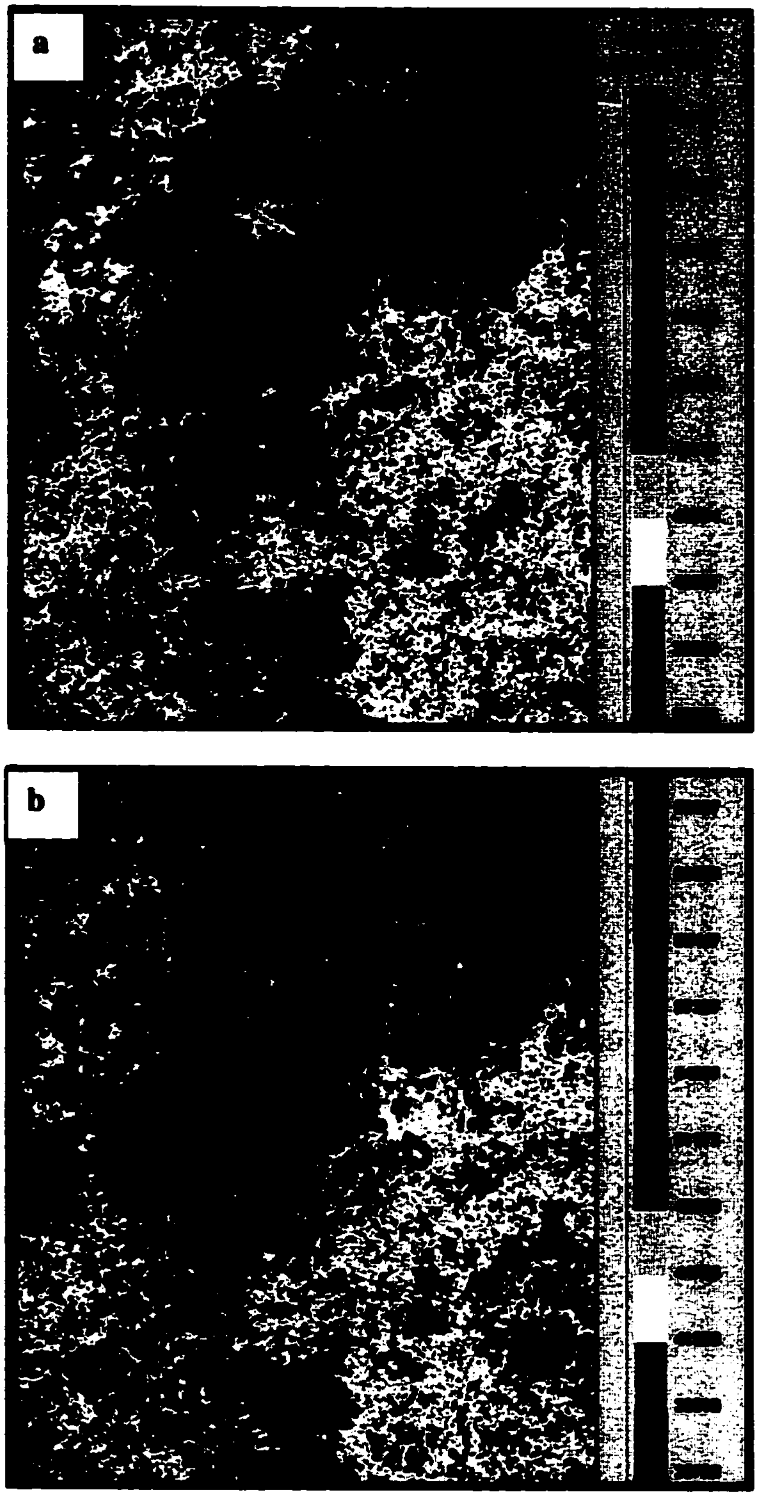

Figure 18: Slices passing through zone 4: a) slice 10 at the upper part of the zone, b) slice 11 at the lower part of the zone. The zone displays high-impedance values with slight decrease in impedance values in the upper part due to porous grain-supported lithofacies interbedded with micritic lithofacies

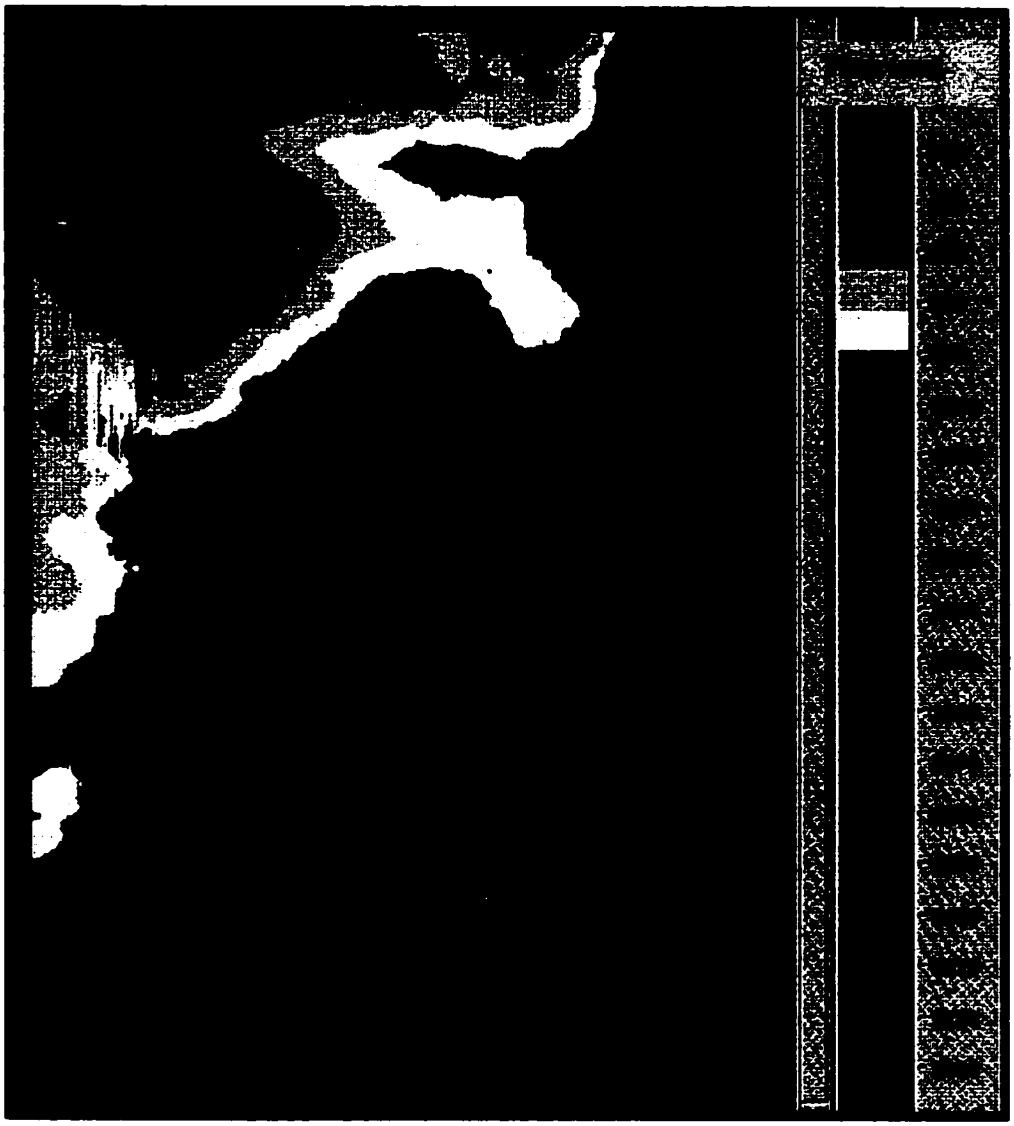

Figure 19: Isochron map of the top of Arab-D reservoir displaying the structural lows and highs expressed at the upper boundary of the reservoir

bathymetric relief. This effect becomes more obvious in the muddier carbonate zones, which have been deposited in a low-energy depositional environment. The southeastern corner of the survey shows a somewhat erratic rounded area with distinctive high and low impedance values. High values are encountered in zone 2B, which is the most dolomitized zone in the reservoir, whereas low values are recorded in all other zones. Hence, this feature is interpreted as a local intensively fractured area in which the most invaded zone by the dolomitizing solutions tends to be more affected by dolomitization responsible for degrading this area. Fractures have favorable effect on other zones in this area where it improves reservoir quality.

Cross-sections clearly manifest and support the previous information in the depth dimension. Dominance of high-impedance rocks in the lower zones of the reservoir in the central structural lows is quite obvious on the cross-sections of inlines passing through the southern area (Figure 20). It is also obvious that in this area, the quality of reservoir zone 2A and bottom of zone 2B degrades off-structure toward the eastern flank (Figure 21).

In general, high-impedance rocks in the most porous zones of 2A and 2B are most likely attributed to dolomitization whereas these impedances are attributed to muddier rocks residing in a gentle low structural relief extending along the central region. This smooth gentle low-relief area, which turns into relatively deeper structure to the south, is expected to be a beginning of a local small syncline extending to the south. Facies distribution was supposed to be controlled by a generalized structural trend from structural highs at the crest of the main anticline to the distal structural lows of the flank. Where more grain-supported facies present on the structural highs and the muddier rocks increase toward the flank. This generalized scheme suggested by many previous regional–scale studies (Cantrell, 2001) and (Daetwyler, 1987) is found invalid in this scale of study, since the influence of local structural lows and highs, is found to be crucial due to the sensitivity of carbonates deposition to minor bathymetric changes.

Much accurate and meaningful lithological description and interpretation of the model would have been possible, if core data had been available. A new description based on core analysis will add a great value to further lithological investigation and could thereby help explain detailed variation in the interwell region.

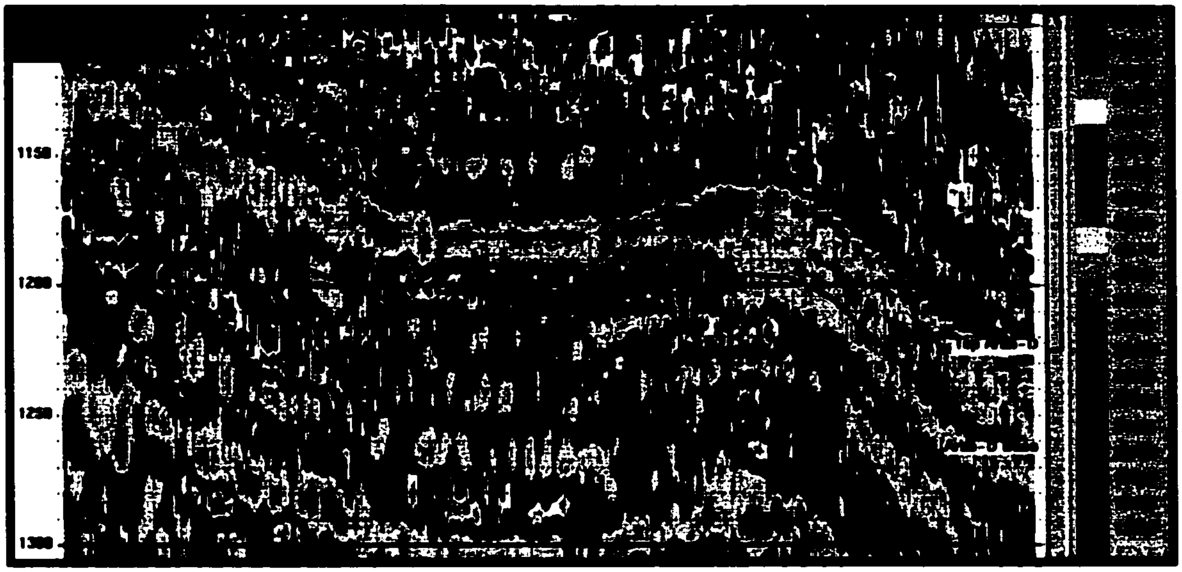

Figure 20: E-W cross section showing the different zones of the reservoir and the dominance of high-impedance rocks in its lower zones

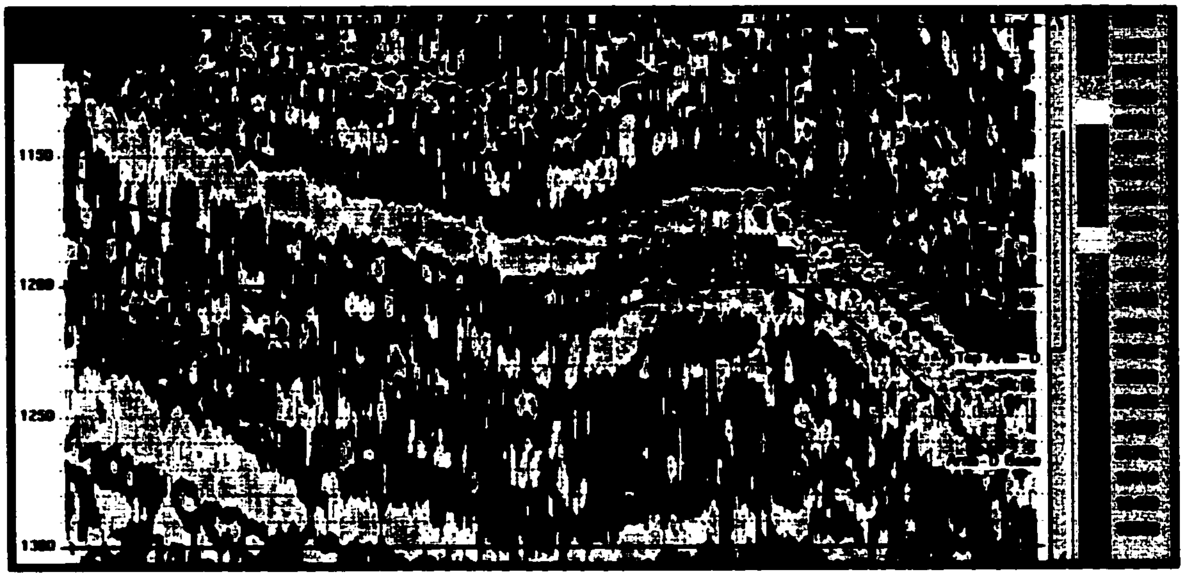

Figure 21: E-W cross section showing the degradation of the quality of reservoir zone 2A and bottom of zone 2B off-structure toward the eastern flank

5.2. SEISMIC FACIES ANALYSIS

Seismic facies maps generated through this study using neural network technique has proven to be very efficient in manifesting facies distribution. The classification technique used is entirely based on the signal variability, which genuinely leverages the underlying rock properties. Therefore, Seismic facies map can greatly reflect the general trends of facies distribution as well as the physical factor that controls this distribution.

As stated earlier, a less quality facies map was firstly generated from a direct classification of the seismic traces. Incorporation of seismic attribute and azimuth-dip maps has notably participated in improving the quality of the facies map. Seismic attributes are known to give some qualitative information of both the geometry and the physical parameters of the subsurface. Dip-azimuth maps (Figure 22) are merely structural maps that account for the major structures found within the signal zone and thus better guide the classification of the seismic signal.

A final high-resolution facies map of the Arab-D interval containing fifteen types of facies displayed in different colors for better visualization (Figure 23). This map showed a clear facial zonation. This distribution is quite regular suggesting some depositional controls. As seen from the map, facies types are changing gradually in a systematic manner from the southeast to northwest, i.e. from distal flanks areas to the axis of the main anticline of Uthmaniyah area. This also suggests a northeastern trend for the paleoshore line at this area. However, it shows a northwestern trend on regional scale (KFUPM, 2000). A central elongated area represents an anomaly to the general behavior of the facies distribution. This area is extending from south to north and increasingly narrowing to the north.

Figure 22: Azimuth map showing the major structures of the top of Arab-D reservoir

Figure 23: Multi-attribute facies map showing fifteen different types of facies in different colors. See the gradual facies change from the structural lows at the flank area to the southeast to the structural high at the axis of the major anticline to the northwest

Referring to the structural time map of the top of the Arab-D reservoir, it is quite obvious that this facies distribution is mainly controlled by the structural geology of area. This finding strongly confirms the previous results obtained form the seismic inversion analysis. Since it is found that the spatial distribution of rock types in most of the reservoir zones is structurally controlled. Lateral facies change follows the famous depositional trend in which structural highs are dominated by more porous grain-supported rocks grading to muddier carbonate rocks on the structural lows. The suspected local syncline interrupts this trend giving different facies that might characterize that level of depth. This is consistent with the fact that deposition of carbonate rocks is very sensitive to minor bathymetric changes caused by even few feet of structural relief. It's worth recalling that the prominent areas of high impedance values in zones 2A and 2B are due to dolomitization.

Advanced petrophysical investigations were performed to study the impact of the different petrophysical properties on the signal variability or the lithological distribution within each reservoir zone. This method depends on an interactive parameter modification and consequent modeling of the seismic response to test geological hypotheses and model the seismic response at well locations. Simply the model was perturbed by editing thickness, density and porosity within a specific zone and recording the response of the seismic signal to these parameters. This allowed identification of the most petrophysical controlling factors that produce major changes in the seismic signal and thereby affect facies classifications. The most dominant facies type (Figure 24) was selected to execute these tests at well locations and build a general idea about the petrophysical control. This helped define the factors that govern lithological variability within each zone.

Editing thickness and density values at zone 1 caused a substantial change in the shape of the seismic trace, whereas changing porosity values has almost no effect on the seismic signal. When density was decreased form 2.847 to 2.5 gm/cc, the seismic response was significant (Figure 25). Also a slight change in thickness from 3.8 to 4m resulted in a considerable change in the seismic signal (Figure 26). In contrast, porosity was largely modified from zero to 15%, although the modification of the trace shape was negligible (Figure 27). This implies the insignificance of porosity to facies distribution due to the presence of low-porosity dolomites and anhydrites. Thus only difference in rock density and thickness can affect facial zonation.

Modifying thickness of zone 2A also caused an obvious modification in the seismic signal (Figure 28). Density is still influential as well as the porosity, which started to exert greater influence in this zone. Changing thickness form 11 to 15 m produced a clear change on signal shape. Also, the signal was largely deformed when density was increased from 2.37 to 2.8 gm/cc (Figure 29). And slight change in porosity from 22.2% to 25 % caused great change in signal shape (Figure 30). This suggests that all these parameters play an important role in the distribution of rock types within this zone.

As in zone 2A, all parameters are found to be important to facies distribution in zone 2B. This was tested by changing thickness from 22.3 to 30m (Figure 31), density from 2.4 to 2.8 gm/cc (Figure 32) and porosity from 19.7% to 11% (Figure 33). Also, all parameters were crucial to facies distribution in zone 3A. This was tested by changing thickness from 17.4 to 25m (Figure 34), density from 2.5 to 2.0 gm/cc (Figure 35) and porosity from 12% to 19% (Figure 36). In zone 3B, porosity and density were quite important; although porosity appeared to be less important than in the three previous

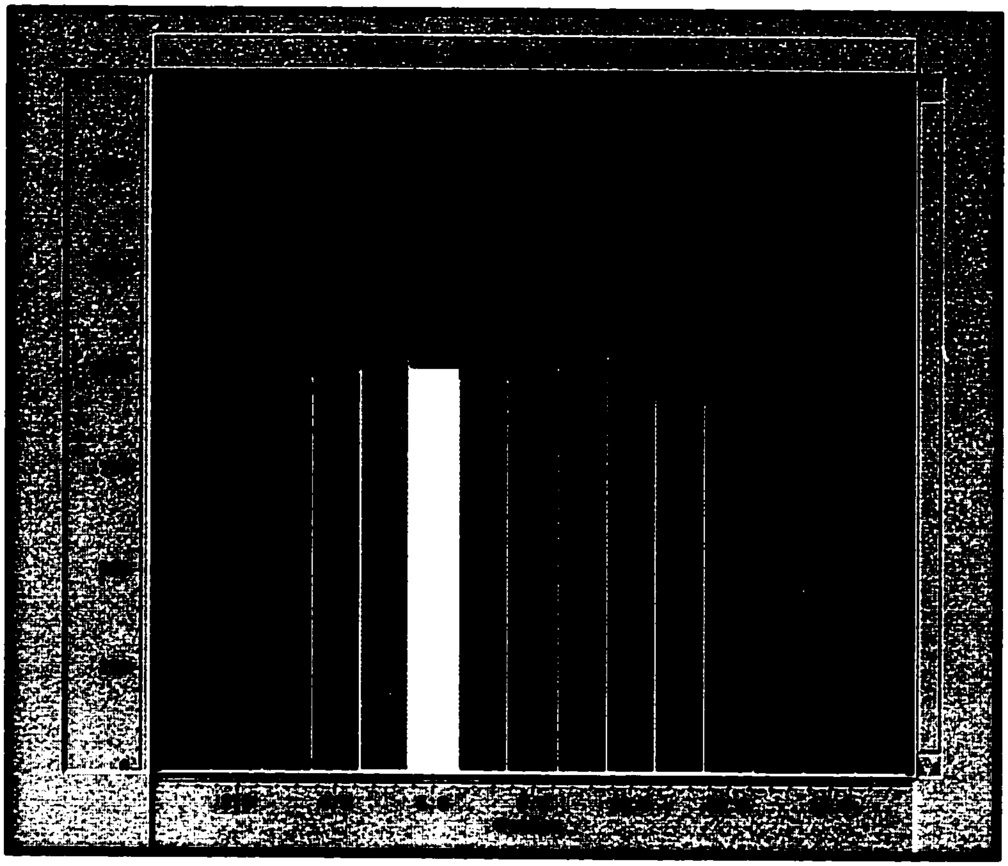

Figure 24: Histogram showing different types of seismic facies appeared in the multi-attribute facies map with the dominant facies shown in dark brown color

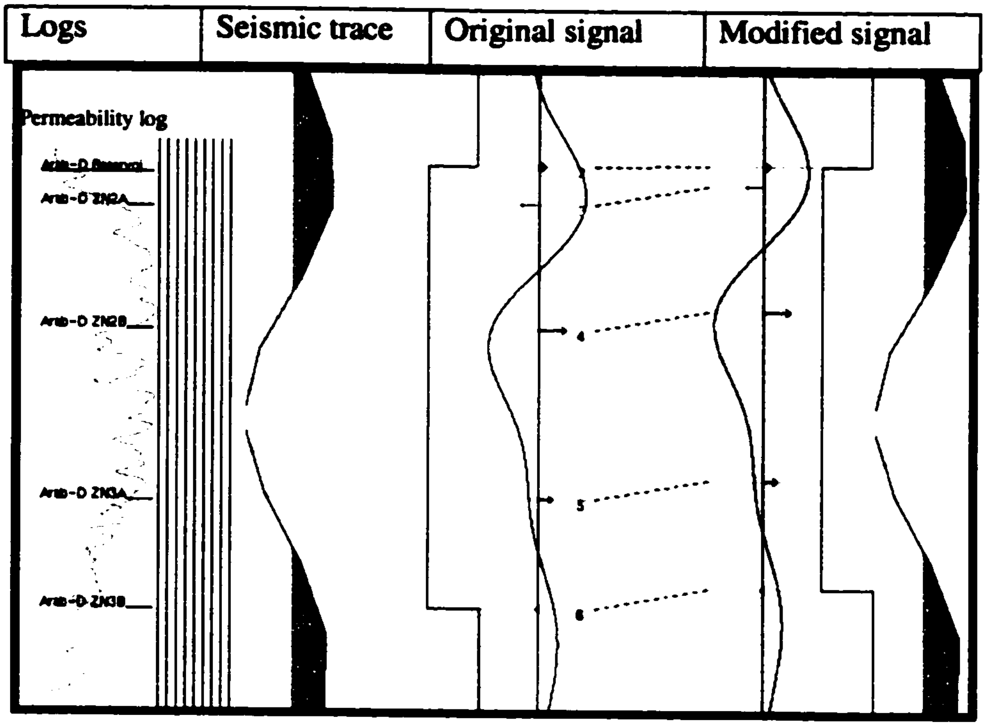

Figure 25: Effect of thickness on signal variability (zone1)

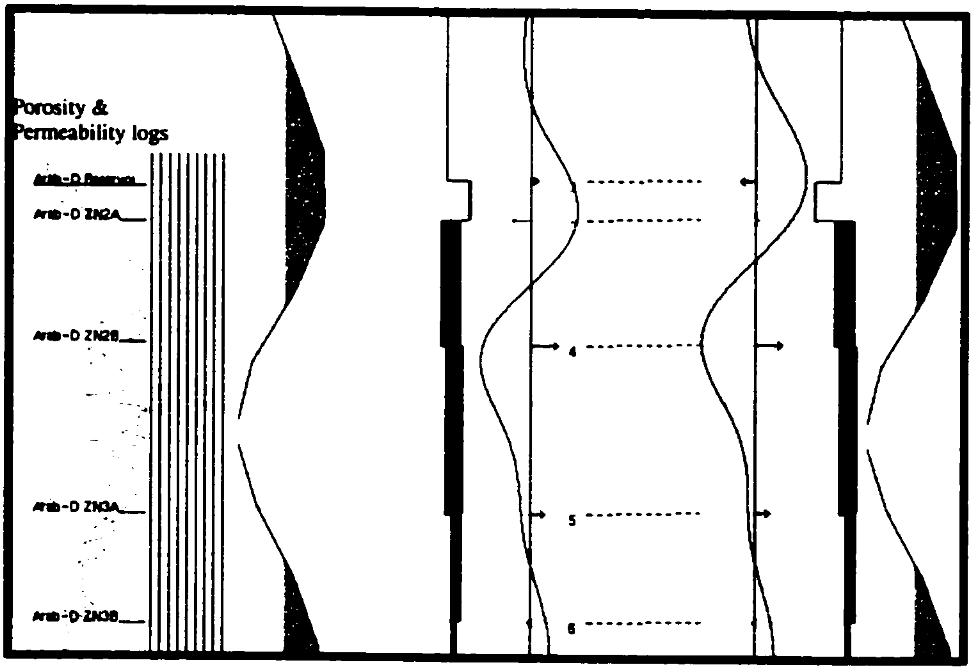

Figure 26: Effect of density on signal variability (zone1)

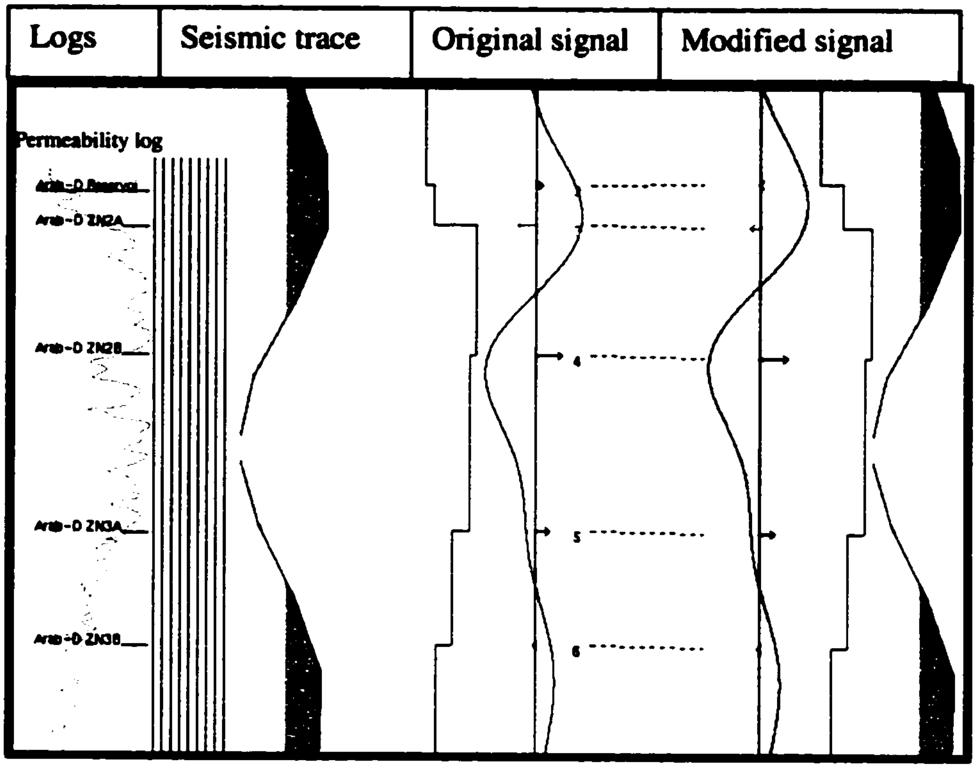

Figure 27: Effect of porosity on seismic signal (zone1)

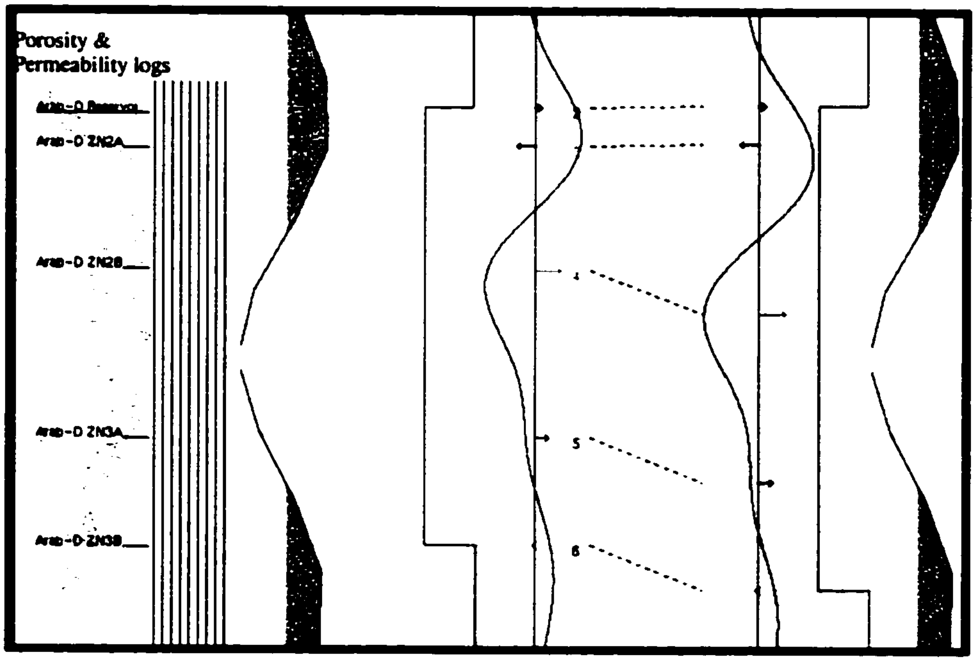

Figure 28: Effect of thickness on seismic signal (zone2A)

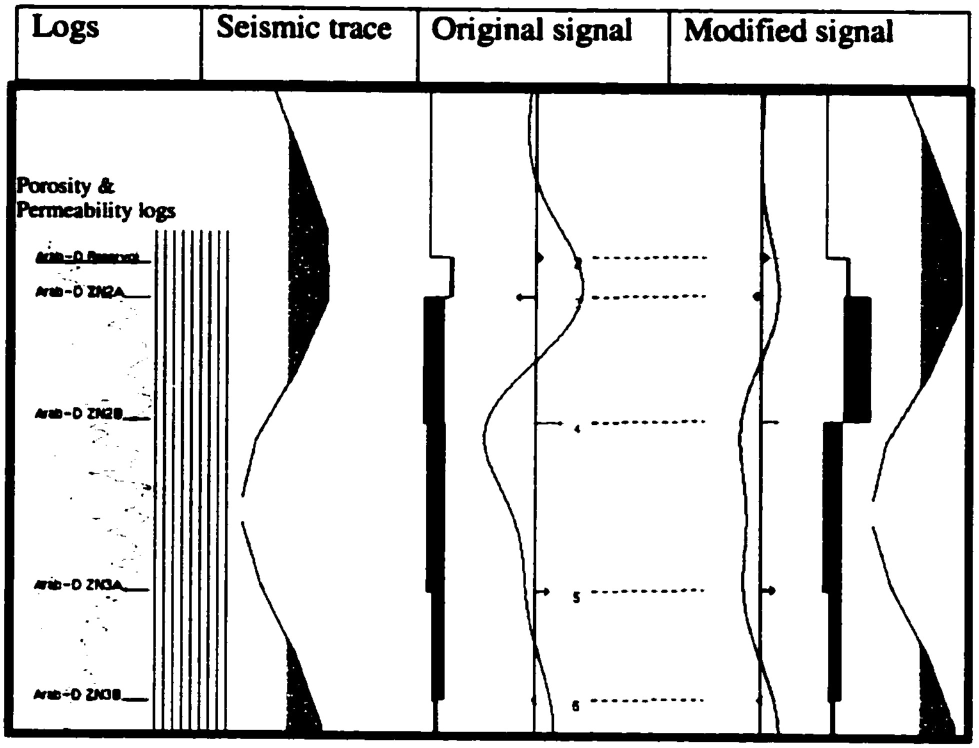

Figure 29: Effect of density on the signal variability (zone 2A)

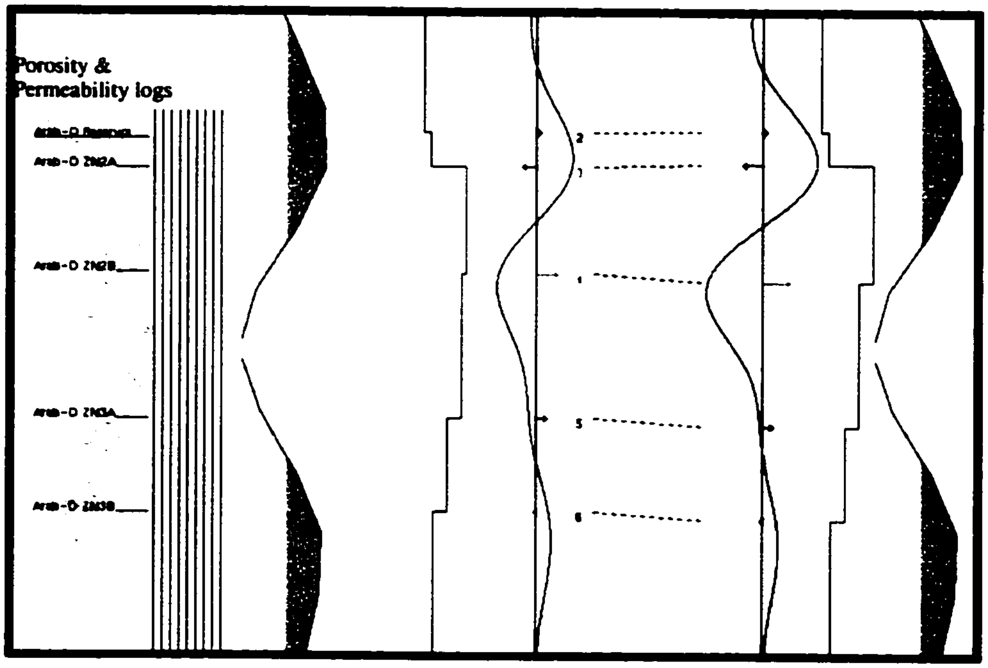

Figure 30: Effect of porosity on the seismic signal (zone 2A)

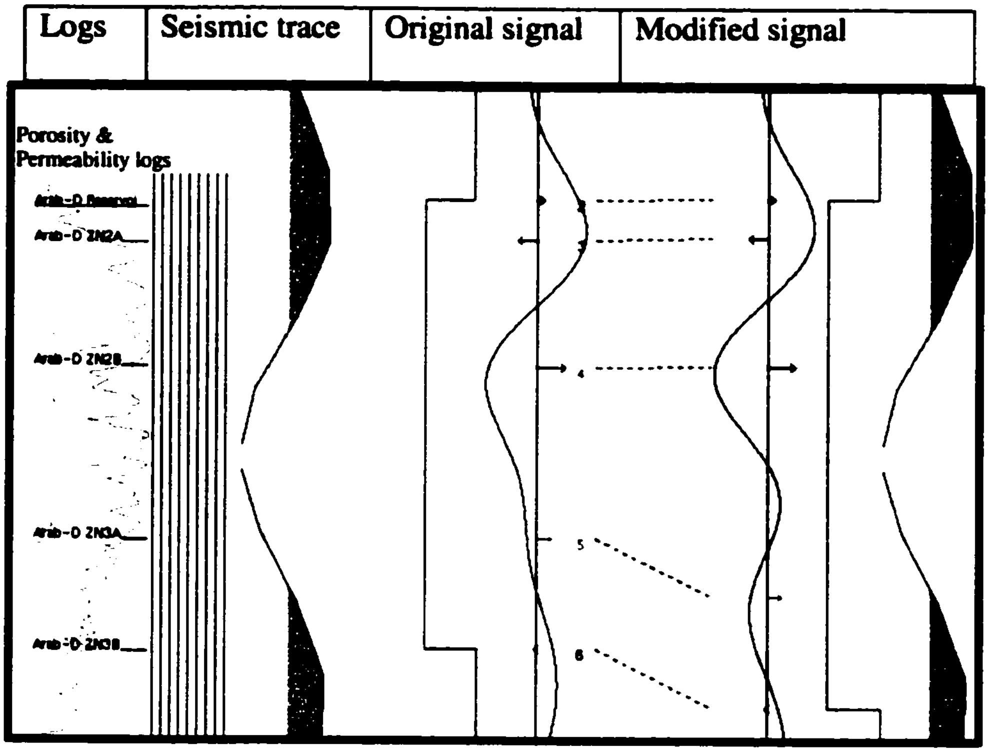

Figure 31: Effect of thickness on seismic signal (zone 2B)

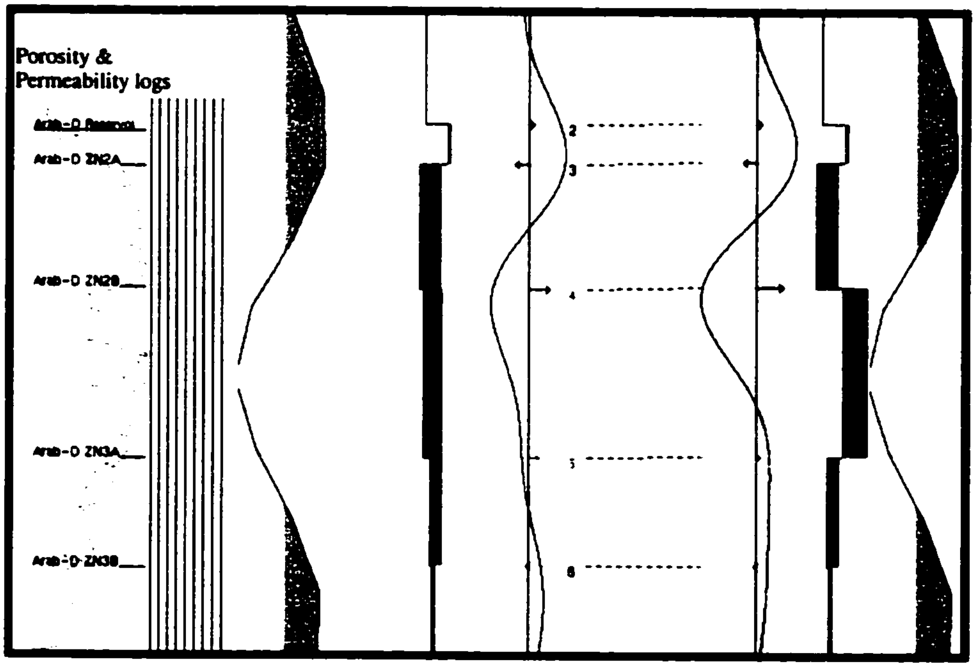

Figure 32: Effect of density of the seismic signal (zone 2B)

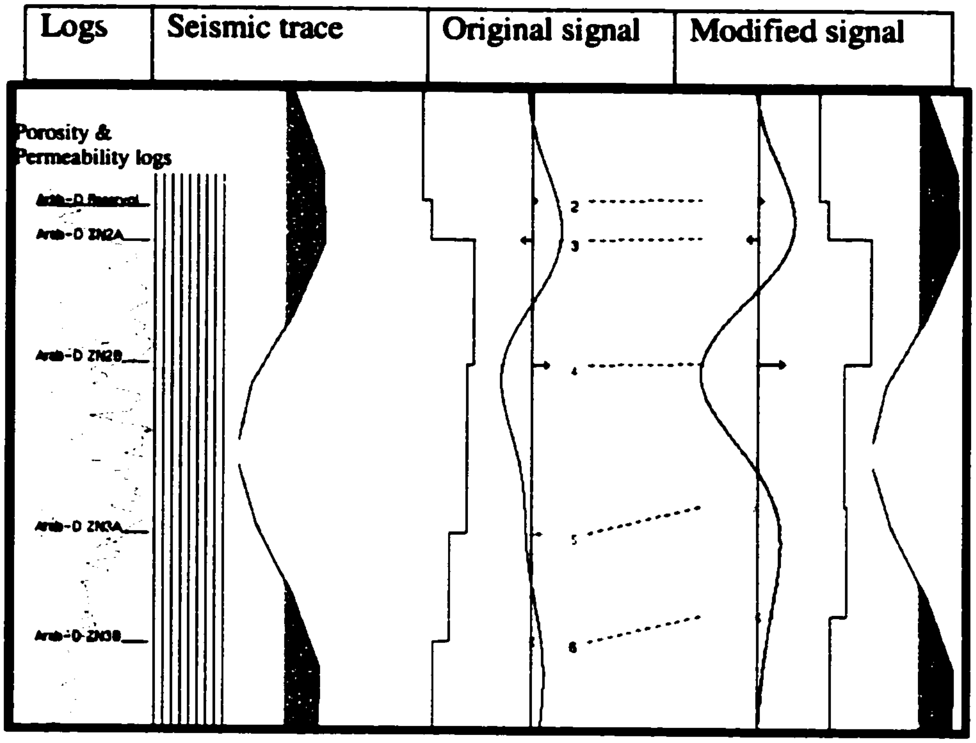

Figure 33: Effect of porosity on the seismic signal (zone 2B)

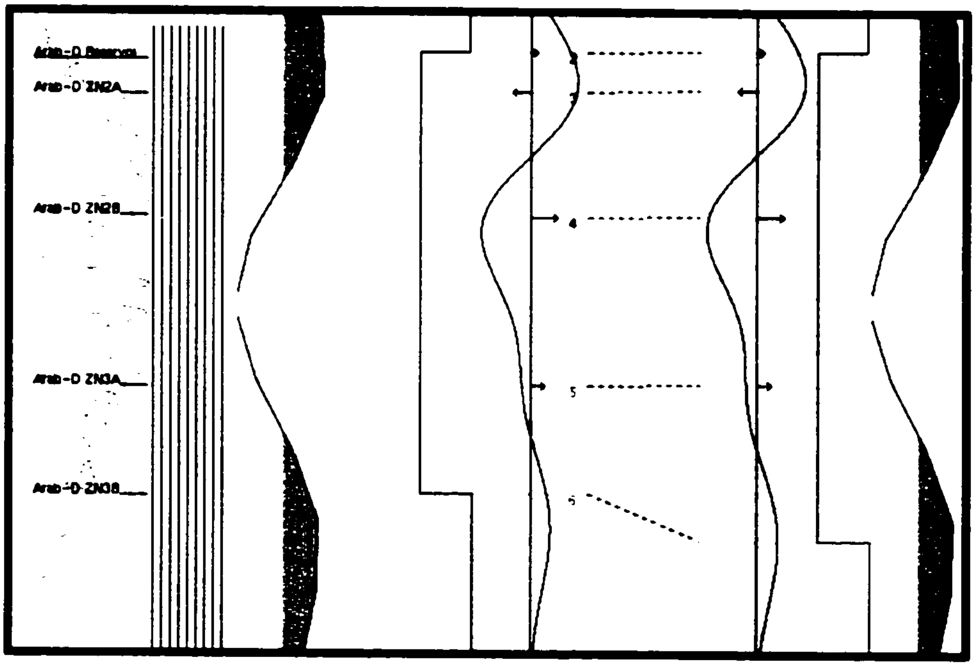

Figure 34: Effect of thickness on the seismic signal (zone 3A)

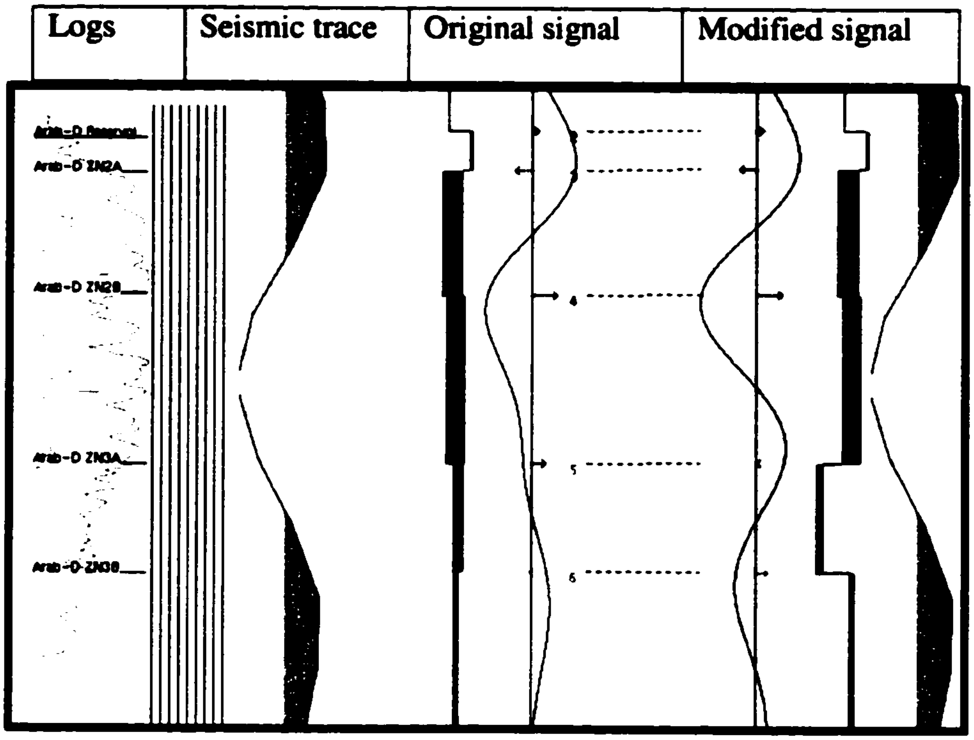

Figure 35: Effect of density on the seismic signal (zone 3A)

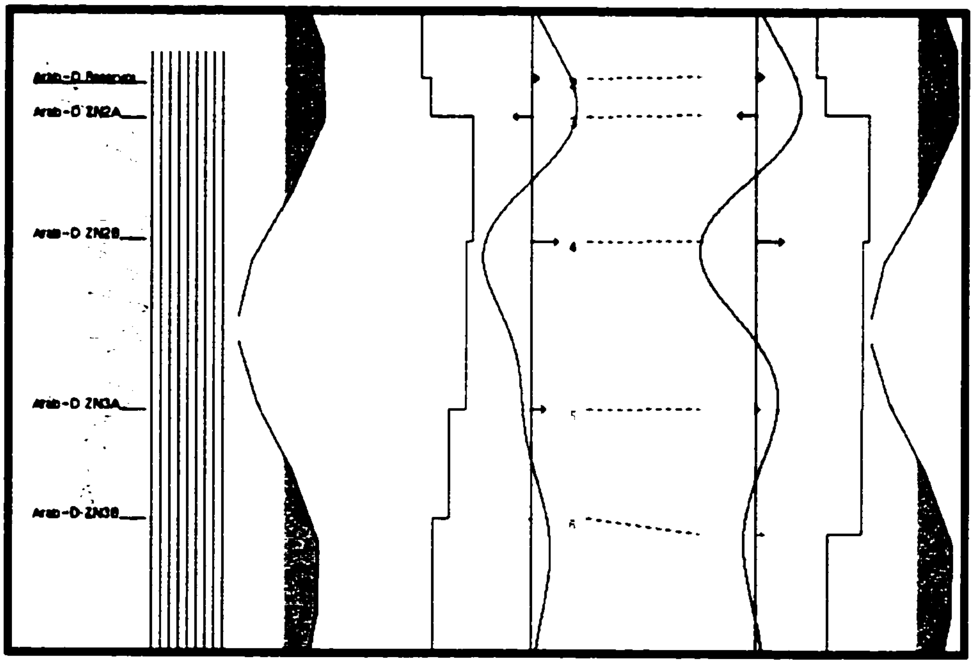

Figure 36: Effect of porosity on the seismic signal (zone 3A)

zones. These tests were performed by changing density from 2.59 to 2.8 gm/cc (Figure 37) and porosity from 4.9% to 9% (Figure 38). This is most likely attributed to the considerable increase in the mud content and the substantial decrease in porosity in this zone.

Generally, density and porosity were found to be the main controlling factors to facies distribution. This was quite expected since the differences between rocks reflect the structural geology of the area. Structurally controlled lithological distribution is a function of mud content and grain size, which in turn determine rock density and porosity.

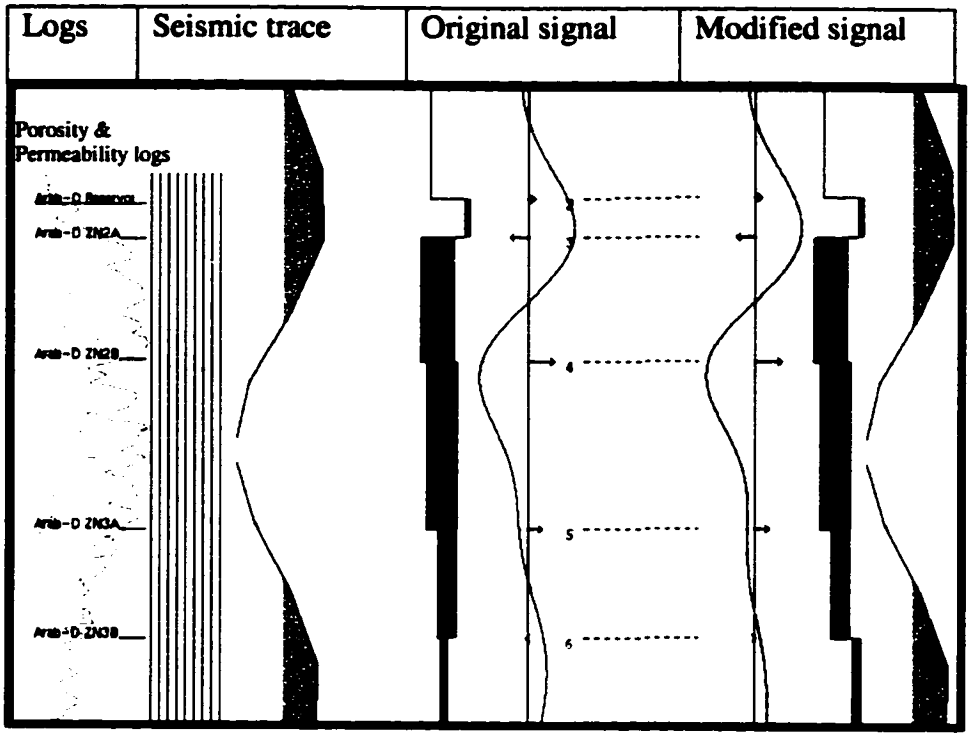

Figure 37: Effect of density on the seismic signal (zone 3B)

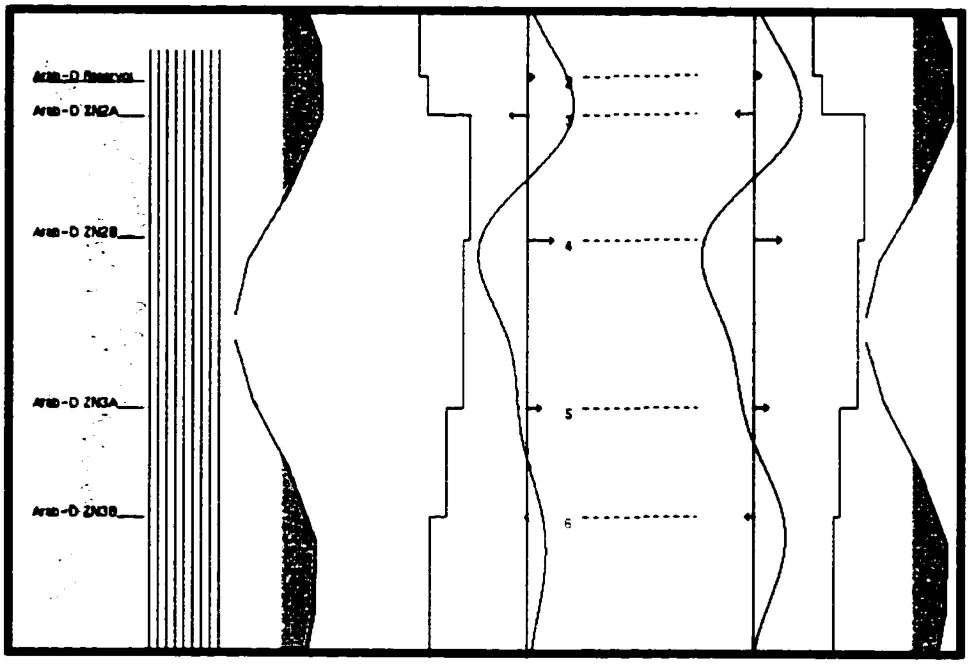

Figure 38: Effect of porosity on the seismic signal (zone 3B)

5.3. GEOSTATISTICAL ANALYSIS

5.3.1. BIVARIATE ANALYSIS:

Porosity values from eleven wells within the study area were used as a primary data to model porosity. Some of the seismic impedance slices, generated in the inversion analysis part, were again used as a secondary data to generate porosity slices passing through distinctive zones within the reservoir interval. The basic incentive, for using impedances in reservoir characterization, stems from observed excellent correlation between porosity and seismic impedance. Impedances have the ability to indicate anomalous porosity zones between wells, whereas little predictive strength is gained using other parameters. Also, using impedances has proven to be excellent in case of modeling porosity using few wells. Vegbaek et. al. (1996) noticed that the seismic impedances are particularly useful in areas with very little well data. Only eleven average interval porosities from eleven wells were used as primary data for modeling. Occasionally, porosity values at some wells showed bad correlation with impedance and hence they were excluded from the analysis to maintain high correlation obtained from other wells. This problem is most likely caused by inaccuracy resulted from noisy data present around these wells since they gave the lowest seismic-well correlation in the inversion process.

Impedance-porosity relationship was tested by cross-plotting seismic impedance against porosity for each slice. Impedances show good correlation with porosity ranging from – 0.6 to – 0.8 (Figure 39). This relationship was then utilized to initially predict porosity by applying linear regression to the input data. As seen form the regression maps, results obtained are largely inaccurate (Figure 40). It was noted that predicted values at

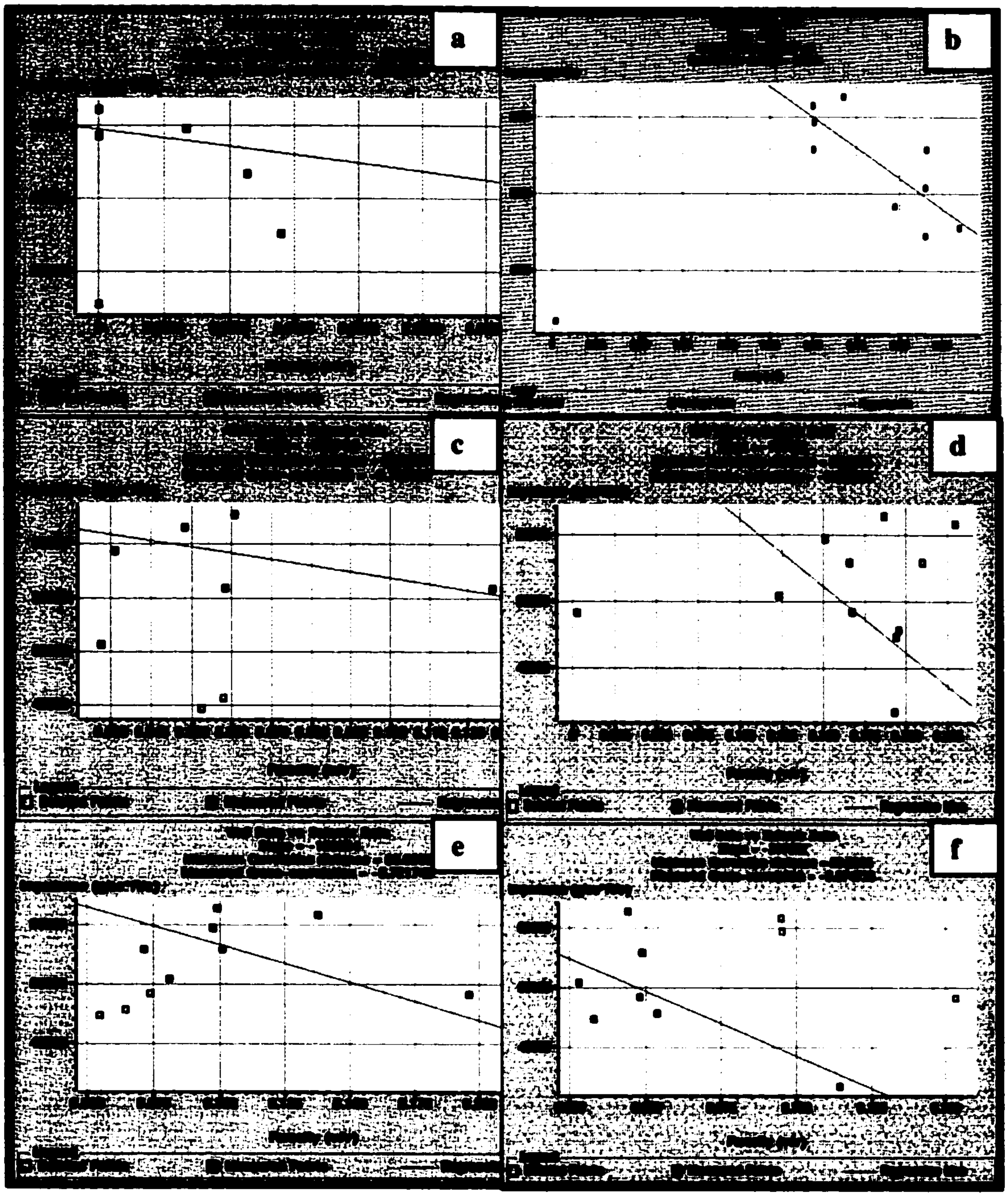

Figure 39: Cross plots between impedance and porosity for slices: a) slice 1(zone1), b) slice 2 (zone 2A), c) slice 3 (upper part of zone 2B), d) slice 5 (lower part of zone 2B, e) slice 7 (zone 3A) and e) slice 9 (zone 3B).

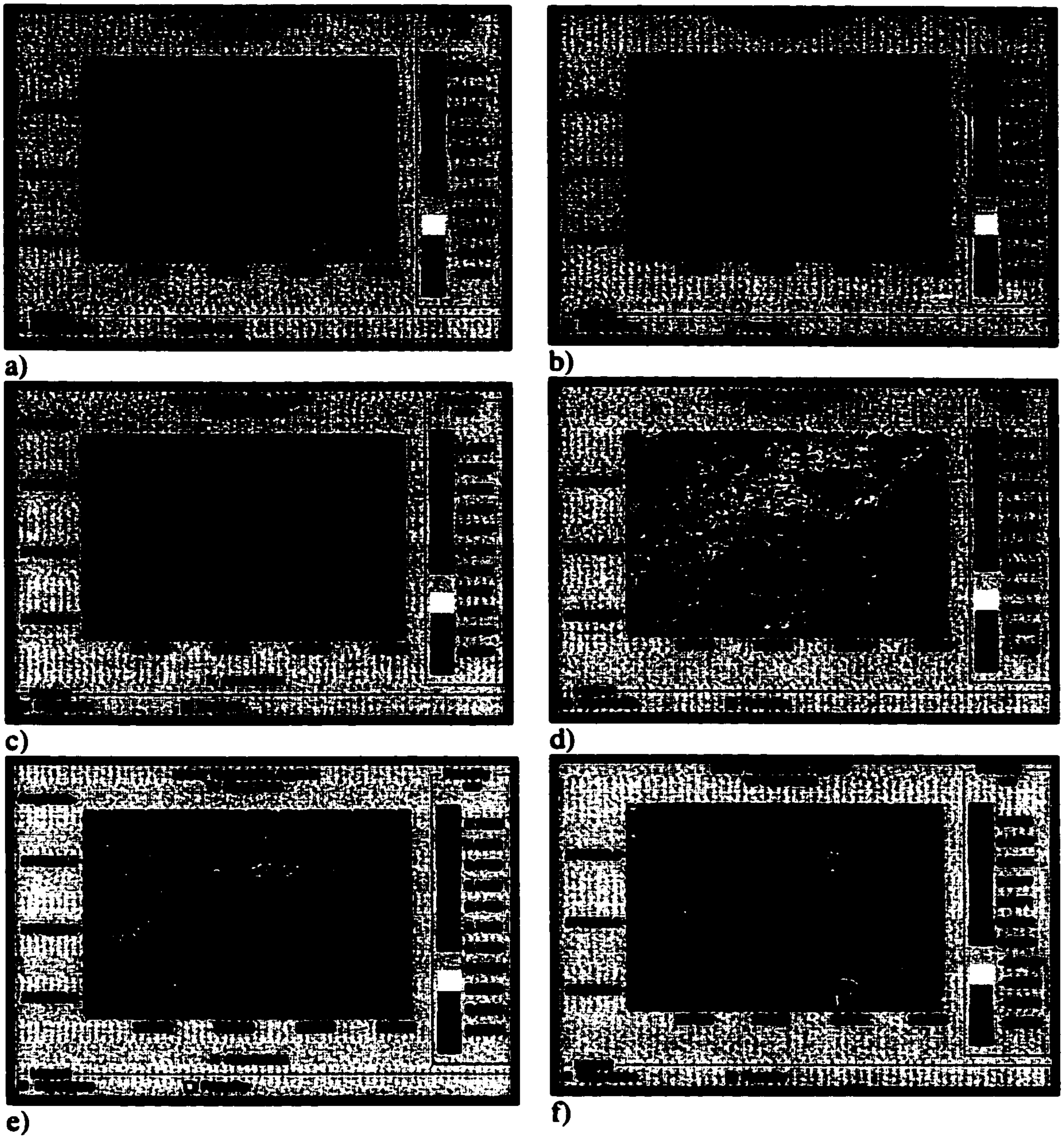

Figure 40: Linear regression applied to input data, a) slice 1 (zone 1), b) slice 2 (zone 2A), c) slice 3 (upper part of zone 2B), d) slice 5 (lower part of zone 2B), e) slice 7 (zone 3A), f) slice 9 (zone 3B). Predicted values at many well locations in all of the slices are quite different from the real values of logs

many well locations are quite different from the real values of logs. This necessitates introduction of the more robust techniques discussed in the following sections.

5.3.2. SPATIAL ANALYSIS:

Generally, the experimental directional variograms would reveal major changes in the sill or the range as the direction changes. The rate at which the variogram rises toward the sill is a function of continuity of the property under study. When this rate changes with direction while the sill remains relatively constant, then this phenomenon is called geometric anisotropy. Once the axis of geometrical anisotropy has been identified, the theoretical model chosen needs to be adjusted so that it describes how the experimental variogram changes with distance and direction.

Omnidirectional variograms of the well data were modeled for each slice (Figure 41). Porosity values at well locations were calculated by averaging porosity values within five feet below impedance slices. The nugget of the spherical model of all these variograms were found to be zero, therefore honoring exactly well data was guaranteed. The ranges of these variograms are ranging from 2000 to 3000. Upper zones have greater ranges than the lower zones. This due to the larger structures encountered in upper zones. In contrast, sill values showed a considerable variation. Sill value of the variogram of zone1 is very small. The variograms of zones 2A and 2B showed higher values of sill, although it appeared to be relatively lower at the bottom of zone 2B. Sill values started again to be very low at zones 3A and 3B. High sill values indicate the randomness of the distribution of the porosity values, whereas low sill values indicate that the porosity values are correlated.

The rate at which the variogram rises toward the sill is a function of continuity, thus this variation can be related to continuity of porosity at each slice. Consequently, continuity in zone1 is considered to be higher than other zones. In contrast, zones 2A and 2B are interpreted to have lower continuity, which is consistent with the geological nature of these zones (see the previous section). Again, the variograms of zones 3A and 3B gave lower values indicating higher continuity. However, continuity in zone 3A is a bit higher than that of zone 3B. Cross variograms between the two data sets were also constructed to model the spatial variability of the combination of the two data sets (Figure 42). These cross variograms are deemed important since they are a major prerequisite to cokriging and conditional simulation as explained earlier.

Directional variograms of all zones (slices) were modeled to investigate the spatial variability of impedances in different directions. Four variograms in north, east, northeast, and northwest directions were established for each slice. All these variograms were generally characterized with almost constant ranges, varying sill values and zero nuggets. Again the rate of change of variograms near origin was used as a measure of continuity to reveal the underlying geology. Slices of zone1 and zone 2B displayed the highest continuity among other slices reflecting the randomness of porosity distribution in these zones, which also showed smaller structure. This is most probably attributed to the dolomitization effect. The low continuity of impedances in rest of slices is interpreted to be resulting from the homogeneity characterizing these zones relative to other zones (Figure 43). Variogram maps for all slices were generated to better manifest the directional continuity of impedances (Figure 44). Generally these maps showed small variability of impedances in the north direction. Only zone1 showed a relatively higher variability in the northeast direction.

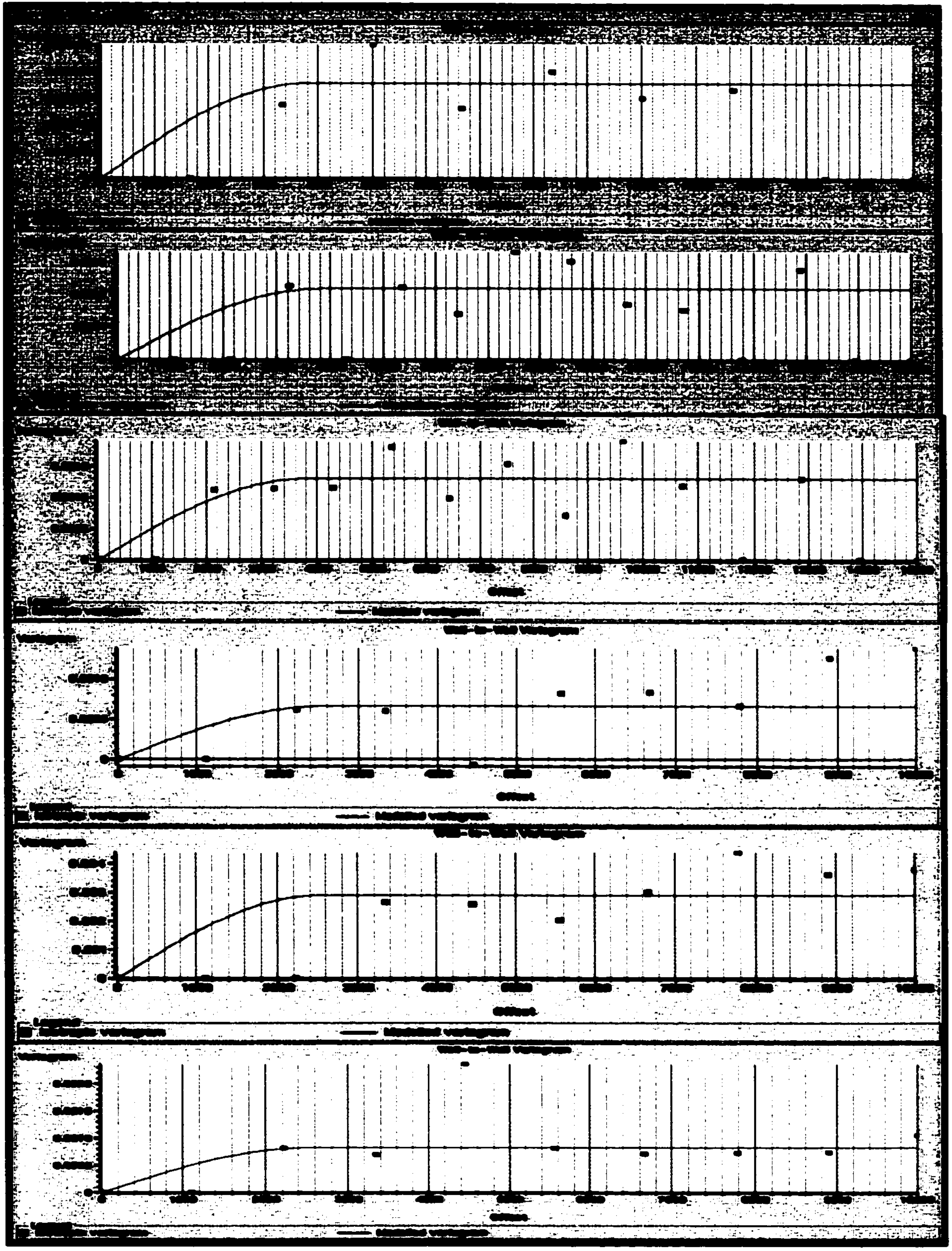

Figure 41: Omnidirectional variograms for porosity of slices from top to bottom: zone1, zone 2A, upper zone 2B, bottom zone 2B, zone 3A and zone 3B.

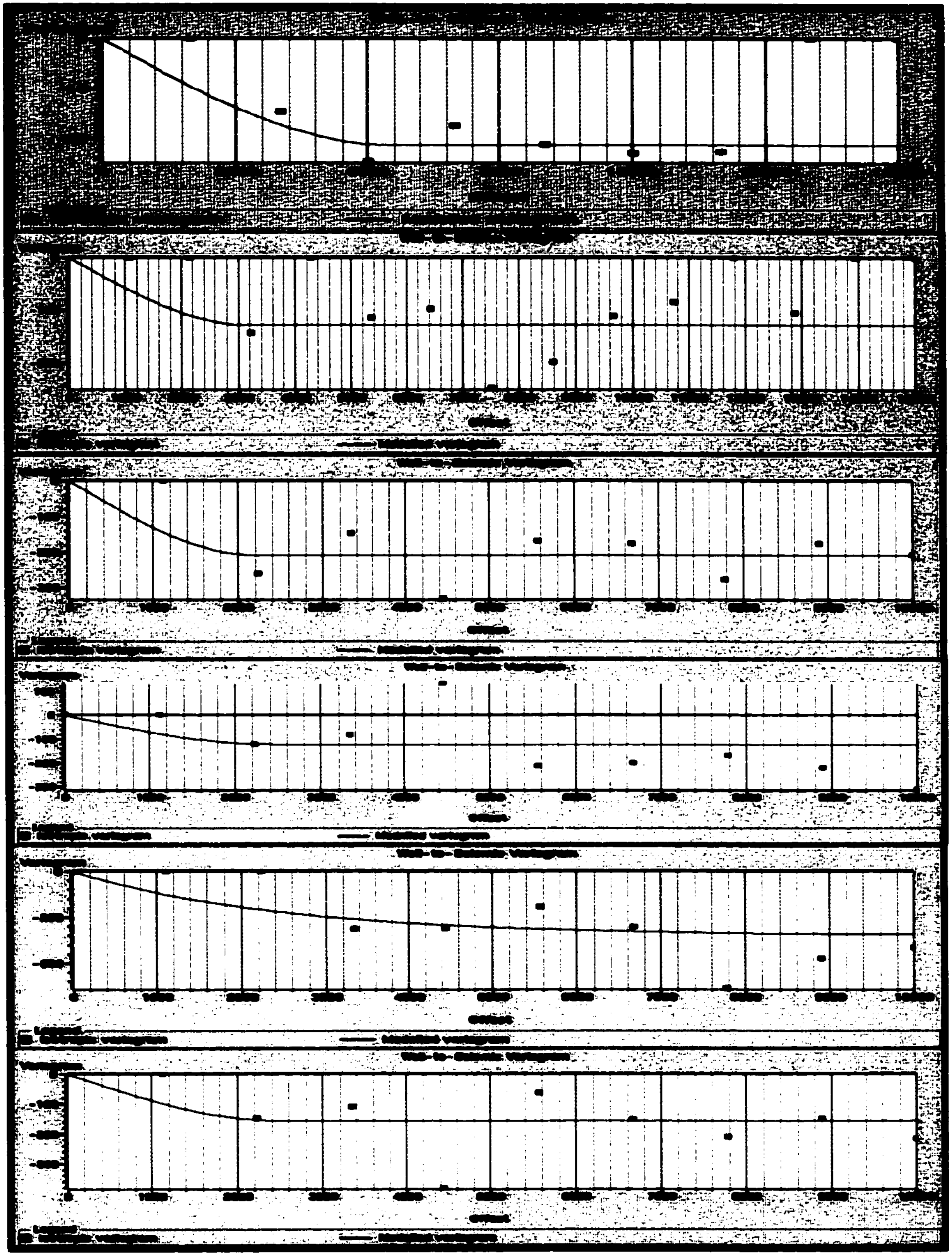

Figure 42: Well-seismic cross variograms for slices from top to bottom: zone1, zone 2A, upper zone 2B, lower zone 2B, zone 3A and zone 3B.

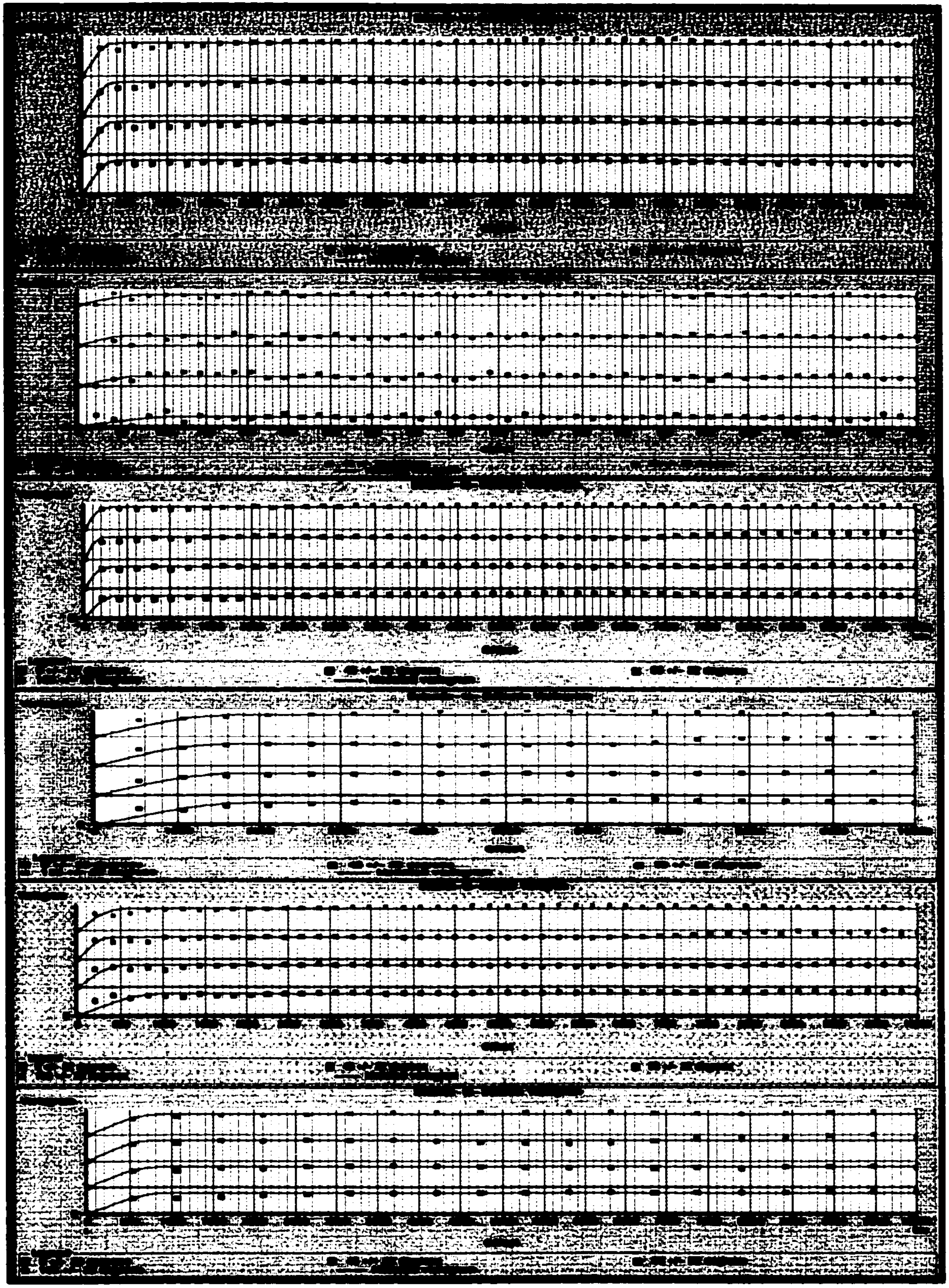

Figure 43: Directional variograms of impedances from top to bottom: zone1, zone 2A, upper zone 2B, lower zone 2B, zone 3A and zone 3B.

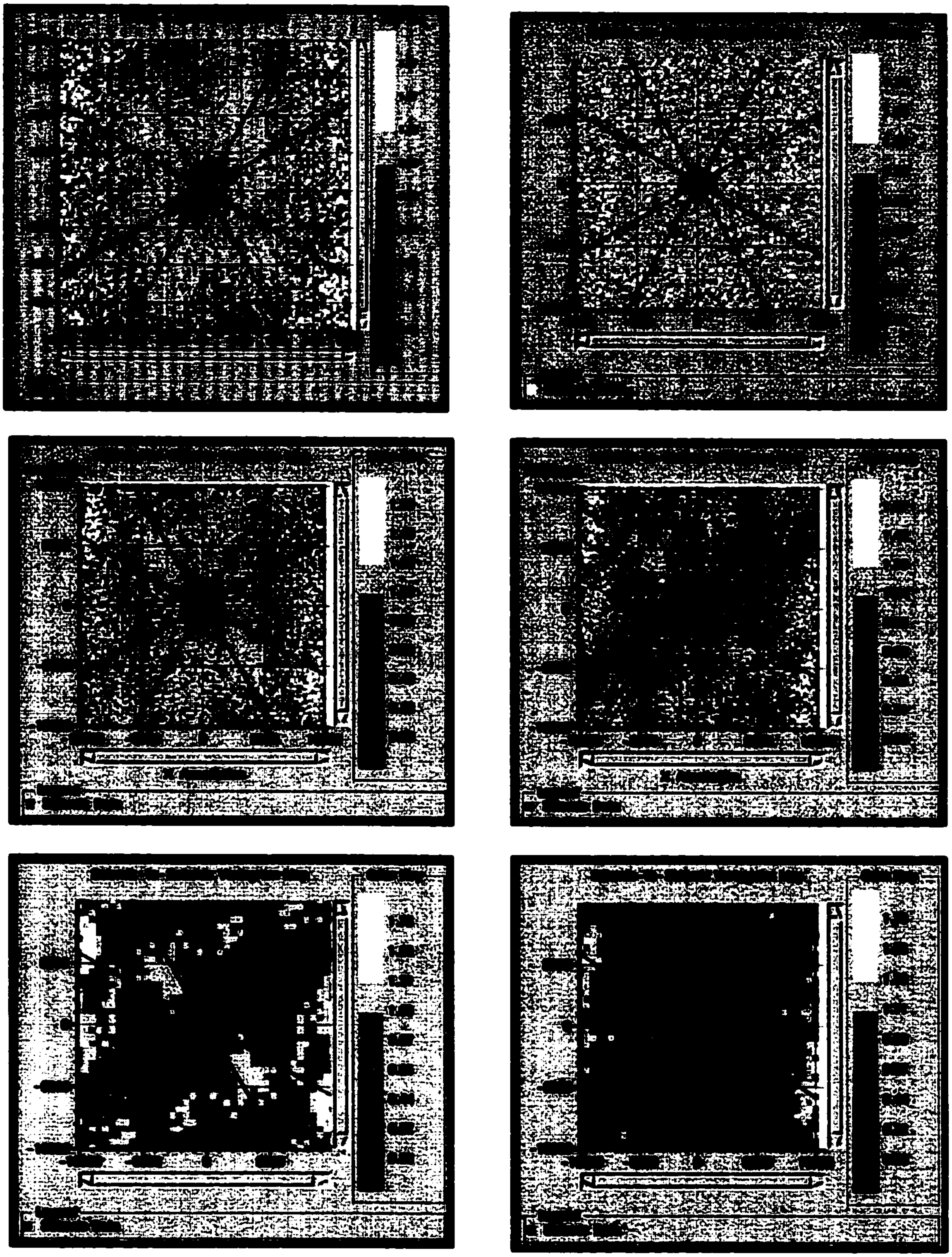

Figure 44: Variogram maps of impedances from top to bottom: zone1, zone 2A, upper zone 2B, lower zone 2B, zone 3A and zone 3B. Only zone1 showed a relatively higher variability in the northeast direction.

5.3.3. KRIGING:

2-D porosity maps were first generated using the ordinary kriging algorithm where only well average porosity values at the level of the given slices were used in the analysis. Given that porosity values previously excluded from analysis due to correlation problems were not incorporated in the kriging maps to be in consistency with other results and to evaluate the actual efficiency and contribution of the different methods to mapping variability. Six to nine porosity values were commonly used to generate porosity maps for slices passing through the different zones.

As seen from figure (Figure 45), kriging maps could not properly reveal porosity variation within different zones. Instead, very spatially smoothed simplistic porosity maps for these zones were obtained. This kind of inefficiency was anticipated due to the insufficiency of the data used. Kriging error (kriging variance) associated with the generated maps was found to be quite large especially in the areas far from the control wells indicating the considerable inaccuracy and confirming the unreliability of the results obtained (Figure 46). Therefore, more well data are highly recommended for kriging especially in the absence of seismic data in order to get acceptable results since kriging results are prone to serious errors when the control wells are too few to capture local variability of the property under study.

5.3.4. COLLOCATED COKRIGING:

Cokriging method was introduced to solve the problem of insufficient well data by incorporating acoustic impedance, which showed a good correlation with the porosity values at well locations. The value added by this secondary data (Figure 47)

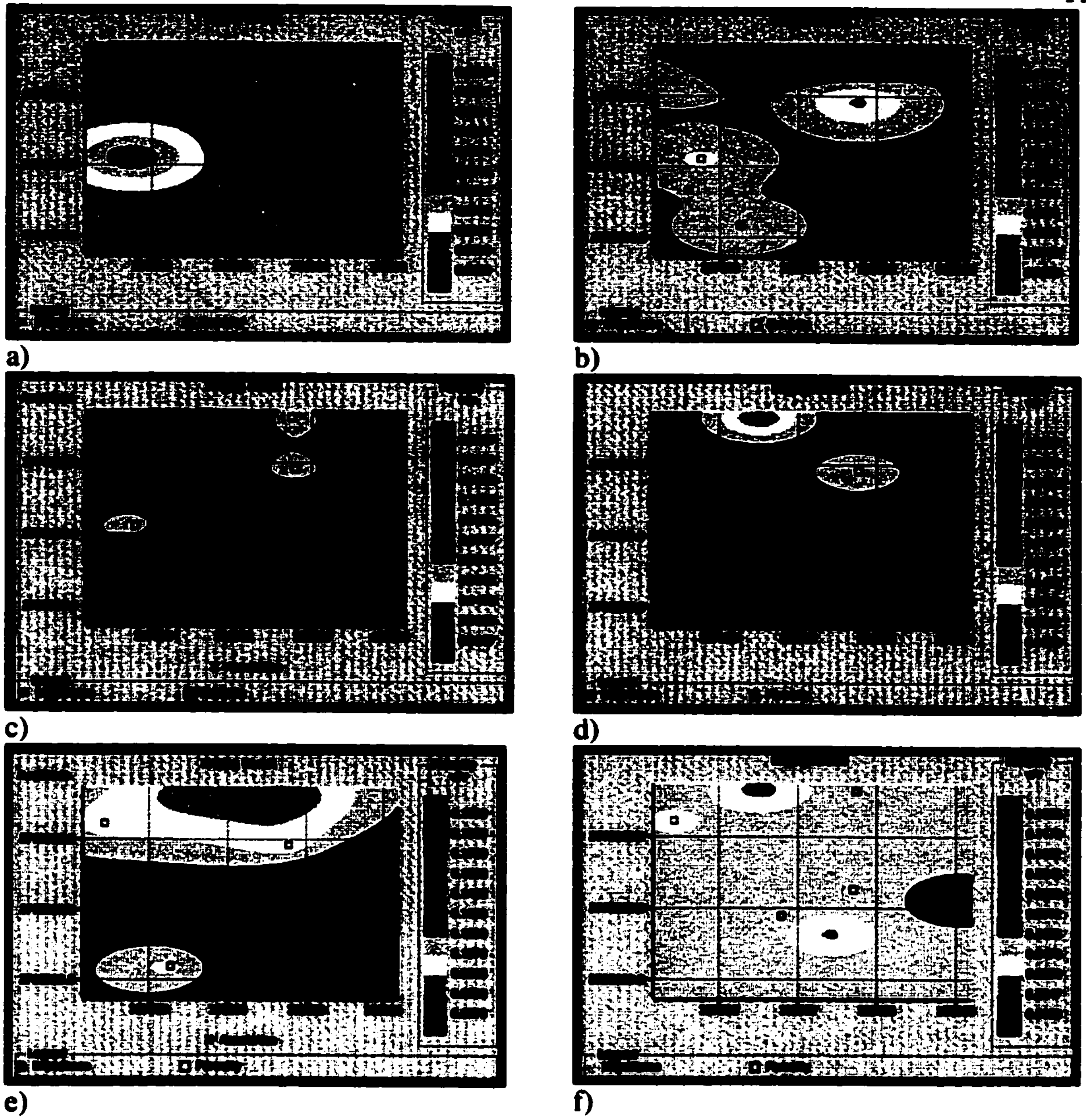

a) b) c) d) e) f)

Figure 45: Kriging maps for slices passing through different reservoir zones: a) zone1, b) zone 2A, c) upper zone 2B, d) lower zone 2B, e) zone 3A and f) zone 3B. As seen, kriging maps could not properly reveal porosity variation within different zones

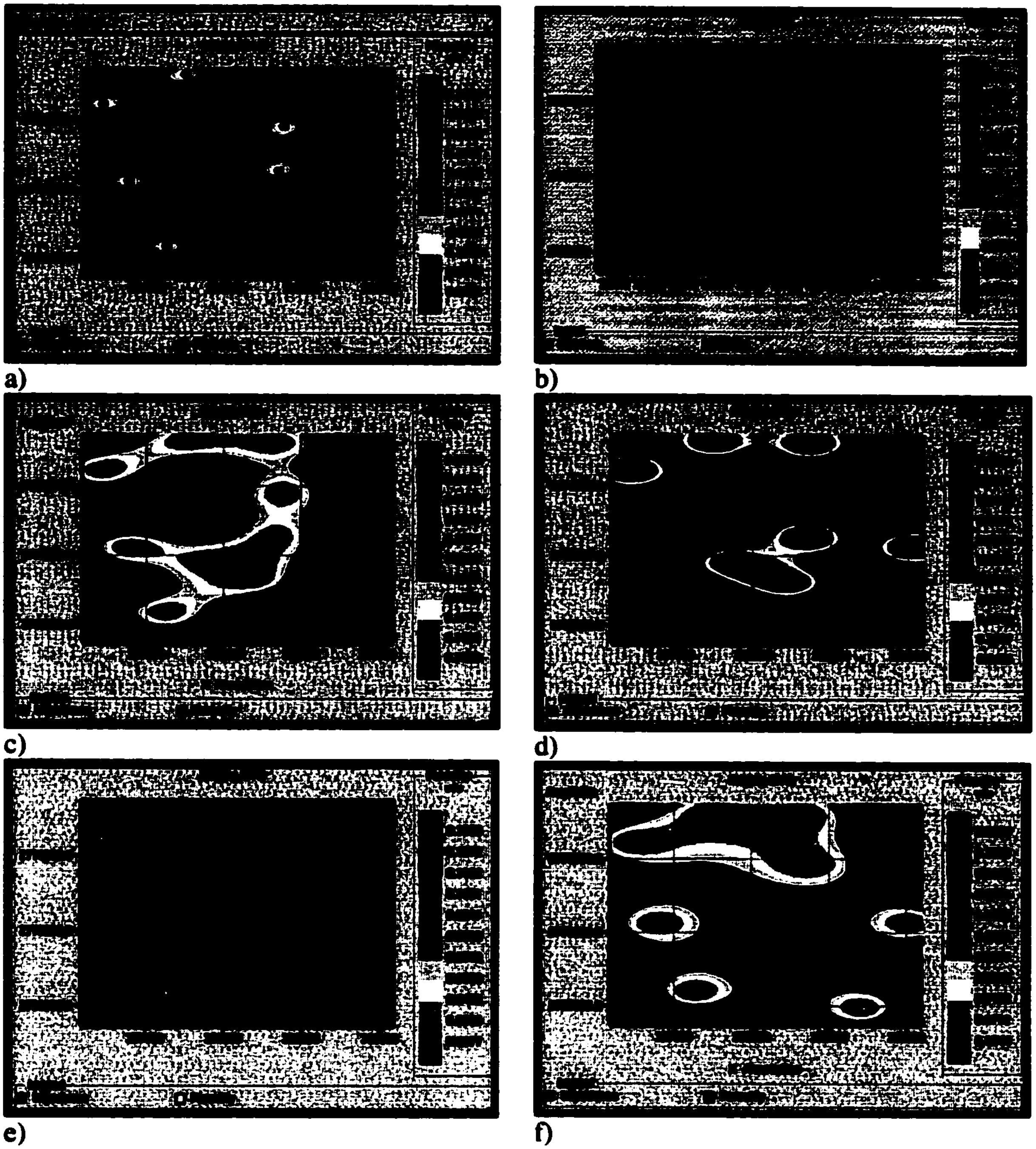

a)

b)

c)

d)

e)

f)

Figure 46: Kriging error maps for slices passing through different reservoir zones: a) zone1, b) zone 2A, c) upper zone 2B, d) lower zone 2B, e) zone 3A and f) zone 3B.

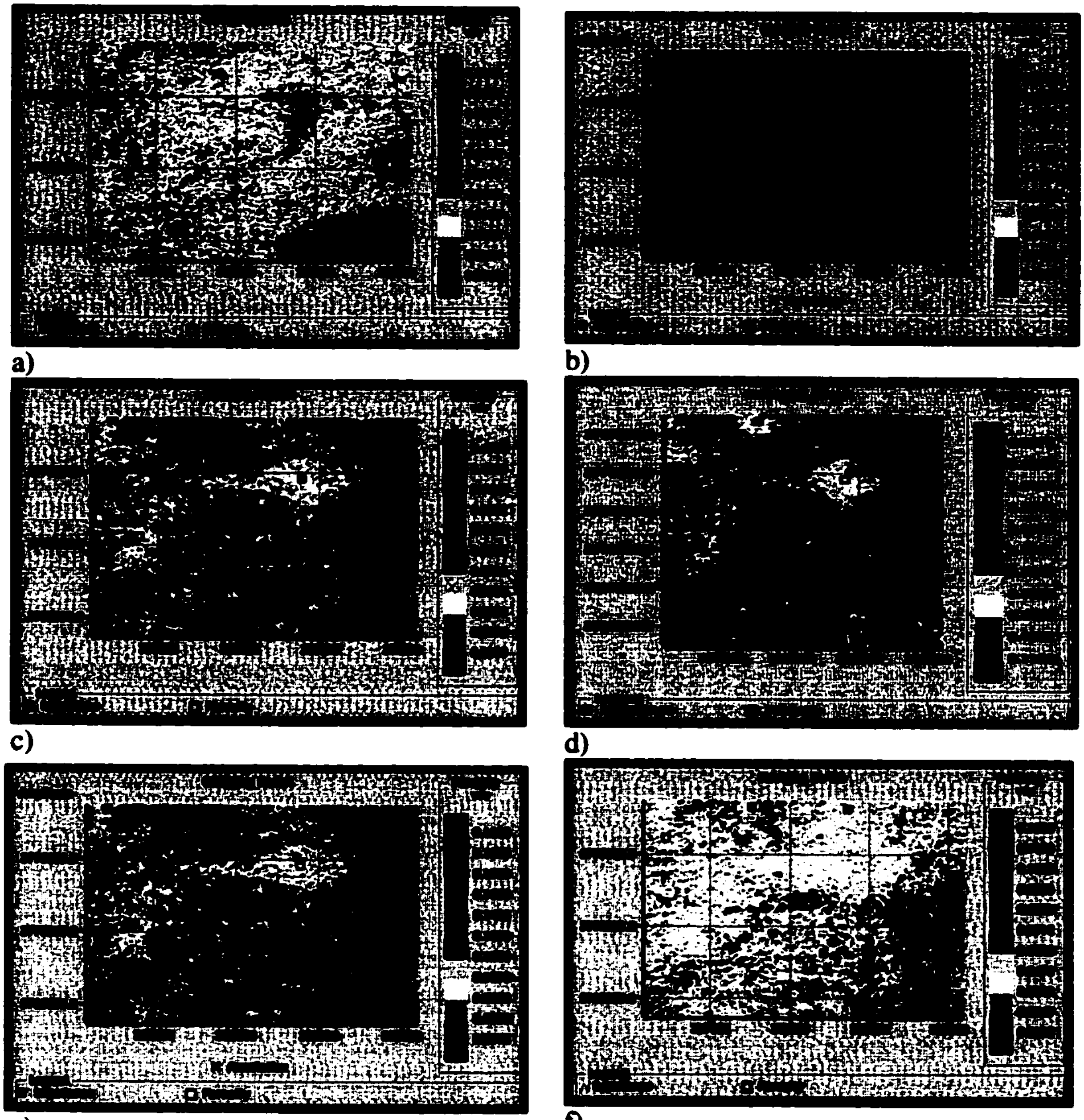

a)

b)

c)

d)

e)

f)

Figure 47: Cokriging maps of slices passing through different reservoir zones, a) zone1, b) zone 2A, c) upper zone 2B, d) lower zone 2B, e) zone 3A and f) zone 3B. The final porosity output maps have a good resolution similar to that of the incorporated seismic data

is the dense distribution over space, which is inherited from the original seismic data. Hence, the final porosity output maps would have a good resolution similar to that of the seismic data. This results in removing the effect of smoothing and inappropriate extrapolation associated with kriging. Cokriging and Sequential Gaussian Simulation are considered as the most common used methods to better integrate seismic data (Srivastava, 1994).

The resulting cokriging porosity maps showed a very excellent resolution capturing much variability than did the kriging maps. Besides, accuracy obtained by cokriging maps is much higher than that associated with kriging maps. Generally, cokriging error in all of the generated maps is ranging from zero to 0.055 v/v (5.5%) (Figure 48) indicating the great improvement achieved through the integration of another type of data. Also, the validation error at each well was measured to test the accuracy and the predictive power of the method. All the maps showed relatively small validation errors ranging from zero and 0.066 (Figure 49). It is noticed that these errors are great compared to the equivalent cokriging errors. This is attributed to the exclusion of the predicted well in the calculation of the validation error. It's also quite observed that the greater the number of the wells used in the analysis, the less the error encountered in each map.

The cokriging proved to be a robust method and succeeded to overcome the problem of inadequacy resulting from lack of sufficient well data. Nevertheless, the porosity distribution of the generated cokriging maps is greatly dominated by the trend of seismic data. This drawback was anticipated due the incorporation of the very dense seismic data with the very sparse and little well data.

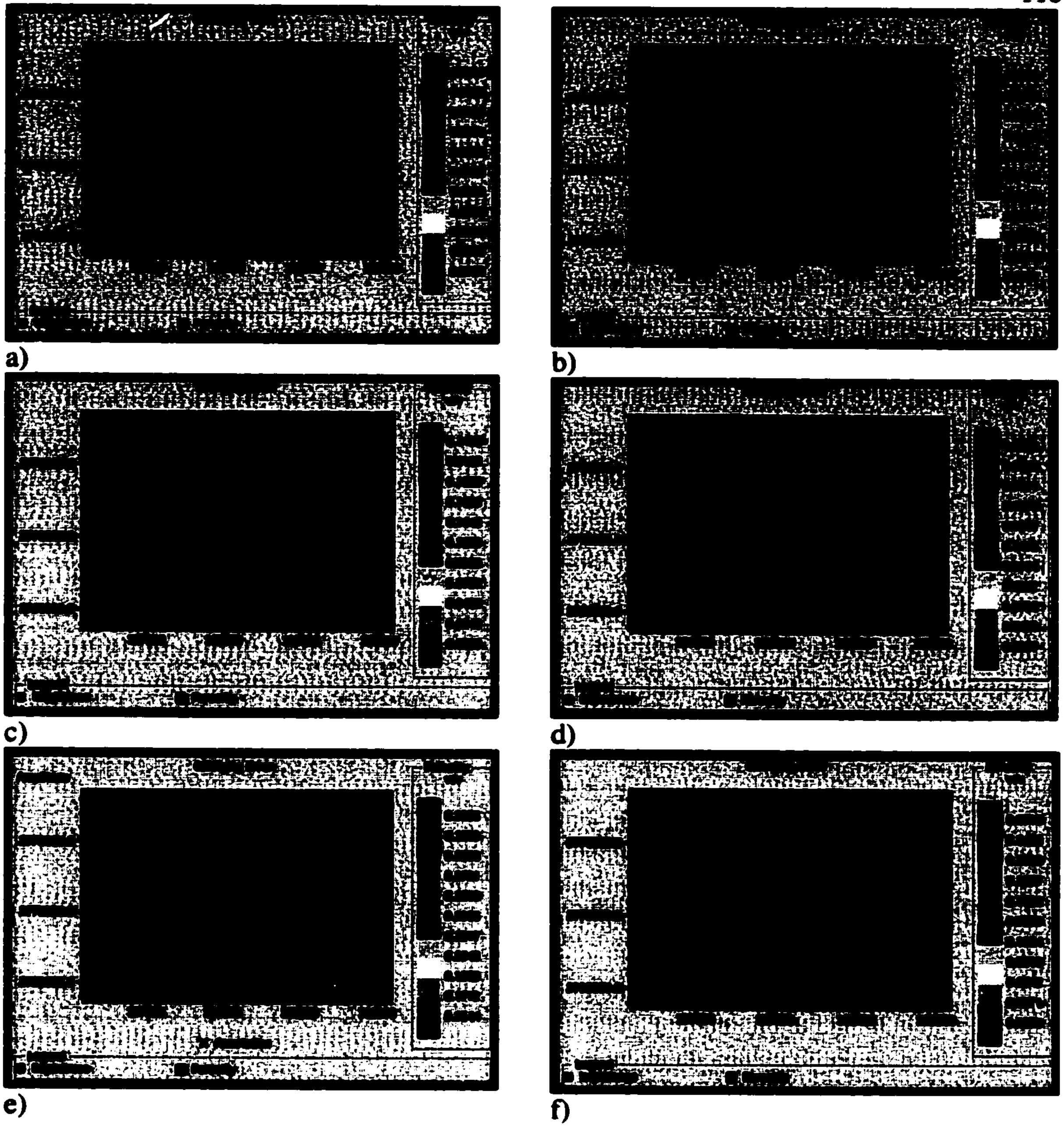

Figure 48: Cokriging error maps of slices passing through: a) zone1, b) zone 2A, c) upper zone 2B, d) lower zone 2B, e) zone 3A and f) zone 3B. It is quite noticed that accuracy obtained by cokriging is much higher than that associated with kriging indicating the improvement achieved through the integration of seismic data

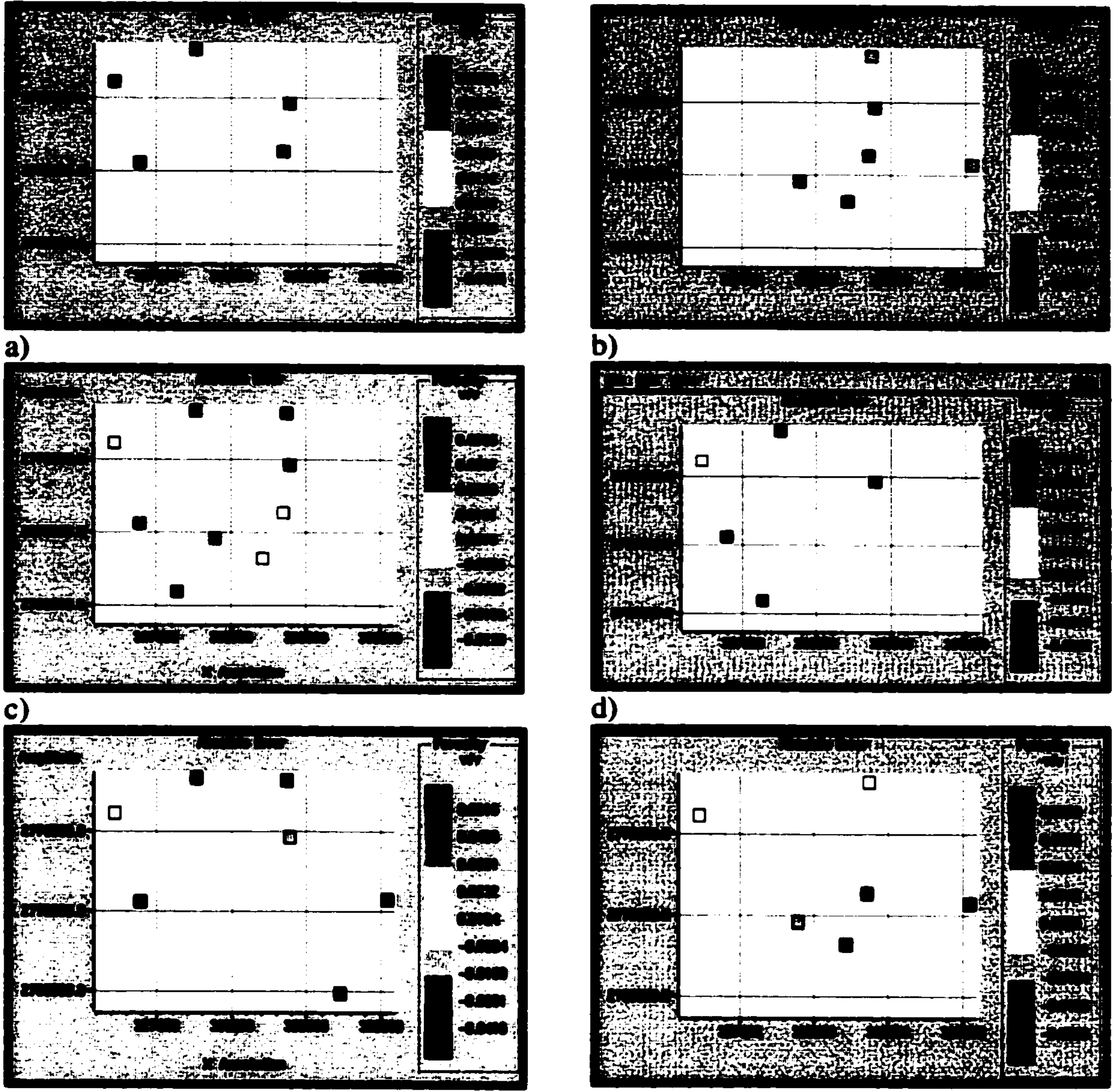

a) b) c) d) e) f)

Figure 49: Validation error maps of slices passing through: a) zone1, b) zone 2A, c) upper zone 2B, d) lower zone 2B, e) zone 3A and f) zone 3B

5.3.5. SEQUENTIAL GAUSSIAN SIMULATUION:

This type of simulation is the most commonly used and most straightforward type of simulation for generating images or realizations of the variable under study. Many examples of the use of the sequential Gaussian with cokriging to integrate seismic information have been provided during the last few years (Srivastava, 1994). By switching from kriging to cokriging, Sequential Gaussian Simulation could honor the correlation between rock property and seismic information.

Countless examples exist of reservoir performance predictions whose failure is due to the use of overly simplistic models. Most traditional methods for reservoir modeling end up with a model that is too smooth and continuous, gently undulating from one well to the next rather than showing the interwell variability known to exist. Such smoothness commonly leads to biased prediction and poor development plans. Srivastava (1994) argued that even a single outcome from stochastic approach is a better basis for performance prediction than a single outcome from a traditional technique that doesn't honor reservoir heterogeneity.

Simulated porosity maps using the same variograms previously generated were constructed. Normal score transforms were done using the local cdf of the porosity data available from the well information. Twenty images of porosity at each slice were produced and all were nearly similar. The twentieth image taken as an example at each slice is displayed in Figure 50. It is quite obvious that unlike the maps resulted from kriging; all of the simulated maps don't show any smoothing effect between wells. This is closer to reality known that porosity is not smoothly distributed property. However, the effect of the dominance of seismic trend could also be observed. This limitation could be attributed to the redundancy of the seismic samples.

Since simulated porosity maps do better honor heterogeneity, they could be more capable of revealing the real underlying geology and therefore they were used to interpret porosity distribution across the different zone of the reservoir.

In the slice map passing through zone1, porosity values are extremely low ranging from zero to 3.8%. Much lower porosity values are present at the southeastern area and the central area in which they follow a northeastern trend. Relatively higher values are sporadically distributed over the entire survey with some concentrations on the eastern, northwestern and southwestern areas (Figure 50a). This complex distribution pattern echoes the transitional nature (due to facies changes) of this reservoir zone. A probability map at this zone showing probability of finding values higher than 3% indicated that these values are most probably limited to small areas, whereas most of the zone is dominated by much more smaller values (Figure 51a). This was better enhanced by using a simulation indicator map applying the same search criterion with 90% confidence. This map showed how this range of values is restricted to only limited small areas (Figure 52a). Such types of maps are very useful for drilling plans and optimization of well site selection since they facilitate precise depiction of probable producing zones.

Slice map 2, passing through zone 2A, gave very high porosity values compared to the previous zone. The highest values are located at the central part of the eastern flank area. Other local high porosities at the southern part of the central area, southwestern area and northwestern area were also observed. Where low porosity values showed a general northeastern trend throughout the entire survey (Figure 50b). A probability map defining areas with probable values higher than 10% showed that these values could be found within the high-porosity areas to the central east, south and northwest. For this high-porosity range, an indicator map of 90% confidence showed a wide distribution of these values (Figure 51b) and (Figure 52b). The increase in porosity values on the flank area may reflect syndepositional structural growth and concentration of highly porous gain carbonates (Daetwyler, 1987). It may also be attributable to the development of local minor fractures known to be dominant in these areas. The decrease in porosity on the flank to the south probably reflects degradation of reservoir due to dolomitization.

The highest porosities within the reservoir were observed in slice 3, which passes through the upper part of zone 2B. Most of the zone is dominated by high porosities (> 18%) especially the southern part of the central area, northwestern area and the central part of the flank area (Figure 50c). A probability map and an indicator map with 90% confidence showed that the entire zone has porosities higher than 10% (Figure 51c) and (Figure 52c). Lower part of zone 2B displayed moderate to high porosity values (Figure 50d). Porosity distribution reflects the extreme heterogeneity of this part of the zone. Core descriptions made for this area indicated that the occurrence of dolomitization in zone 2B gives rise to reservoir inhomogeneities (Cantrell et. al., 2001). The probability and indicator maps of this part indicated that high porosities (> 10%) are prevailing over the entire map of this part of the zone (Figure 51d) and (Figure 52d). Much of the porosity variability in this zone is attributable to dolomite diagenesis (Powers, 1966). Vugular and moldic porosities are common in zone 2B especially in its basal part (Daetwyler, 1987) indicating postdepositional fabric selective leaching of skeletal debris after dolomitization.

Zone 3A showed moderate porosity values, which generally increase eastward and southward with local high-porosity area to the northwest (Figure 50e). The majority of the zone showed porosities higher than 10% (Figure 51e) and (Figure 52e).

Porosities in zone 3B are lower than those of zone 3A, yet larger than those of zone1. The highest values concentrate on the flank area (Figure 50f). Very small area could have porosities higher than 10% (Figure 51f) and (Figure 52f).

Generally it is believed that porosity distribution is affected by facies and diagenetic factors. This became quite clear because of the obvious consistency between porosity distribution and facies distributions predicted from seismic inversion analysis. Geostatistical techniques proved to be very efficient in mapping porosity distribution in this area using only the limited well information. Nevertheless, it showed a great inadequacy when applied to permeability modeling giving absolute error greater than 187 md. This necessitates the application of the newer multiattribute transforms and neural network technique, which is more capable of addressing the problem of permeability modeling due to the involvement of non-parametric transformations that helps build a good relationship between permeability and seismic attributes and thus increase the predictive power of the method used.

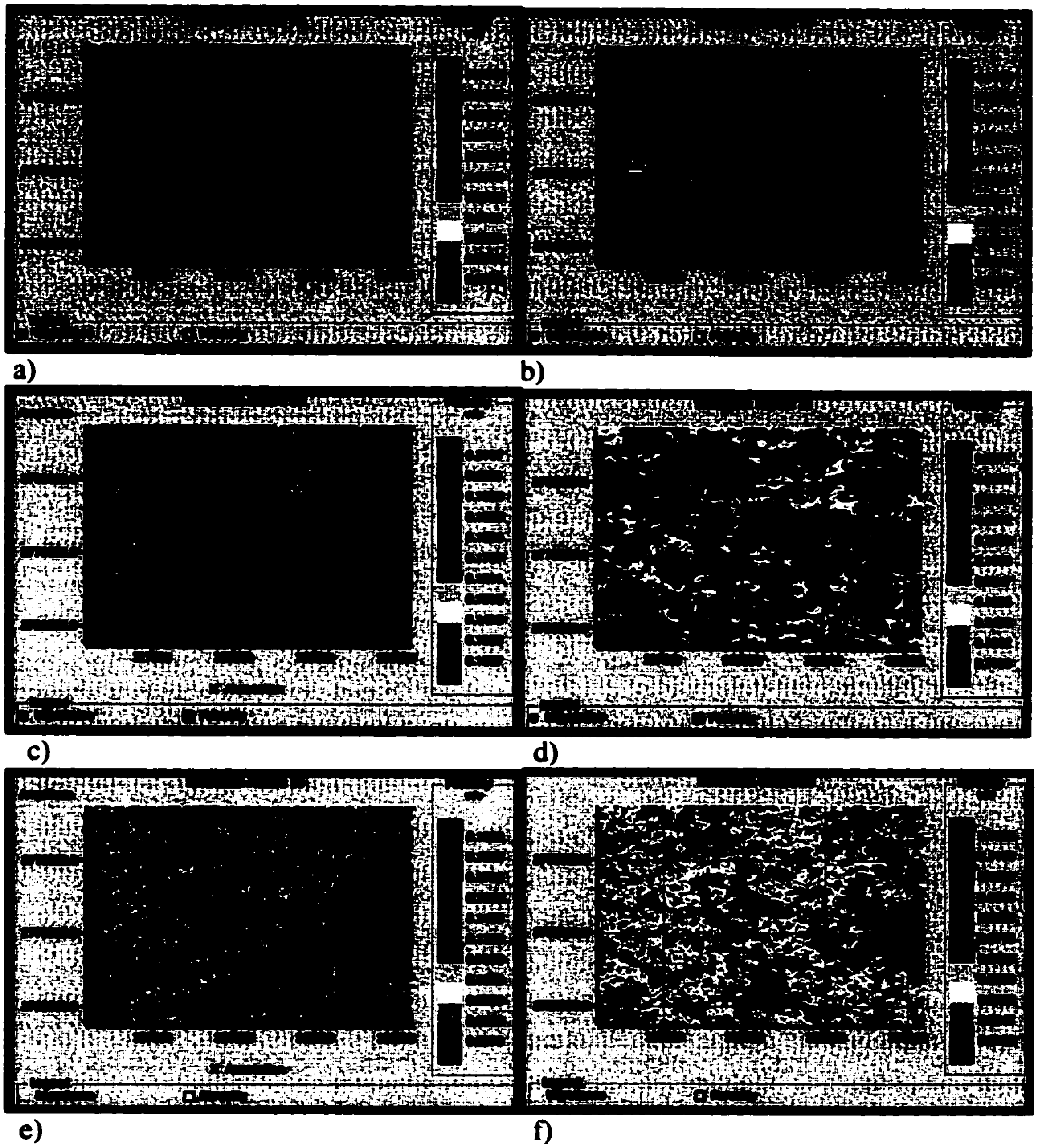

Figure 50: The twentieth simulation images of slices passing through: a) zone1 b) zone 2A, c) upper zone 2B d) lower zone 2B, e) zone 3A and f) zone 3B

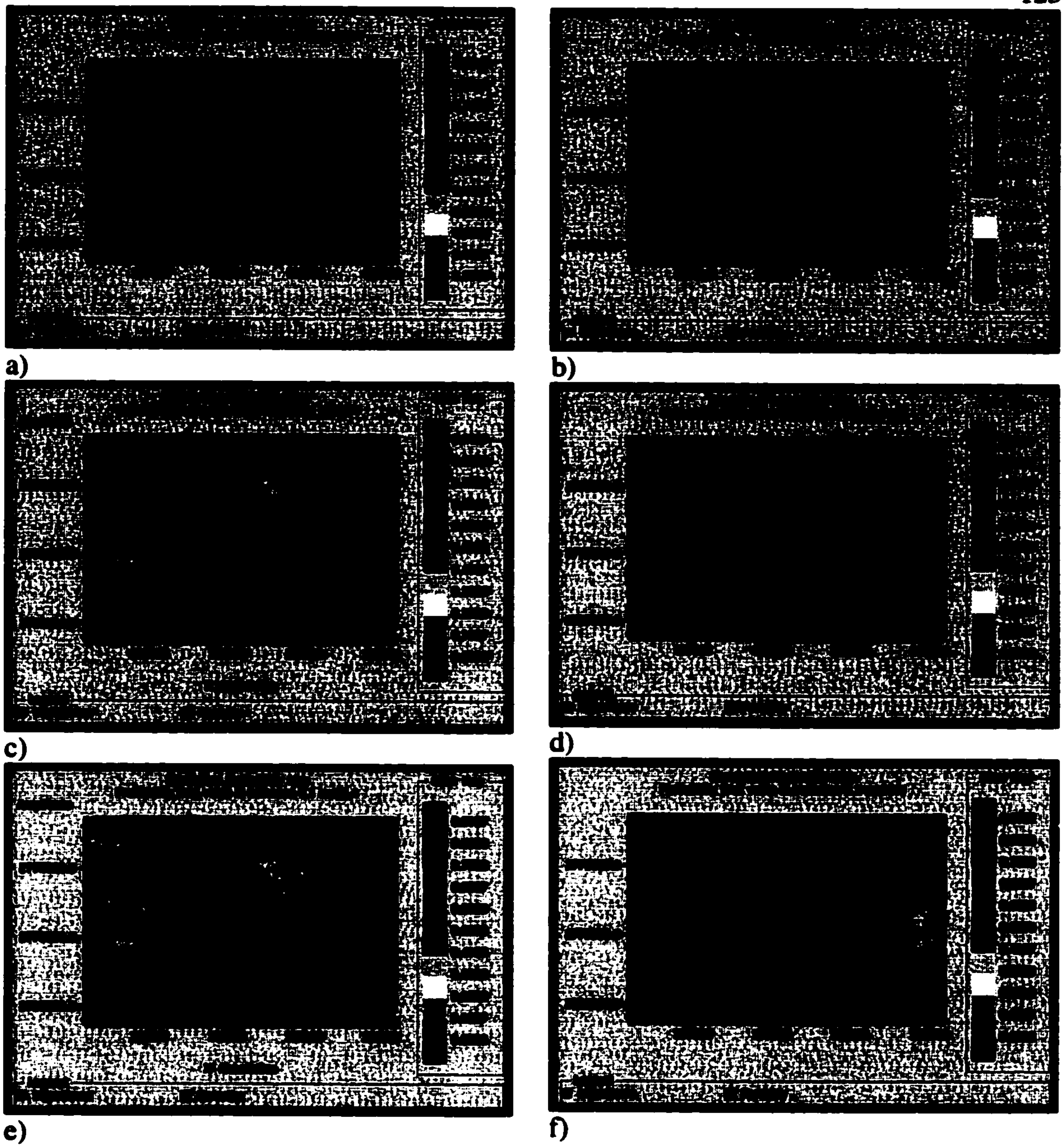

Figure 51: Probability maps of slices passing through: a) zone1 b) zone 2A, c) upper zone 2B d) lower zone 2B, e) zone 3A and f) zone 3B

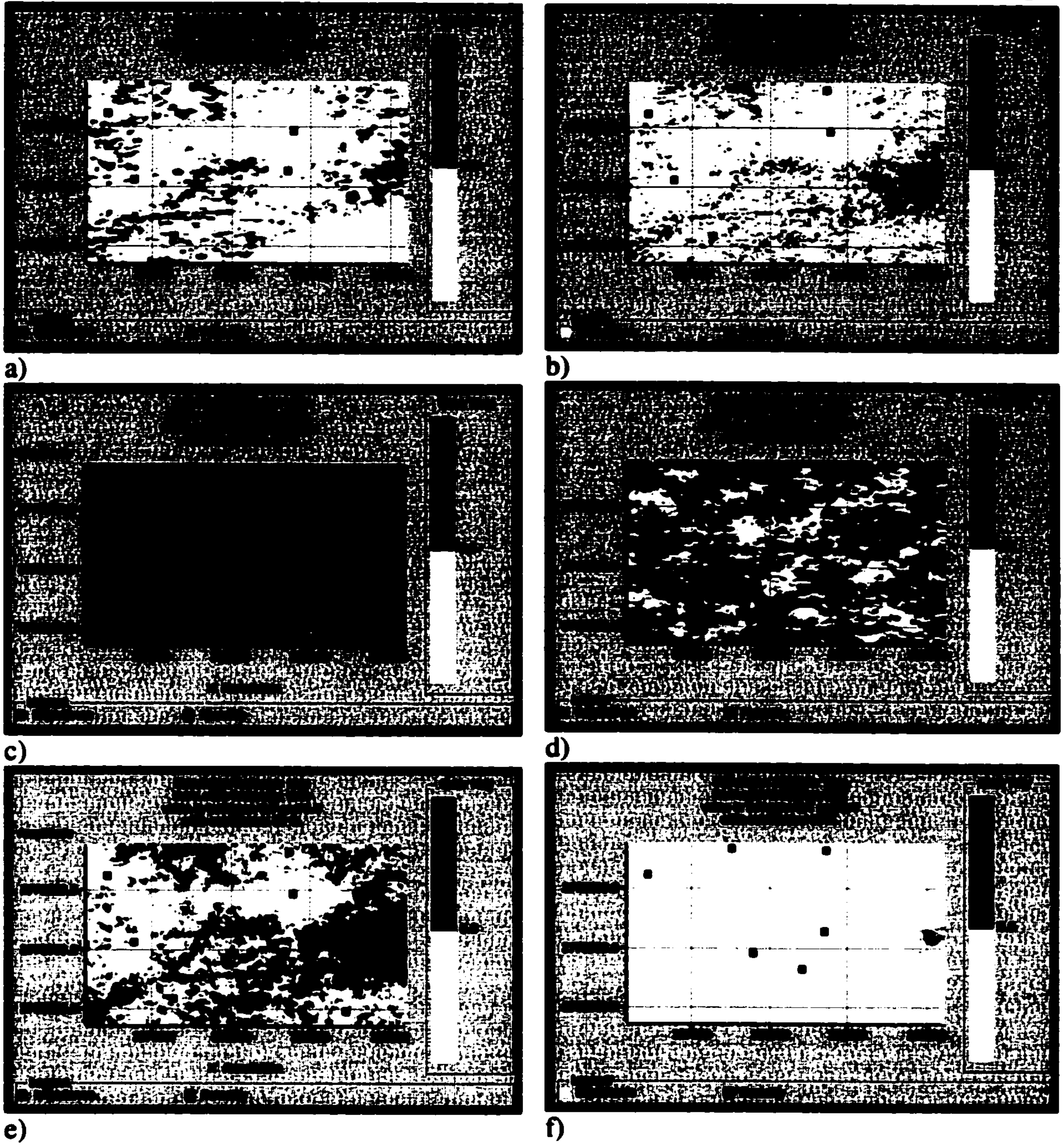

a) b) c) d) e) f)

Figure 52: Indicator maps of slices passing through: a) zone1 b) zone 2A, c) upper zone 2B d) lower zone 2B, e) zone 3A and f) zone 3B

5.4. MULTIATTRIBUTE TRANSFORMS AND NEURAL NETWORK ANALYSIS

As previously stated, multiattribute analysis is a growing area of specialization within geophysics related to attributes and statistics. This idea is to extract many attributes from a 3-D seismic data set, and then do multiple regressions on these against important parameters from well control hoping that a meaningful relationship will emerge. Clearly, some attributes are highly correlated with well parameters while some are not. The method starts by approximating this mapping operator that relates seismic responses to well parameters using multi-attribute regression and the neural network technology trained by the data set consisting of well data as desired output and seismic recording recordings near each well as input. Using the mapping network in this study, the seismic data are mapped into well parameters, trace by trace, to extrapolate these parameters. Twenty seismic attributes were initially extracted from the seismic data to be used for correlation with log properties. Inversion result was also incorporated as an additional external attribute where seismic porosity generated by this method was used instead as an external attribute for permeability modeling.

5.4.1. POROSITY MODELING:

Modeling porosity using this method was necessary to test its accuracy by comparing results obtained with those of the geostatistical analysis. The direct impedance-porosity relationship was expected to immensely increase the predictive strength of this method. However, when tested, it didn't show a satisfactory level of correlation and prediction accuracy. When linear regression was applied using only impedance data, the resulting error was 6% and the correlation was only 0.522 (Figure 53). Therefore,

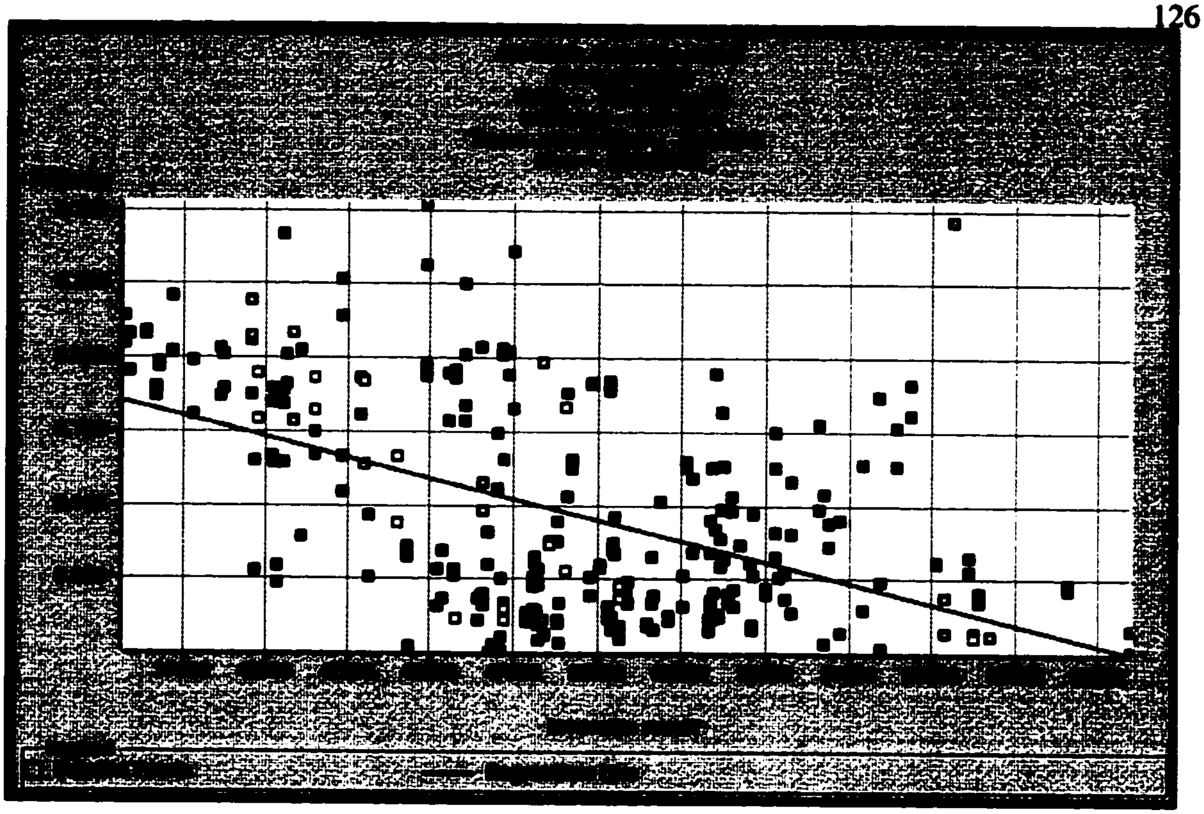

Figure 53: Cross-correlation between porosity and impedance

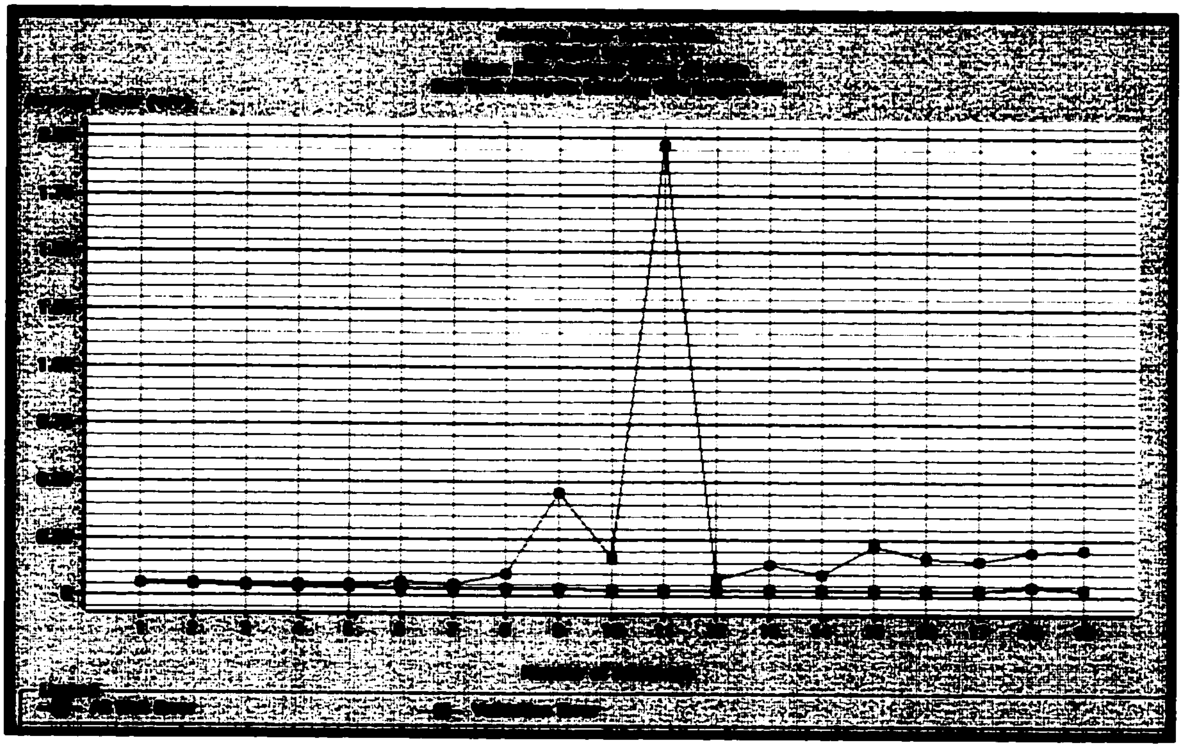

Figure 54: Average error and validation error of porosity prediction for all wells

additional seismic attributes were introduced to the analysis in search for better results.

The best eighteen attributes that can be used to predict porosity and impedance were initially selected utilizing a multi-attribute step-wise linear regression supported by a convolutional operator. The first three attributes proved to be the best among the selected attributes and hence they were selected to be used in the subsequent application of the multi-attribute regression on the seismic volume (Figure 54). It can be obviously noted that attributes comes after the third one don't participate in improving the prediction power of the algorithm since the validation error abruptly increases after the third attribute. Application of the regression result using three attributes gave an average prediction error of 4.1% where seismic attributes showed a correlation of 0.825 with porosity (Figure 55) and (Figure 56). This considerable improvement over the previous impedance-based analysis and bivariate linear regression became possible after the incorporation of two more seismic attributes namely the integrated absolute amplitude and the amplitude envelope. Absolute amplitude has been widely known as a very useful attribute in detecting lateral changes in sequence amplitude due to changing lithology. Also, the amplitude envelope is considered to be an excellent indicator of major lithology changes (Taner et. al., 1994). The considerable contribution of these attributes to porosity modeling could be understood as porosity distribution in this interval is facially controlled (section 5.2).

Eventually, the analysis was repeated using neural networks, which has the advantage of utilizing both parametric and non-parametric relationship between porosity and seismic attributes. As expected, the application of the neural network analysis using the same attributes considerably maximized the predictive power of the method. The probabilistic neural network algorithm gave a correlation of 0.846 and an absolute average

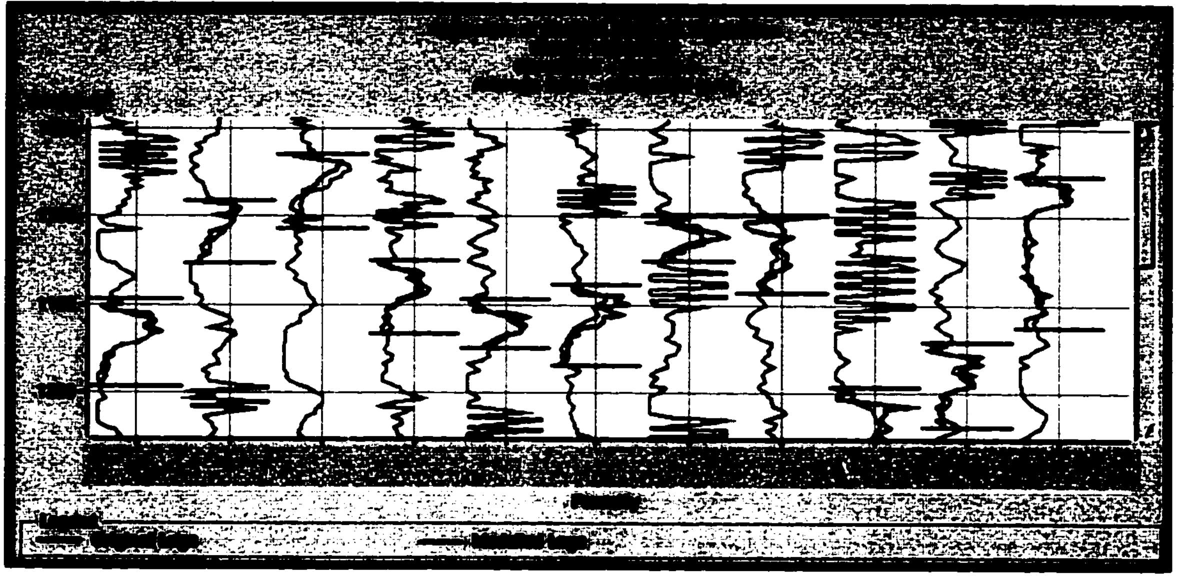

Figure 55: Application of multi-attribute regression for porosity prediction at well locations

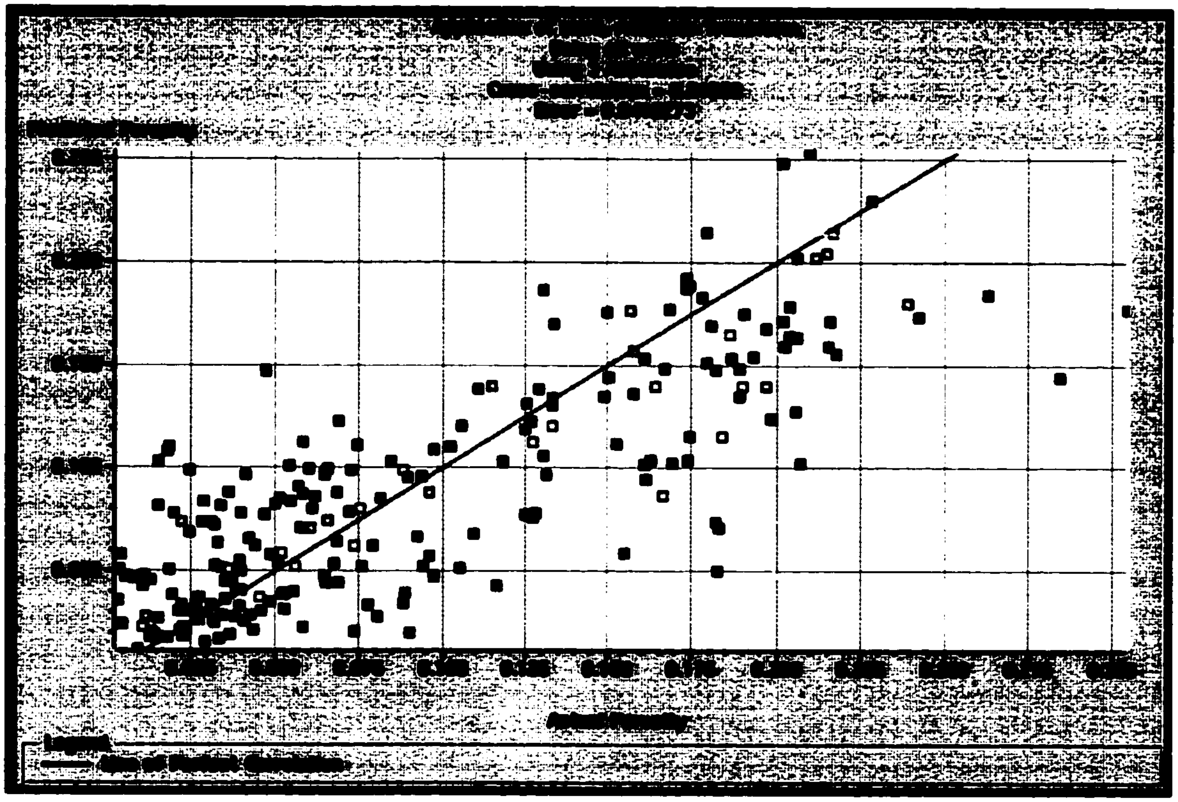

Figure 56: Cross-correlation between actual porosity and predicted porosity using multi-attribute regression

error of only 3.78 % excelling the conventional geostatistical methods (Figure 57) and (Figure 58).

Validation result of the multiple attribute regression showed a correlation of 0.65 and an average validation error of 0.58 (Figure 59). Whereas, the validation of the probabilistic neural network showed a better result with a correlation of 0.677 and average validation error of 0.53 (Figure 60). The degradation of the performance observed in validation was due to the elimination of the well to be predicted from the training data set.

The seismic attributes within the seismic volume were finally converted into porosity by applying the probabilistic network result. The generated model displayed the same porosity distribution obtained in the geostatistical model with slightly much higher resolution. To portray the consistency between the products of the two methods, porosity maps for the same slices used in the geostatistical method were prepared. Some cross-sections showing the porosity distribution in the depth dimension were made to compensate for the absence of the 3-D display (Figures 61 to 68).

Robustness achieved in porosity modeling using probabilistic neural network was a persuasive factor to propose this method for solving the problem of permeability modeling discussed in the following section.

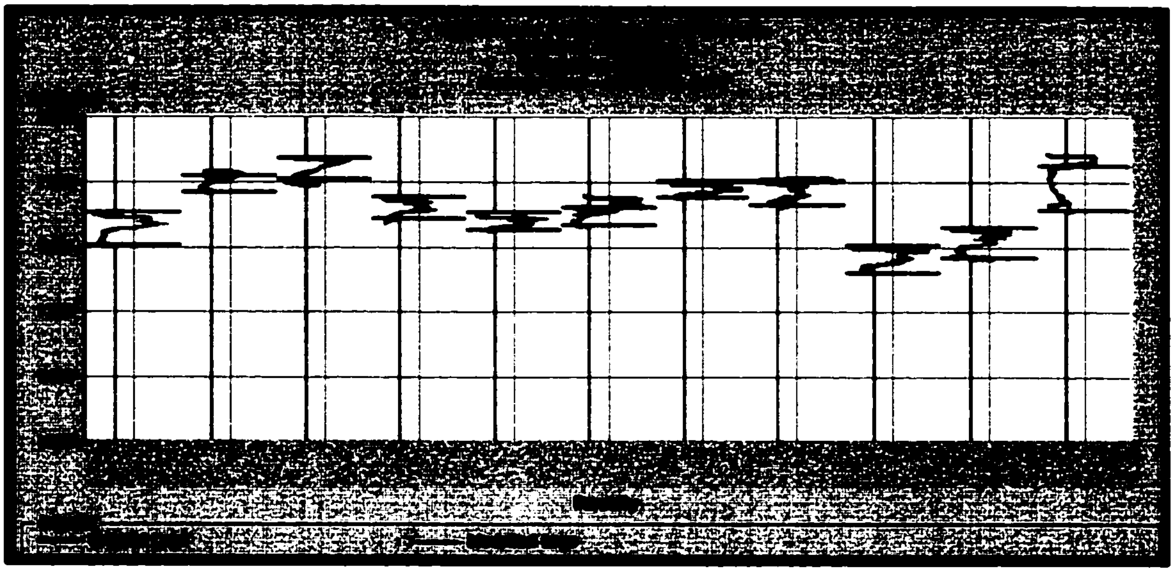

Figure 57: Application of probabilistic neural network for porosity prediction

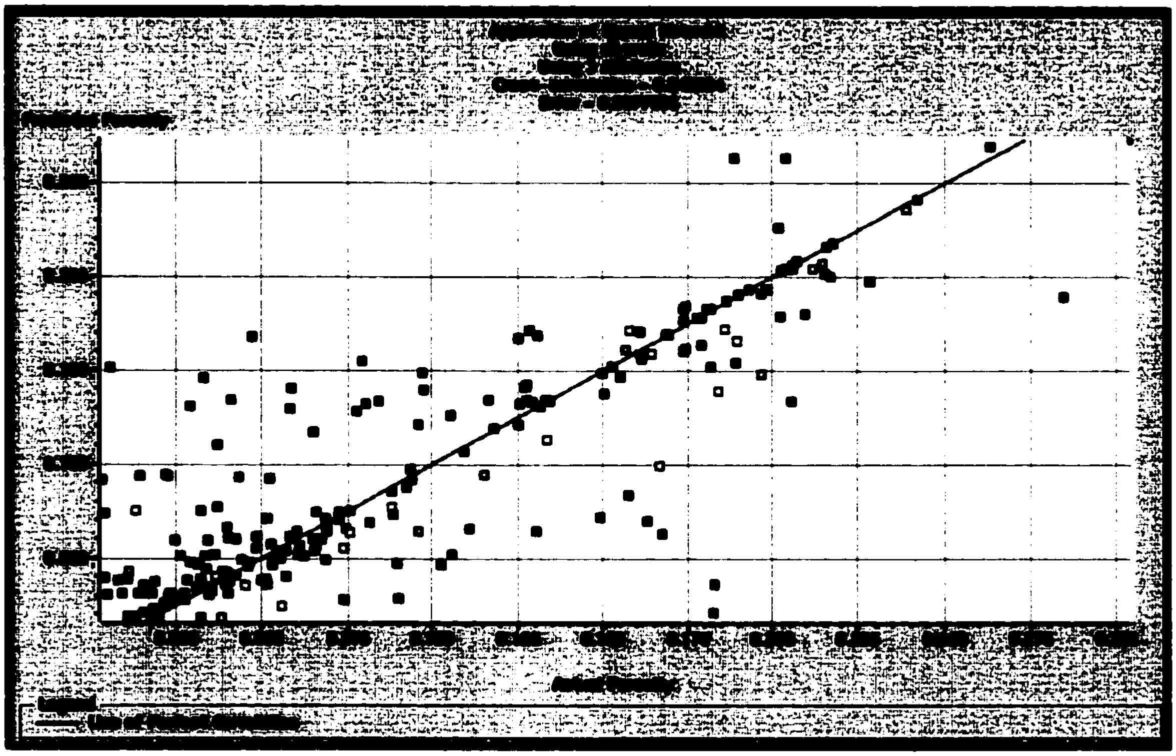

Figure 58: Cross-correlation between actual porosity and predicted porosity using probabilistic neural network

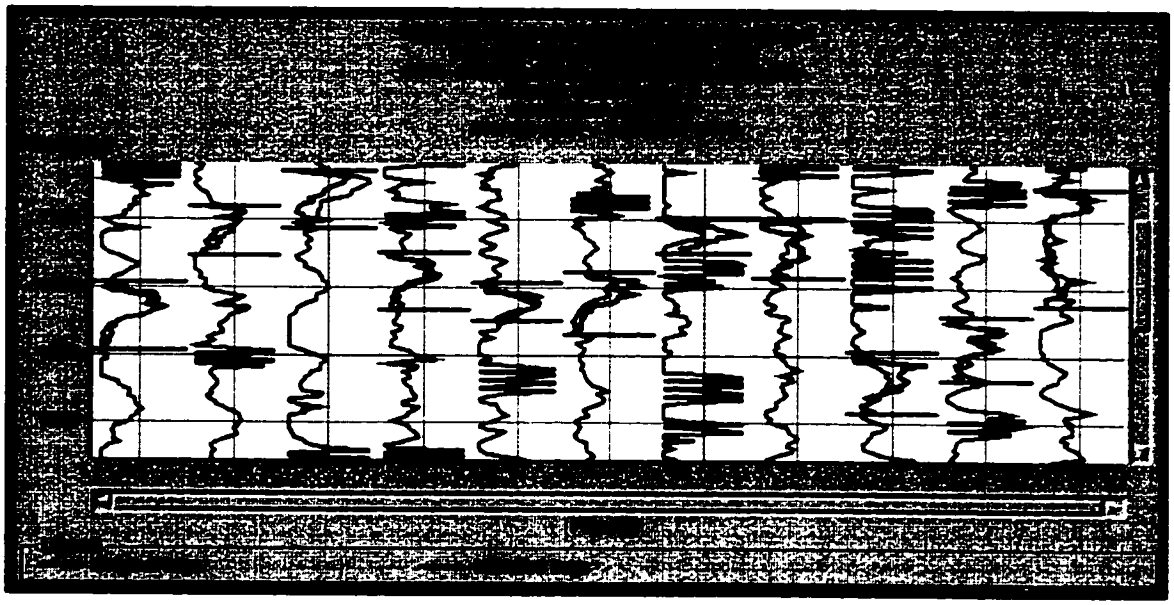

Figure 59: Validation result of the multi-attribute regression for porosity prediction

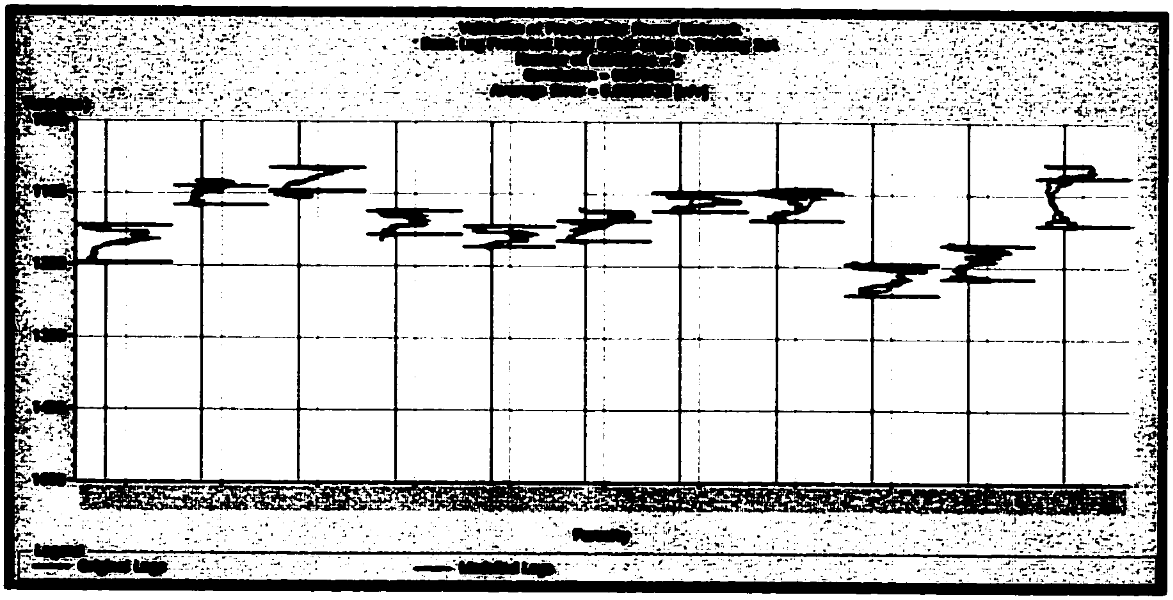

Figure 60: Validation result of the probabilistic neural network for porosity prediction

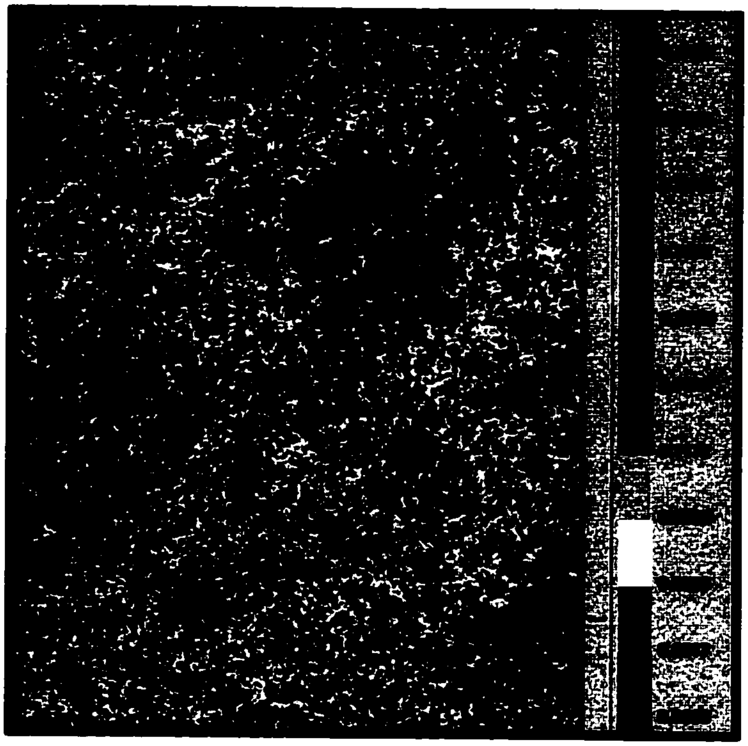

Figure 61: Porosity map for slice1, which passes through zone1

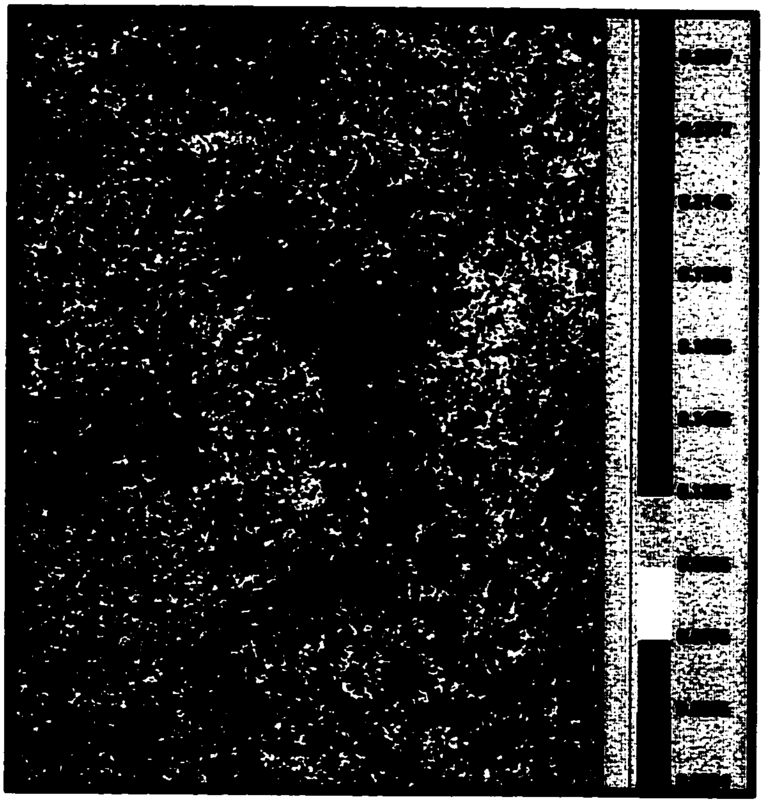

Figure 62: Porosity map for slice 2, which passes through zone 2A

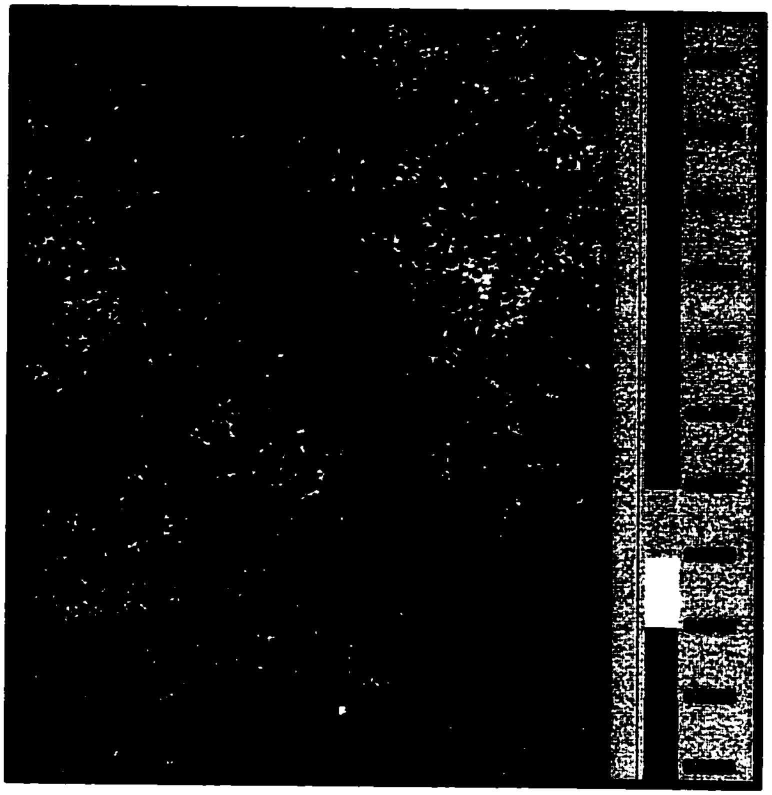

Figure 63: Porosity map for slice 3, which passes through zone 2B (upper)

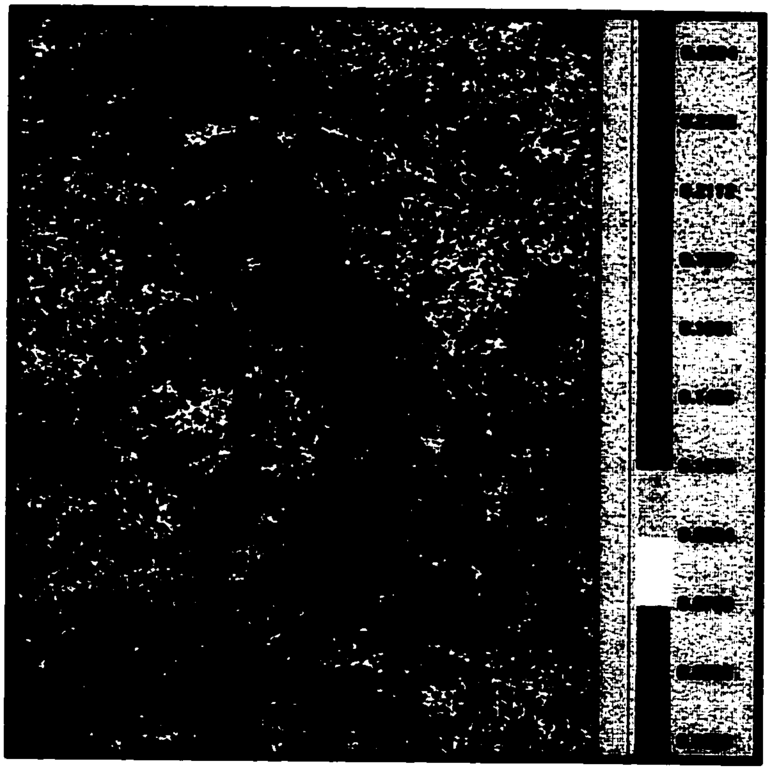

Figure 64: Porosity map for slice 5, which passes through zone 2B (lower)

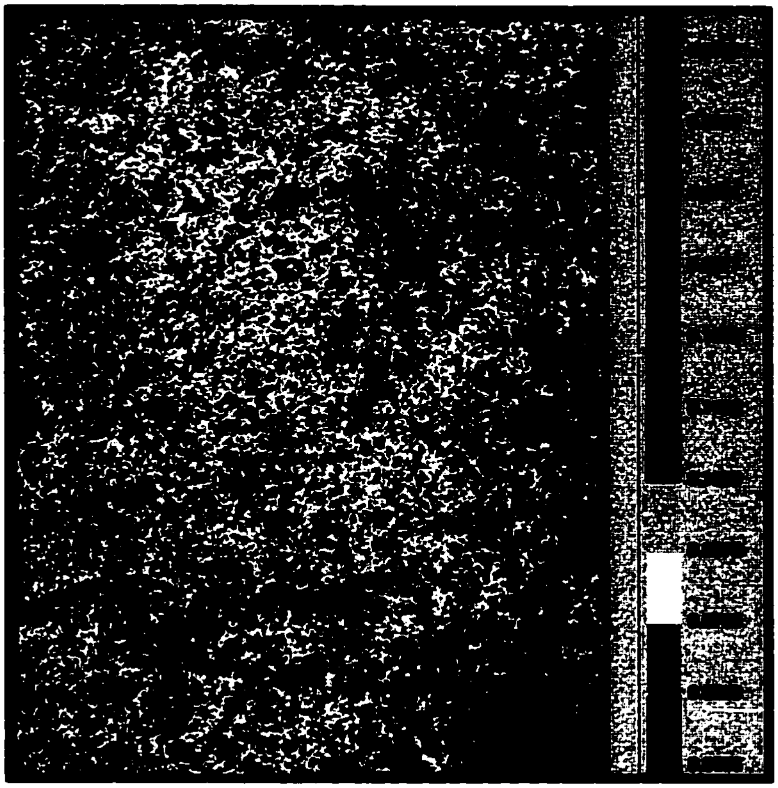

Figure 65: Porosity map for slice 7, which passes through zone 3A

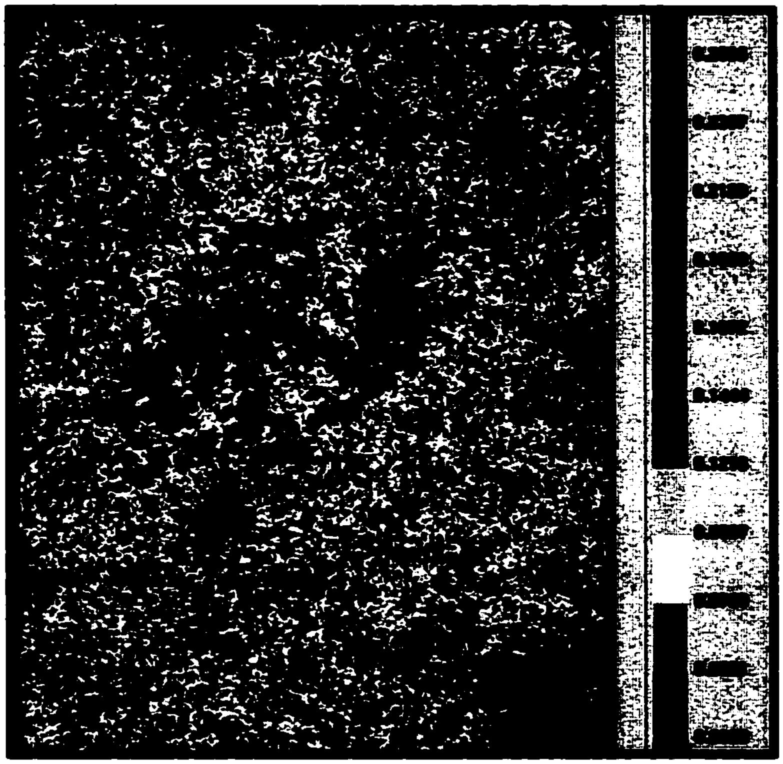

Figure 66: Porosity map for slice 9, which passes through zone 3B

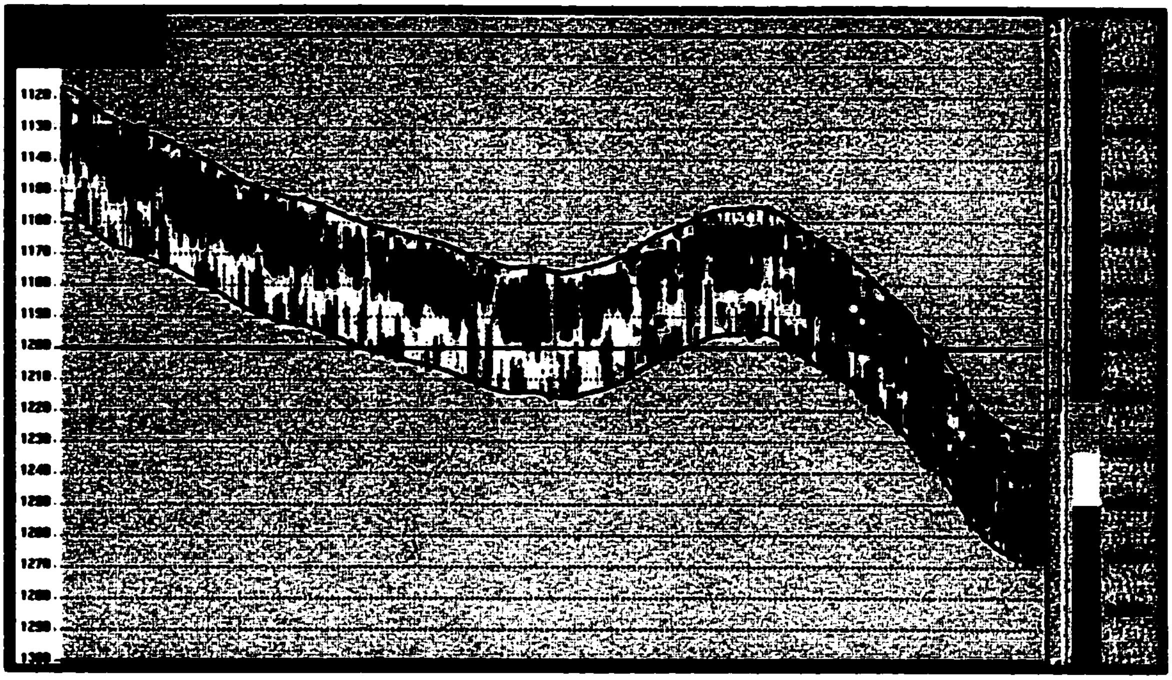

Figure 67: A cross-section along inline 50 showing porosity distribution in the depth dimension

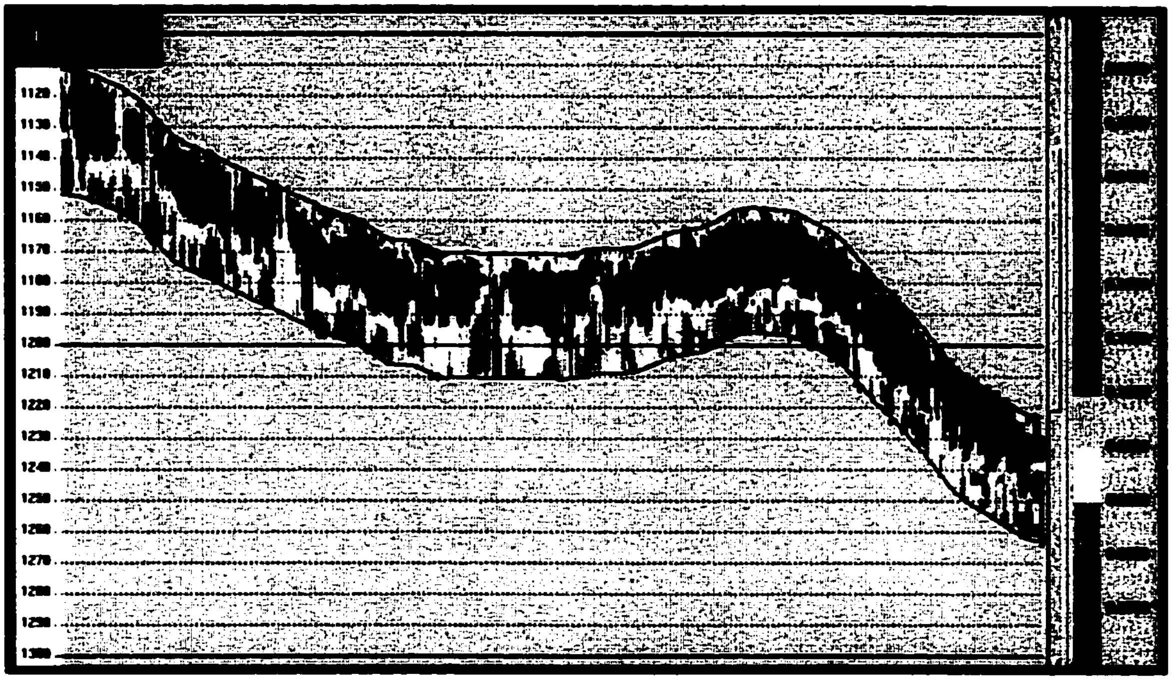

Figure 68: A cross-section along inline 100 showing porosity distribution in the depth dimension

5.4.2. PERMEABILITY MODELING:

The models to explain permeability are commonly assumed to be bivariate (log transform of permeability versus porosity) linear model, which doesn't prove to be always correct. Actual and predicted permeability from the current linear model were compared and a correlation coefficient of about 0.6 was found with an average absolute error about 61.6 md. This questioned the reliability of such a model and provided an additional justification to the great error associated with the permeability geostatistical model (Figure 69). However, porosity is deemed a vital element for deriving permeability and hence it was used in this analysis as another source of information in the form of external attribute to support the analytical power of the seismic-driven attributes.

The best eleven attributes were firstly chosen for a primary multiple regression analysis to evaluate their predictive power to permeability in order to select the best combination to be used for permeability modeling. The first four attributes were objectively chosen for a more robust multiple regression analysis due to the high accuracy they showed. The three seismic attributes that demonstrated the best correlation with permeability in this study are the amplitude-weighted phase, the integrated trace and instantaneous phase. The contribution of the phase components to the analysis is justifiable since it is evident that lateral changes in phase may explain the changes of the bedding character of a specific event. Besides the instantaneous phase is a well-known indicator for event continuity and stratigraphic configuration (Brown, 1996). Although, the study couldn't provide a direct relationship between the integrated seismic trace and permeability and hence it is proposed for further investigation. Given that the mean

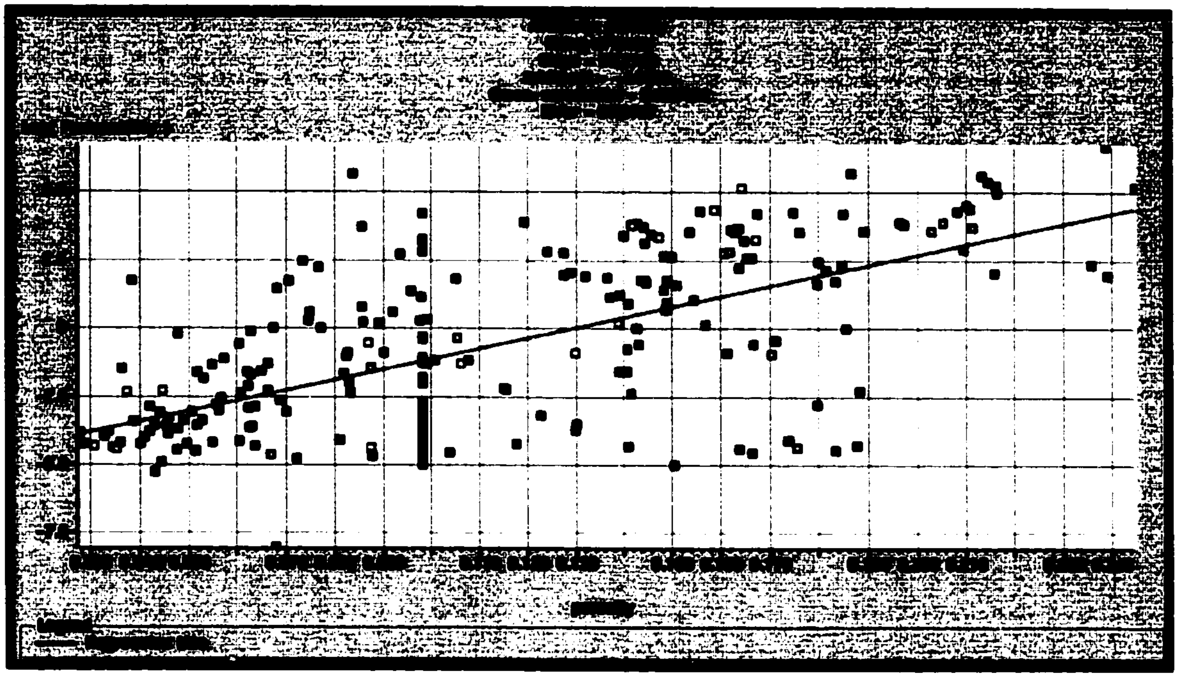

Figure 69: A cross plot for permeability and porosity showing the error associated with such a linear model in predicting permeability

problem in using seismic attributes for property estimation is that their relation to rock properties is not obvious. There are unknown local factors that may affect the data in unexpected ways (Anjos et. al., 2001).

The result of the multiple linear regression using porosity and the best three seismic attributes were first applied to seismic data at well location to test the efficiency of this method. It gave a correlation coefficient of 0.836 with an average error of 36.55 md, which is obviously better than the result previously obtained using only porosity data (Figures 70 and 71).

The same combination of attributes was used in the subsequent neural network analysis they showed even much better result with a correlation coefficient of 0.856 and average error of 34.59 md. This again is due to the implementation of the possible non-parametric relationships between permeability and attributes (Figures 72and 73). When these methods were validated, they gave more biased result than the actual application for example when the multi-attribute regression, a correlation coefficient of 0.69 resulted with an average error of 51.1 md. This is attributable to the decrease in the well information used in training due to the exclusion of the validation well.

Robustness of the PNN method was better than that of multi-attribute regression and far beyond those of the bivariate regression and geostatistical method. Therefore this result was adopted and consequently used to extrapolate permeability in the interwell areas. Many cross-sections cutting the final 3-D model along inline direction were prepared to illustrate the permeability distribution within the reservoir.

Generally, the reservoir displays moderate to low permeability values. The low permeability values dominate the lowest part of the reservoir interval, which includes

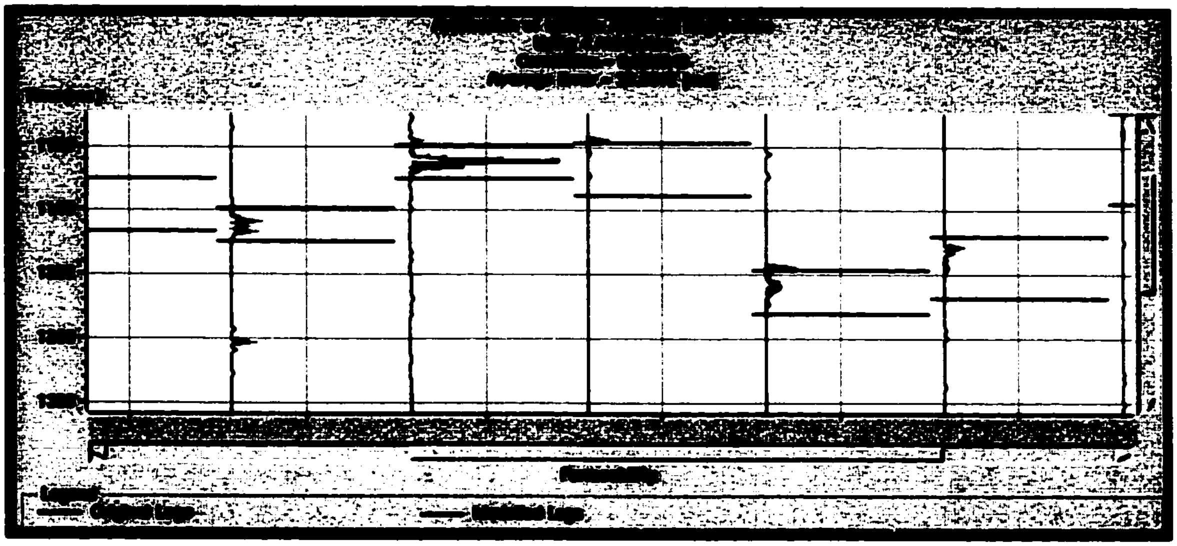

Figure 70: Application of multi-attribute regression to model permeability

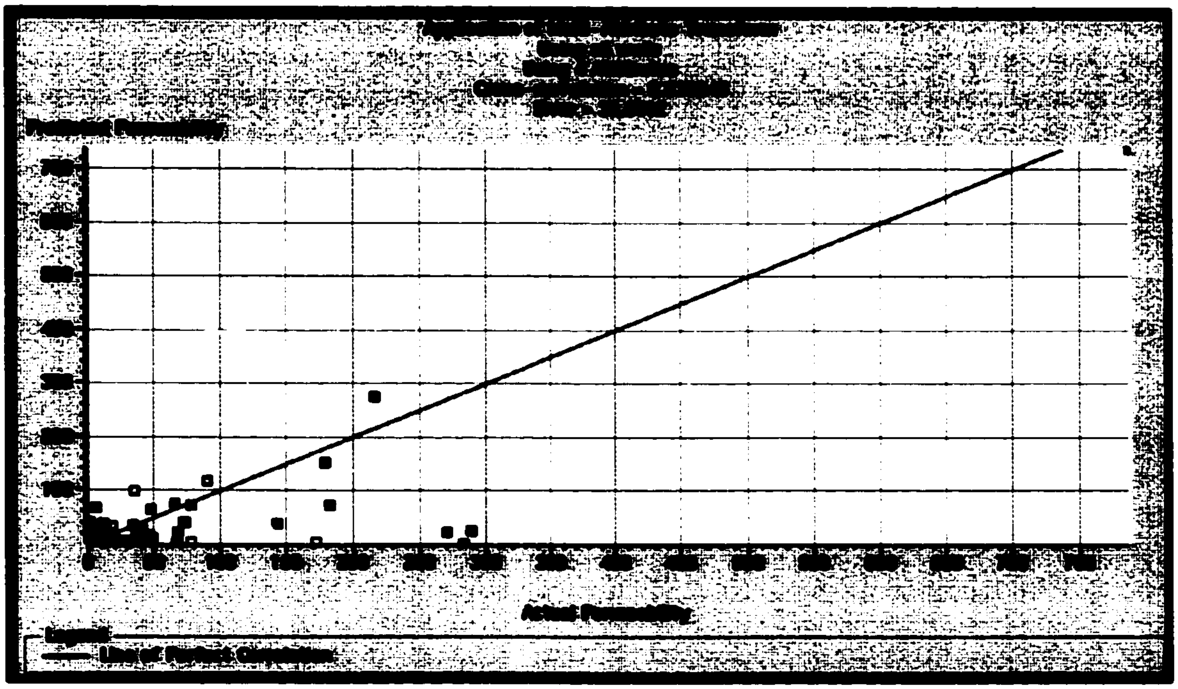

Figure 71: Cross-correlation between actual and predicted permeability using multi-attribute regression

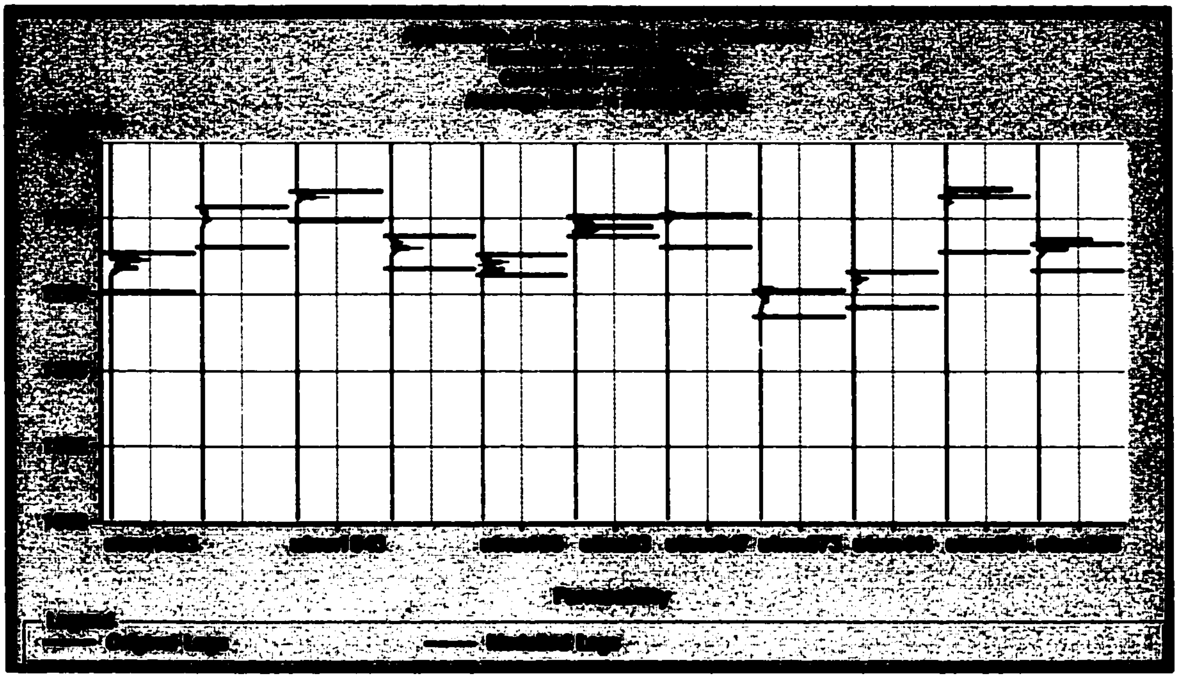

Figure 72: Application of PNN to model permeability

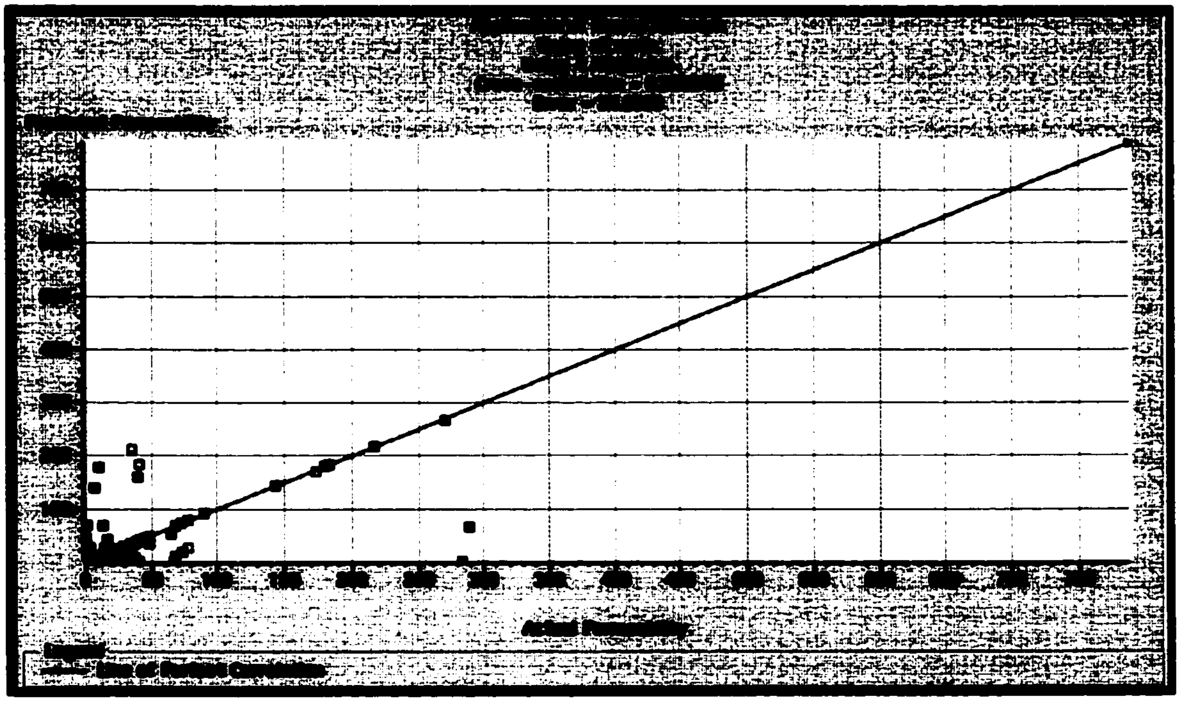

Figure 73: Cross-correlation between actual and predicted permeability using PNN

zones 3A, 3B and 4. This doesn't merely apply on the flank areas, where these zones comprise high permeabilities. The uppermost part of the reservoir, corresponding to zone1, demonstrates very low permeability values.

Moderate to high permeabilities ranging from 66 to 500 md are prevailing over the upper half of the reservoir, which comprises zones 2A and 2B. Extremely high permeability values exceeding 700 md are sporadically disseminated throughout zone 2B, which nearly lies at the lowest part of the upper half of the interval (Figures 74 to 79). In zone 2A overlaying this zone, such permeability values are present but less abundant (Figure 75). Also, these permeabilities were noticed in lower zones (3A, 3B and 4) on the flank area (Figures 74 and 77). They are also rarely present in these lower zones at the flexure of the possible local anticline to the south (Figure 75). As previously mentioned, these very high permeabilities are crucial to production operations since they considerably affect sweep efficiency during injection treatments.

Most of the very high permeabilities encountered in zones 2B and 2A are obviously concordant with areas showing as high porosity as 18%. This suggested that these permeabilities to be mostly resulted from the interconnected vugular and moldic pores associated with the dolomite facies prevailing in these zones. Thus these permeabilities can be described as permeable matrix layers. Very high permeable regions encountered in the lowermost zones on the flank areas were interpreted as to be caused by either fracture clusters or locally dolomitized layers occurring within these zones. Since the compacted muddier carbonates of these zones are expected to be more brittle and susceptible to fracturing, which is most probably triggered by gentle bending of the distal flank. Detailed investigation and modeling of fractures is anticipated to greatly contribute in precisely characterizing the fluid-flow units of the reservoir.

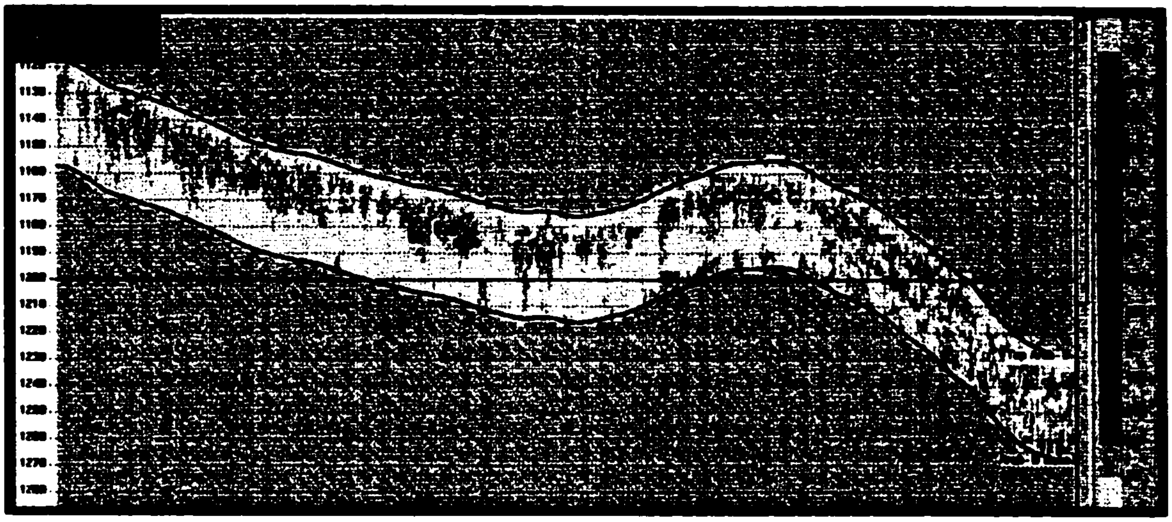

Figure 74: A cross-section along inline 50 showing permeability distribution

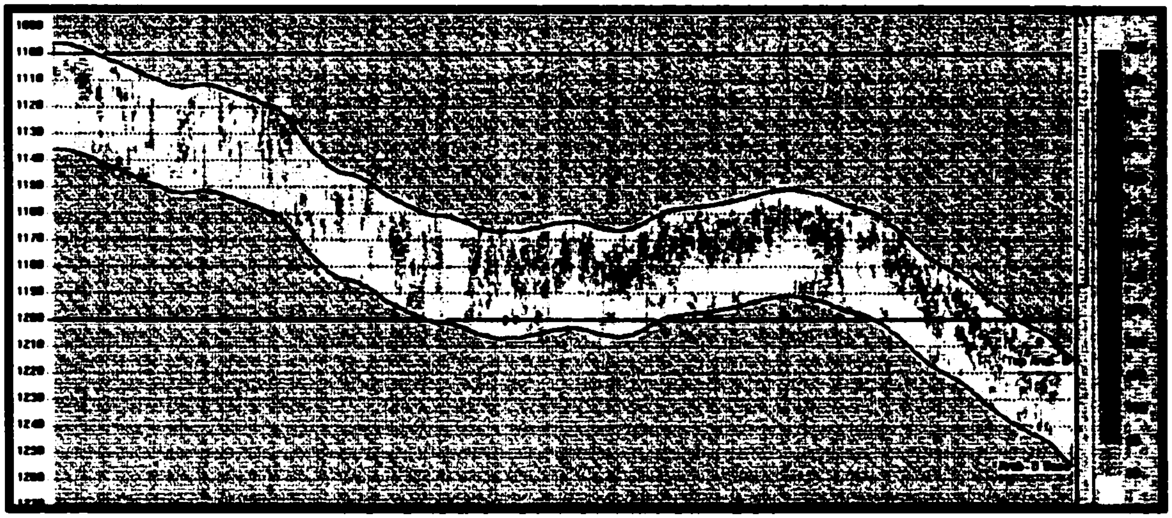

Figure 75: A cross-section along inline 150 showing permeability distribution

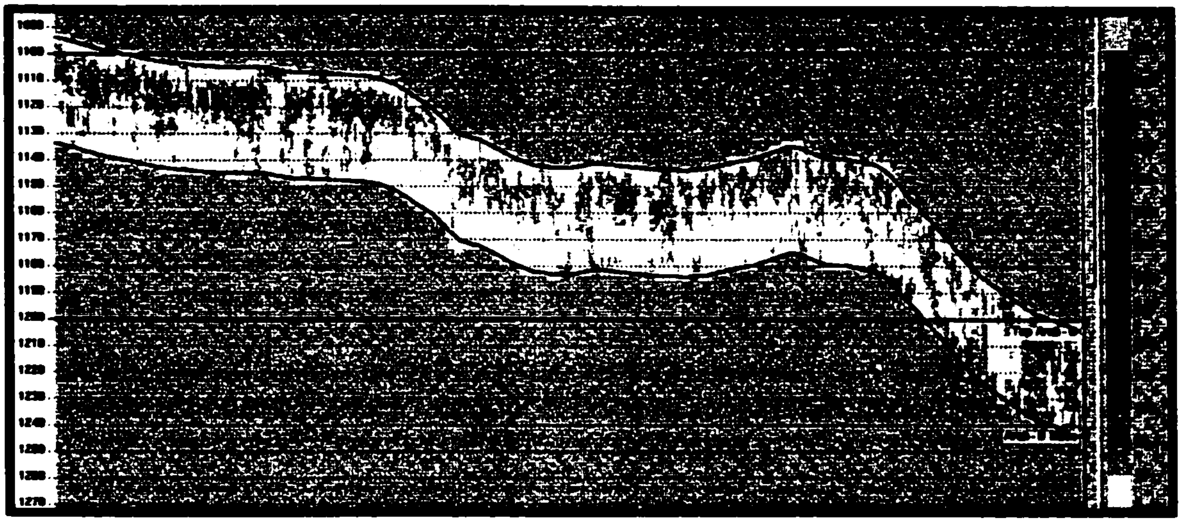

Figure 76: A cross-section along inline 250 showing permeability distribution

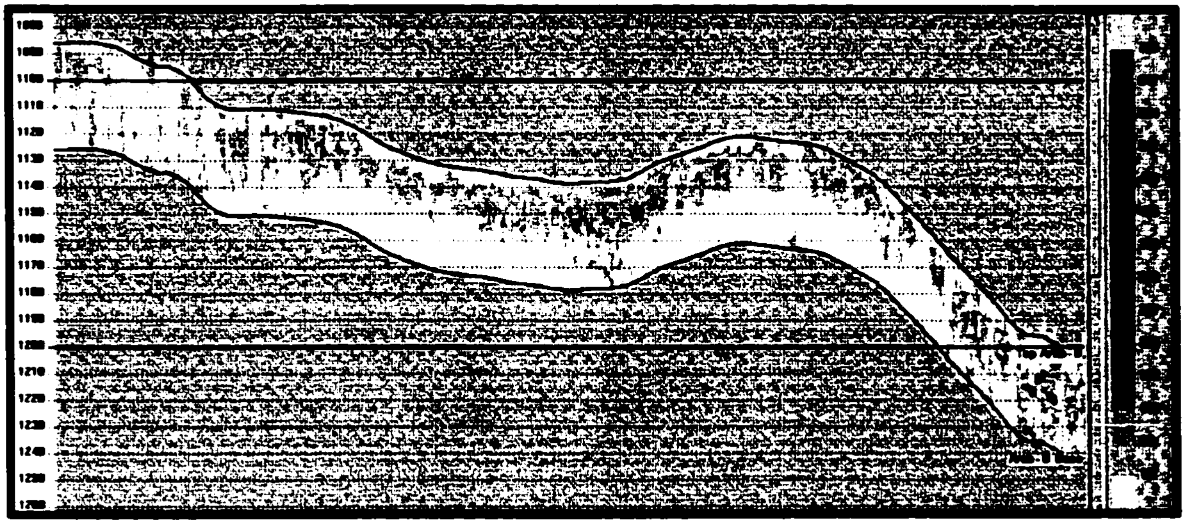

Figure 77: A cross-section along inline 350 showing permeability distribution

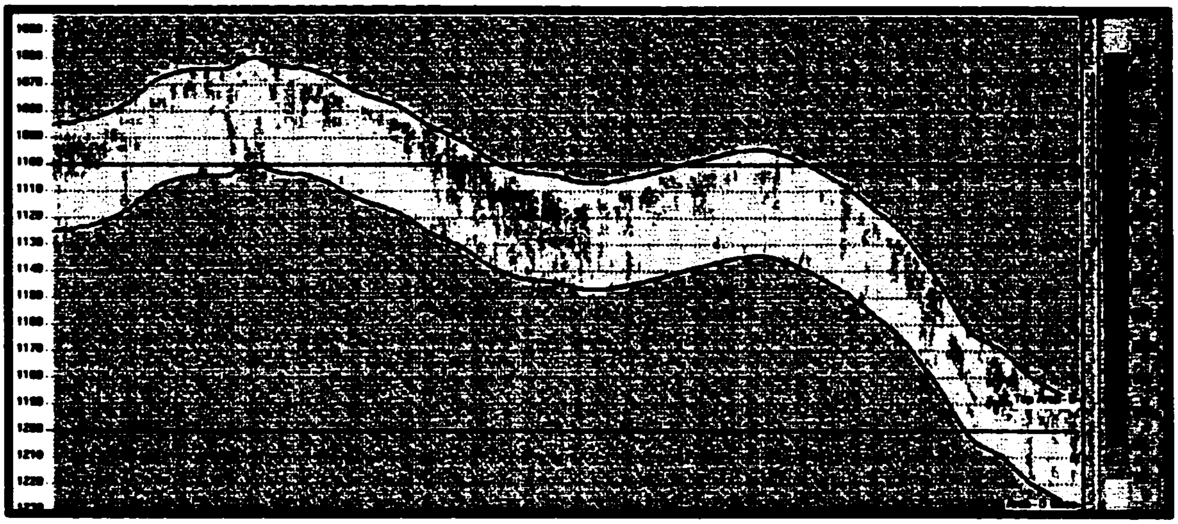

Figure 78: A cross-section along inline 450 showing permeability distribution

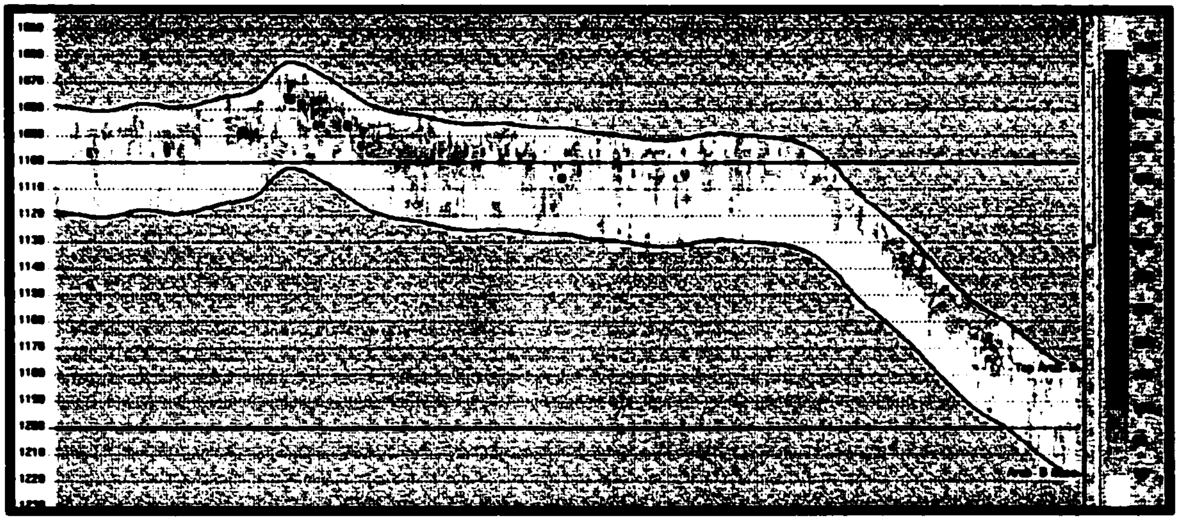

Figure 79: A cross-section along inline 550 showing permeability distribution

CHAPTER SIX

CONCLUSION AND RECOMMENDATIONS

Seismic inversion using model-based inversion algorithm was fairly successful for two reasons. Firstly, the high accuracy obtained using this method made results gained much more reliable. Secondly, honoring geology was guaranteed since stratal geometry or stratigraphy of the interval was preliminarily incorporated in the initial model, which largely constraint the final model. Therefore, the output impedance model was quite reliable to be utilized with high-level of confidence in further analyses.

Impedance often relates to lithology, which shows direct relationship to lithology and could thereby participate in lithology description and interpretation. This was objectively guided by the tremendous knowledge about the lithology of the Arab-D reservoir. Hence, detailed and meaningful reservoir lithological characterization was possible. This impedance lithological model was found to be nearly consistent with the available lithological information about the reservoir. Lithofacies distribution showed a clear disagreement with the generalized regional depositional trend suggested by many previous studies, which assumed a systematic facies gradation from grain-supported rocks to mud-supported rocks towards the flank. A local syncline was observed in the central part of the southern area where it exerts an obvious influence on the facies distribution and petrophysical properties. In addition, being integrated as secondary data to generate the porosity geostatistical model, seismic data could rigorously enhance resolution and alleviate the effect of the inappropriate extrapolation resulted from the insufficient well data.

To further investigate the lateral facies distribution due to change in depositional environment, a generalized lithofacies map for the reservoir interval was generated using neural network seismic classification. The map was conformable with facies distribution depicted from impedances. These results proved that the spatial distribution of rock types in most of the reservoir zones is structurally controlled where structural highs are dominated by porous grain-supported rocks grading to muddier rocks on the structural lows. This gradual change in facies types, in a systematic manner from the southeast to northwest, suggests a northeastern trend for the paleoshore line at this area. Advanced petrophysical investigations were performed to study the impact of the different petrophysical properties on the signal variability or the lithological distribution for each reservoir zone. As expected, porosity and density were found to be the main controlling factors to facies distribution indicating a sort of structural control since the facies distribution is a function of mud content and grain size.

Geostatistical methods have achieved a reasonable success when applied to model porosity. However, due to insufficient well information, kriging maps showed great inaccuracy. Cokriging and conditional simulation methods were introduced to solve this problem by incorporating acoustic impedance, which showed a good correlation with well porosity values. Hence, high-resolution accurate porosity maps were obtained. Nevertheless, these methods were rather biased when applied to permeability modeling. This is due to lack of sufficient well data and the inappropriate assumption of the linear bivariate porosity-permeability model, which is not always correct.

The new technique of the multi-attribute transforms and neural network was introduced to address the problem of permeability modeling. The new technique is capable of deriving parametric and non-parametric relationships between permeability and porosity and between permeability and seismic attributes and hence it maximizes the predictive power of modeling process. This method was firstly applied to generate porosity model, which was calibrated with the developed geostatistical model to test the validity of this method. Generated porosity model showed the same porosity distribution obtained from geostatistical model with slightly improved resolution and better accuracy. Robustness achieved in porosity modeling using Probabilistic Neural Network (PNN) was a major incentive to propose this method for solving the problem of permeability modeling.

The amplitude weighted phase, the integrated seismic trace and the instantaneous phase demonstrated the best correlation with permeability and they are consequently used in the PNN modeling of permeability. Lateral changes in phase always explain the changes of bedding character while the contribution of the integrated seismic trace to permeability modeling could not be justified and hence it is proposed for further investigation.

Impedances are generally low in zones 2A and 2B at the upper half of the reservoir, which is mainly composed of porous grain-supported carbonates. They dramatically increase in the lower zones of 3A, 3B and 4 due to the increase in the mud content at the bottom of the Arab-D reservoir. Zone 1 at the uppermost part of the reservoir showed the highest impedance values due the effect of dolomitization and the presence of the anhydrite. High-impedance rocks in the most porous zones of 2A and 2B mainly occur at the flank area are most likely attributed to dolomitization whereas these impedances are attributed to muddier rocks residing in a gentle low structural relief extending along the central region of the southern area.

It's obvious that porosity distribution is affected by facies and diagenetic factors. This became quite clear because of the great consistency between porosity distribution and facies distributions predicted from seismic inversion analysis. Porosity values are extremely low ranging from zero to 3.8 percent at the uppermost part of the reservoir (zone1). The lowest porosity values are present at the southeastern area of the central area in which they follow a northeastern trend. Relatively higher values are sporadically distributed over the entire survey with some concentrations on the eastern, northwestern and southwestern areas. This complex distribution pattern echoes the transitional nature (due to facies changes) of this reservoir zone.

Zone 2A showed very high porosity values compared to the previous zone. The highest values are located at the central part of the flank area. Other local high porosities at the southern part of the central area, southwestern and northwestern areas were also observed. Where low porosity values showed a general northeastern trend throughout the entire area. The increase in porosity values on the flank area may reflect syndepositional structural growth and concentration of highly porous grain-supported carbonates. It may also be attributable to the development of local minor fractures dominant in these areas. The decrease in porosity on the flank to the south probably reflects degradation of reservoir due to dolomitization. The highest porosities within the reservoir were observed in the upper part of zone 2B, which is dominated by high porosities (> 18%). While the lower part of zone 2B displayed moderate to high porosity values. Porosity distribution reflects the extreme heterogeneity of this part of the zone caused by dolomitization.

Zone 3A showed moderate porosity values, which generally increase eastward and southward with local high-porosity area to the northwest. Porosities in zone 3B are lower than those of zone 3A, yet larger than those of zone1. The highest values concentrate on the flank area.

Generally, the reservoir displays moderate to low permeability values. The low permeability values are dominant at the lowest part of the reservoir interval, which includes zones 3A, 3B and 4. This doesn't typically apply on the flank areas, where these zones comprise high permeabilities. Most of the very high permeabilities encountered in zones 2B and 2A are obviously concordant with areas showing as high porosity as 18%. This suggested that these permeabilities to be resulted from the interconnected vugular and moldic pores associated with the dolomite facies prevailing in these zones.

Very high permeable regions encountered in lowermost zones on the flank areas were interpreted as to be caused by either fracture clusters or locally dolomitized layers occurring within these zones. Since the compacted muddier carbonates of these zones are expected to be more brittle and susceptible to fracturing, which is most probably triggered by the gentle bending of the distal flank.

Although accurate and reliable results were obtained in this study, better results are strongly expected if additional well data is augmented. This will drastically remove the effect of inappropriate interpolation and the dominance of the seismic data, which degraded the geostatistical results. Besides, the increase of the training data used in neural networks applications for petrophysical modeling will definitely maximize the accuracy of results obtained. Core description at some control wells within the study area will immensely contribute to lithological interpretation using seismic inversion. Therefore, core analysis is strongly recommended for further detailed lithological description.

Stochastic lithological modeling using seismic attributes might provide another mean for direct and much accurate lithofacies description. Hence, it deserves to be tried in further studies in order to verify the impedance-based lithological interpretation.

Detailed investigation and modeling of fractures is anticipated to contribute in precisely characterizing the fluid-flow units of the reservoir. Through research and practice of certain fractured reservoirs, a few methods are summed up as follows: 1) Lithology control on fractured distribution is well known, fractured zones can be indirectly predicted by means of seismic inversion detecting lithology distribution. The applications of the method in carbonate reservoir have gained good effects. 2) It is certain that seismic data mainly contain lithology and fracture information; fractured zones can be identified by comparison of seismic inversion results from lithology and fracture information.

APPENDIX A

POROSITY-IMPEDANCE RELATIONSHIP

Impedance is a product of rock density and sonic velocity of the rock:

I(j) = impedance = ρ(j) v(j) = density $_{(j)}$ × velocity $_{(j)}$

Density of a specific rock type is inversely proportional to its porosity (ϕ) (Figure a):

$$\rho_r(\phi) = \rho_f\phi + (1-\phi)\rho_s \qquad \text{(A-1)}$$

$$\therefore \rho_r(\phi) = (\rho_f - \rho_s)\phi + \rho_s$$

Where: ρ_r = Volume density of the total rock

ρ_f = Volume density of the pore fluid

ρ_s = Volume density of the solid matrix

Note that $\rho_f - \rho_s < 0.0$, therefore making the slope always negative.

The sonic velocity (V_r) of a rock is also inversely proportional to its porosity

$$\frac{1}{V_r(\phi)} = \frac{\phi}{V_f} + \frac{1-\phi}{V_s} \qquad \text{(A-2)}$$

Where: V_r = Sonic velocity of the total rock

V_f = Sonic velocity of the pore fluid

V_s = Sonic velocity of the solid matrix

Rock acoustic impedance is defined as:

$$I_r(\phi) = V_r(\phi)\rho_r(\phi)$$

Inserting equations (1) and (2) into equation (3) and simplifying, we get:

$$I_r(\phi) = \frac{V_S V_F\left[\rho_S + (\rho_F - \rho_S)\phi\right]}{V_F + (V_S - V_F)\phi} \quad \text{(A-3)}$$

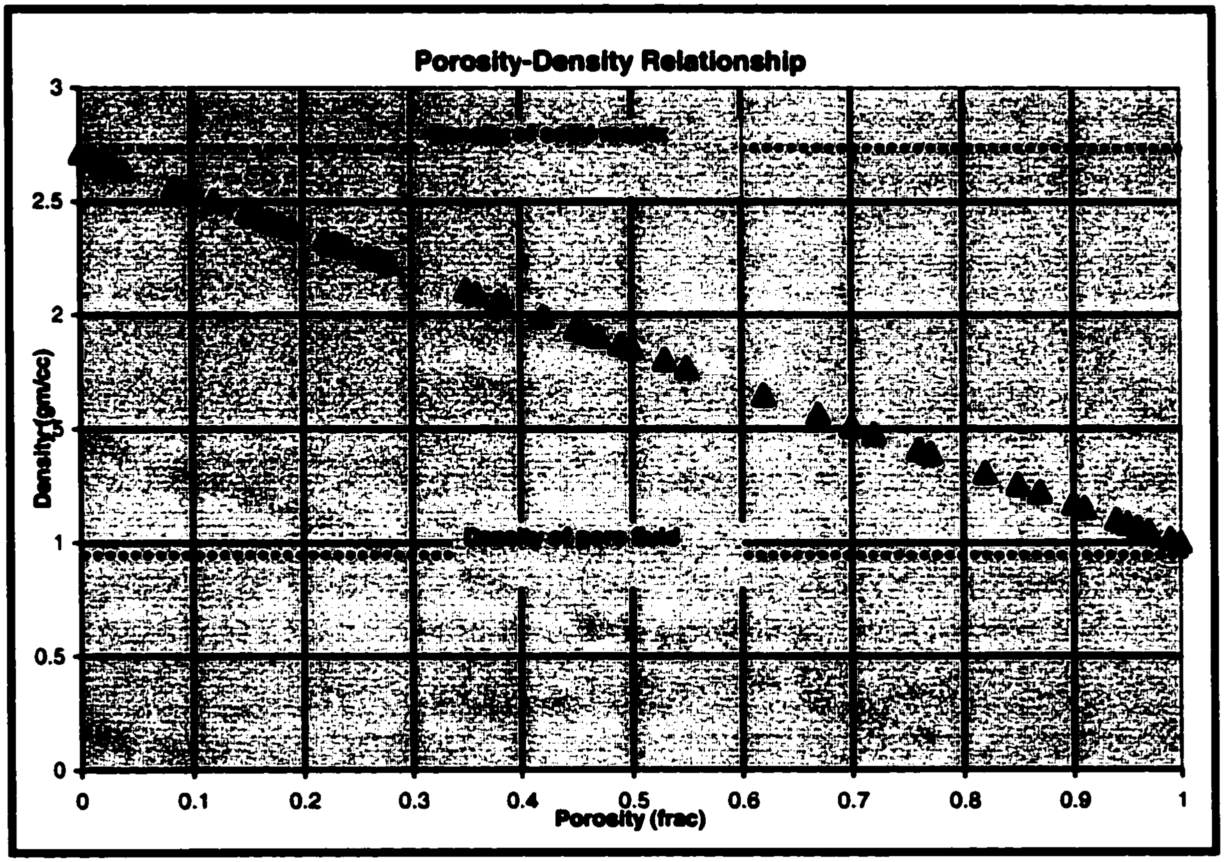

Figure A-1: Cross-plot showing the relationship between rock porosity and rock density. The rock is composed of limestone with water pore fluid.

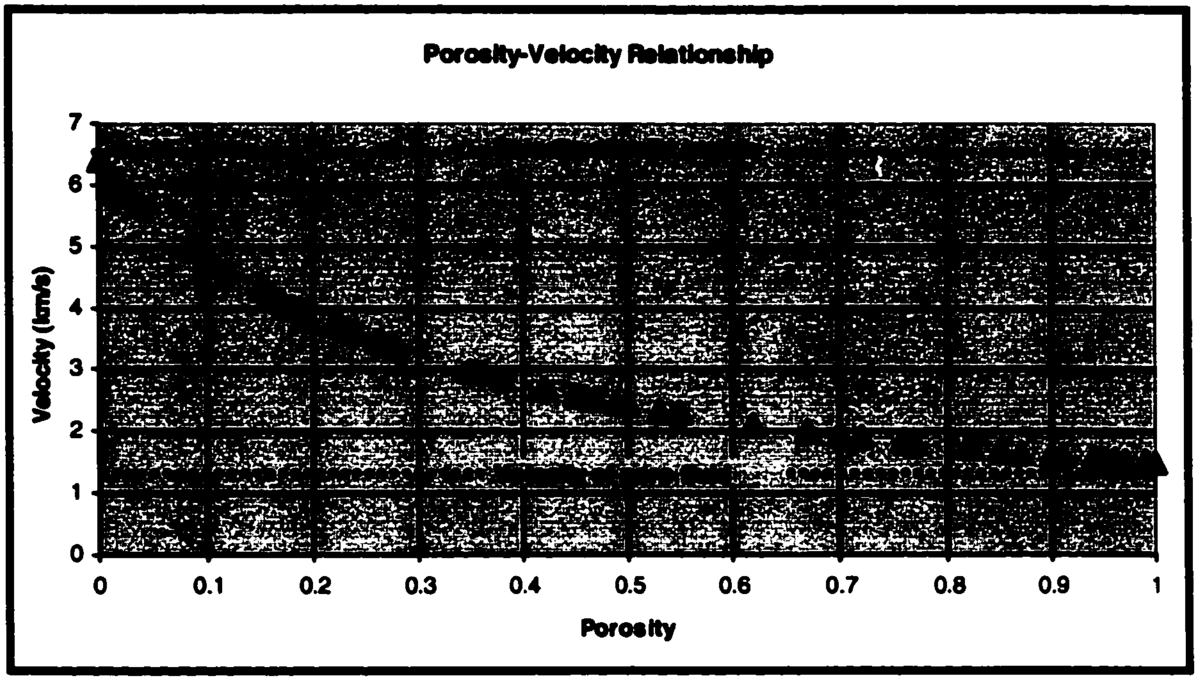

Figure A-2: Cross-plot showing the relationship between rock porosity and sonic velocity. The same rock type as in figure A-1.

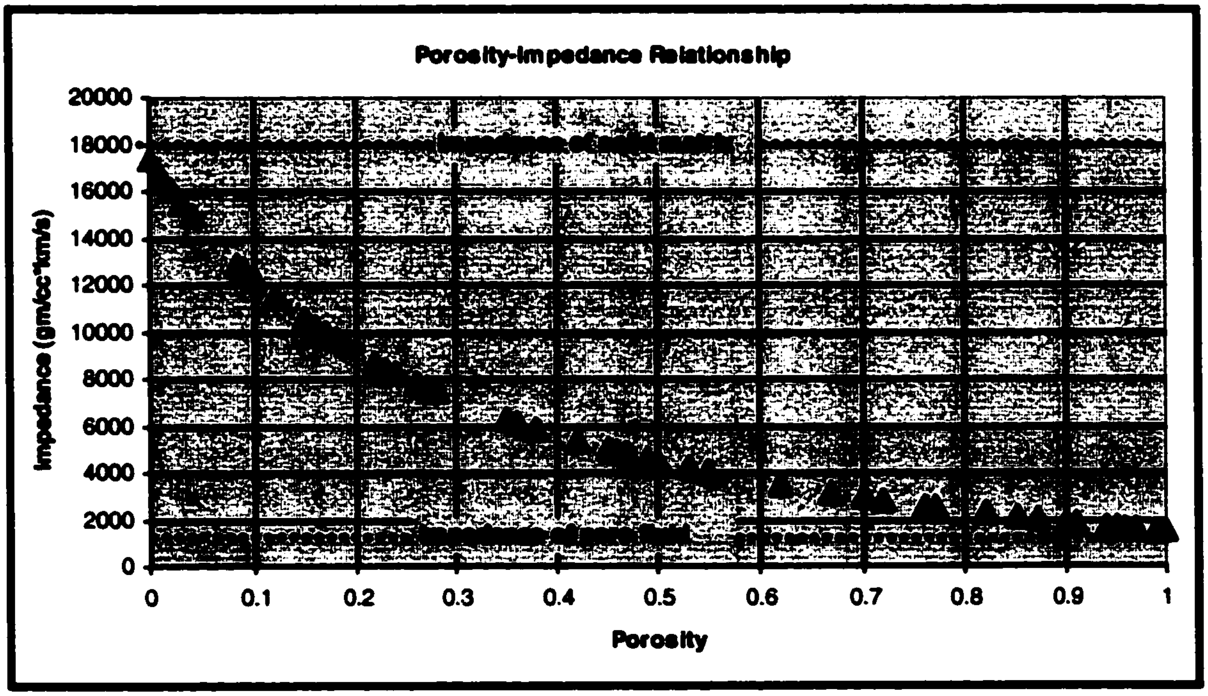

Figure A-3: Cross-plot showing the relationship between rock porosity and acoustic impedance. The same rock type as in figure A-1.

REFERENCES

Addy, S. K., 2001, Neural Net Generated Seismic facies Map and its Application in various Geologic Environments: www.paradigmgeo.com

Anjos, C. E. G., and Zucchi, H., 2001, Geological and geophysical integrated methodology for reservoir characterization: SPE Latin American and Caribbean Petroleum Engineering Conference held in Buenos Aires, March 25-28 2001.

Alsharahan, A. S. and Whittle, G. L., 1995, Carbonate-evaporite sequences of the Late Jurassic, Southern and Southwestern Arabian Gulf: AAPG Bulletin, v. 79/11, p. 1608-1630.

Atkins, D. A., Wilson, M., and Sams, M. S., 2001, Sequence Stratigraphy and Seismic Impedance: A new Approach to Reservoir Characterization: EAGE 63rd Conference and Technical Exhibition held in Amsterdam from 11 to 15 June 2001.

Bashore, W. M., Araktingi, U. G., Levy, M., and Schweller, W. J., 1994, Importance of geological framework and seismic data integration for reservoir modeling and subsequent fluid flow predictions: AAPG, computer application in geology, No. 3, p. 159-175.

Brown, A. R., 1996, Interpretation of three-dimensional seismic data, fourth edition: AAPG Memoir 42, p 223-285.

Cantrell, D. L. and Hagerty, R. M., 1999, Microporosity in the Arab-D Formation carbonates, Saudi Arabia: GeoArabia, v. 4/2, p. 129-154.

Cantrell, D. L., Swart, P. K., Handford, R. C., Kendall, C. G., and Westphall, H., 2001, Geology and production significance of dolomite, Arab-D Reservoir, Ghawar Field, Saudi Arabia: GeoArabia, v. 6, No. 1, p. 45-59.

Daetwyler, C. C., Hagerty, R. M., Cantrell, D. L., and Corwin, L. W., 1987, Arab-D Reservoir Geology Guide, Abqaiq and Ghawar Fields, Saudi Arabia: Exxon Production Research Company.

Dobrin, M. B., and Savit, C. H., 1988, Introduction to Geophysical Prospecting: McGraw-Hill Book Company, 867p.

Douglas, J. L., 1996, Geostatistical model of the Arab-D reservoir, North 'Ain Dar Pilot, Ghawar Field, Saudi Arabia: An improved reservoir simulation model: GeoArabia, v.1/2, p. 267-284.

Gosse, C. L. and Sissons, B. A., 2000, Lithology Prediction in Taranaki Basin Using Neural Network Applications: 2000 New Zealand Petroleum Conference Proceedings, 19-20 March 2000.

Hampson, D., Schuelke, J., Quieren, J., Using Multi-Attribute Transforms to Predict Log Properties from Seismic Data: Geophysics, v., no., p..

Hampson-Russell Software Services, 2000, GEOSTAT Workshop: GEOSTAT Class Exercises, p. 20-25.

Hearn, C. L., Hobson, J. P., and Fowler, M. L., 1986, Reservoir characterization for simulation, Hartzog Draw Field, Wyoming: Reservoir characterization, Academic Press, INC., Harcourt Bruce Jovanovich, Publishers, p. 341-372.

Huges, G. W., 1996, A new bioevent stratigraphy of Late Jurassic Arab-D carbonates of Saudi Arabia: GeoArabia, v. 1, No. 3, p. 417-434.

Johnsen, G., Elde, R., and Skalnes, A., 1996, Use of inverted seismic data in well planning and in 3-D reservoir modeling: NPF/SPE European 3-D reservoir modeling conference held in Stavanger, Norway, 16-17 April 1996.

Journel, A. G., 1994, Geostatistics and reservoir geology: AAPG, computer application in geology, No. 3, p. 19-20.

KFUPM, 2000, Ghawar Field Structural Model and Electronic Database: Final report, volume I, PN 23078, Research institute-King Fahd University of Petroleum and Minerals, 223p.

Lamy, M., Swaby, P. A., Rowbotham, P. S., and Dubrule, O., 1998, From seismic to reservoir properties using geostatistical inversion: SPE 49147, p. 171-196.

Lee, S. L. and Datta-Gupta, A., 1999, Electrofacies characterization and permeability predictions in carbonate reservoirs: Role of multivariate analysis and non-parametric regression: SPE Annual Technical Conference and Exhibition held in Houston, Texas, October 3-6 1990.

Marzuki, Z., Sams, M. S., Atkins, D., 2001, Adding value to impedance through sequence stratigraphy: SPE Annual Technical Conference and Exhibition held in New Orleans, Louisiana, 30 September to 3 October 2001.

Meyer, F. O., Price, R. C., Al-Ghamdi, I. A., Al-Goba, I. M., Al-Raimi, S. M. and Cole, J. C., 1996, Sequential stratigraphy of outcropping strata equivalent to Arab-D reservoir, Wadi Nisah, Saudi Arabia: GeoArabia, v. 1/3, p. 435-455.

Meyer, F. O., Price, R. C., and Al-Raimi, S. M., 2000, Stratigraphic and petrophysical characteristics of cored Arab-D super-k intervals, Hawyiah area, Ghawar Field, Saudi Arabia: GeoArabia, v. 5/3, p. 355-384.

Olea, R. A., 1994, Fundamentals of Semivariogram Estimation, modeling and Usages: AAPG, computer application in geology, No. 3, p. 27-35.

Poupon, M., Azbel, K., and Ingram, J. E., 2001, Integrating seismic facies and petro-acoustic modeling: www.paradigmgeo.com

Powers, R. W., Ramirez, L. F., Redmond, C. D., and Elberg, E. L., 1966, Geology of the Arabian Peninsula: Sedimentary Geology of Saudi Arabia, United States Government Printing office, Washigton.

Riel, P. V., 2000, The Past, Present, and Future of Quantitative Reservoir Characterization: The Leading Edge, v. 8, p 878-881.

Sahin, A., and Ghori, S. G., 1997, Stochastic mapping of lithology in a complex carbonate reservoir: SPE 37697, p. 183-193.

Saner, S., and Sahin, A., 1999, Lithological and zonal porosity-permeability distributions in the Arab-D reservoir, Uthmaniyah Field, Saudi Arabia: AAPG Bulletin, v. 83/2, p. 230-243.

Schlumberger, 1976, Well Evaluation Conference, Iran

Sonneland, L., Barkved, O., and Hagenes, O., 1990, Reservoir characterization by seismic classification maps: SPE Annual Technical Conference and Exhibition held in New Orleans, Louisiana, September 23-26 1990.

Soto, R., Bernal, M. C., Silva, B., Bejarano, A., Cobaleda, G., Arango, S., and Torres, F., 2000, How to improve reservoir characterization using intelligent systems: A case study: Toldado Field in Colombia: 2000 SPE Annual Technical Conference and Exhibition held in Dallas, Texas, October 1-4 2000.

Soto, R., Torres, F., Arango, S., and Cobaleda, G., 2001, Improved reservoir permeability models from flow units and soft computing techniques: A case study, Suria and Performa-Librated Fields: SPE Latin American and Caribbean Petroleum Engineering Conference held in Buenos Aires, March 25-28 2001.

Srivastava, R. M., 1994, An overview of stochastic methods for reservoir characterization: AAPG, computer application in geology, No. 3, p. 3-16.

Taner, M. T., Schuelke, J. S., O'Doherty, R., Baysal, E., 1994, Seismic attributes revisited: 64th Annual International Meeting, Society of Exploration Geophysicists, Expanded Abstracts, v. 94, p. 1104-1106.

Valle, A., Faulhaber, J. J., Keith, T. H., and Hsueh, P. T., 1997, Development of integrated reservoir characterization and simulation model for a heterogeneous carbonate reservoir, Arab-D reservoir, East flank of Ghawar Field: Middle East Oil Show held in Bahrain, 15-18 March 1997.

Vegbaek, O. V., and Rasmussen, K. B., 1996, Geostatistical reservoir characterization using inverted seismic data, Dan Field, Denmark: NPF/SPE European 3-D reservoir modeling conference held in Stavanger, Norway, 16-17 April 1996.

Wang, F. P., Lucia, F. J., and Kerans, C, 1998, Modeling dolomitized carbonate- ramp reservoirs: A case study of the Seminole San Andres unit: Geophysics, v. 63, No. 6, p. 1866-1883.

Weber, K. J., 1986, How heterogeneity affects oil recovery: Reservoir characterization, Academic Press, INC., Harcourt Bruce Jovanovich, Publishers, p. 487-544.

Wolf, D. J., Withers, K. D., Burnaman, M. D., 1994, Integration of Well and Seismic Data Using Geostatistics: AAPG, computer application in geology, No. 3, p. 177-199.

Xu, W., Tran, T. T., Srivastava, R. M., Journel, A. G., 1992, Integrating Seismic Data in Reservoir Modeling: The Collocated Cokriging Alternative: SPE Annual Technical Conference and Exhibition held Washington, DC, October 4-7 1992.

Zhang, L., Quieren, J., Schuelke, J., 2001, Self Organizing map and Neural Network for Tracking Horizons and Classifying Seismic Traces: www.fcii.arizona.edu/poulton/gen587temp/chapter10.pdf

Vita:

Name: Sami Osman Ibrahim

Date of Birth: 3/ 11 / 1970

Nationality: Sudanese

Academic Qualifications: - B.Sc. (Honors-First class) from university of Khartoum, Faculty of Science, Department of Geology (December, 1995).

- MS from King Fahd University of Petroleum and Minerals, College of Science, Earth Sciences Department (April, 2002)

Work Experience: - Teaching Assistant-University of Khartoum, Khartoum-Sudan (January, 1996-January, 1999)

- Research Assistant- King Fahd University of Petroleum and Minerals, Dhahran, Saudi Arabia (January, 1999-April, 2002)